Action of Anesthetics on Membranes

and

Protein Adsorption on Solid Surfaces

studied by

Molecular Dynamics Simulations

von

Beate Jutta Griepernau

Saarbrücken

2009

Tag des Kolloquiums: 29. Mai 2009

Dekan: Univ.-Prof. Dr. rer. nat. Christoph Becher

Mitglieder des
Prüfungsausschusses: Univ.-Prof. Dr. rer. nat. Manfred Lücke
                          Univ.-Prof. Dr. rer. nat. Karin Jacobs
                          Dr. rer. nat. Rainer Böckmann
                          PD Dr. rer. nat. Patrick Huber

Hiermit versichere ich an Eides statt, dass ich die vorliegende Arbeit selbstständig und ohne Benutzung anderer als der angegebenen Hilfsmittel angefertigt habe. Die aus anderen Quellen oder indirekt übernommenen Daten und Konzepte sind unter Angabe der Quelle gekennzeichnet. Die Arbeit wurde bisher weder im In- noch im Ausland in gleicher oder ähnlicher Form in einem Verfahren zur Erlangung eines akademischen Grades vorgelegt.

Saarbrücken, Januar 2009

Abstract

In this thesis, the mechanisms underlying anesthesia and the adsorption of proteins on solid surfaces have been studied using the method of molecular dynamics simulations.

It is generally assumed that biological membranes are the site of anesthetic action. However, there is no consensus whether anesthetics act directly by binding to membrane proteins, thereby inhibiting their function, or indirectly by modulating the physical properties of the lipid part of the membrane. In the simulations presented here, distinct changes of lipid bilayer properties in response to the presence of alkanols, a group of anesthetics, have been observed. An anesthetic-induced shift of the equilibrium between different membrane protein conformations, modeled by simple geometric shapes, has been found. In simulations with the ion channel gramicidin A embedded in a lipid bilayer, alkanols distributed inhomogeneously in the bilayer, with almost no alkanol molecules residing in close vicinity to the gramicidin. These results provide evidence for an indirect mode of anesthetic action.

Spontaneous protein adsorption on solid-liquid interfaces is the first step in the formation of biofilms. Here, a coarse-grained molecular dynamics scheme has been applied to study this complex process at high resolution, but still reaching the necessary time and length scales. Changes in protein structure and dynamics after adsorption and preferred orientations of proteins on the surface were observed.

Zusammenfassung

In dieser Arbeit wurde die Wirkungsweise von Anästhetika und die Adsorption von Proteinen an Festkörperoberflächen mittels Moleküldynamik-Simulationen untersucht.

Es wird allgemein angenommen, dass Anästhetika auf biologische Membranen wirken. Umstritten ist jedoch, ob Anästhetika direkt an Membranproteine binden und damit deren Funktion hemmen, oder ob sie indirekt wirken, indem sie die physikalischen Eigenschaften der Lipiddoppelschicht der Membran verändern. Solche indirekten Effekte wurden in den hier vorgestellten Simulationen bei Anwesenheit von Alkanolen, einer Gruppe von Anästhetika, beobachtet. Gleichzeitig wurde eine durch Anästhetika verursachte Verschiebung des Gleichgewichts zwischen unterschiedlichen, vereinfacht dargestellten Proteinkonformationen gefunden. Simulationen eines in einer Lipiddoppelschicht eingebetteten Ionenkanals zeigten eine sehr geringe Konzentration von Alkanolen in unmittelbarer Nähe des Kanals. Diese Ergebnisse deuten auf eine indirekte Wirkungsweise von Anästhetika hin.

Spontane Adsorption von Proteinen an fest-flüssig Grenzflächen ist der erste Schritt bei der Bildung von Biofilmen. Um diesen Prozess der Proteinadsorption mit hoher Auflösung auf ausreichend langen Zeit- und Längenskalen zu untersuchen, wurde ein „coarse-grained" Moleküldynamik-Schema verwendet. Es wurden Veränderungen in der Proteinstruktur und -dynamik und bevorzugte Ausrichtungen der Proteine auf der Oberfläche beobachtet.

Contents

Contents

Part I

Action of Anesthetics on Membranes

1 Biological Basics and Motivation

Anesthetic action is generally assumed to take place at the site of biological membranes, impeding signal propagation along or across cells. However, neither the exact molecular target of anesthetics nor their mode of operation are known today.

Here, possible molecular mechanisms underlying anesthesia have been studied by means of molecular dynamics simulations. In a first step, the influence of 1-alkanols of different hydrocarbon chain lengths (Fig. 1.1) on lipid bilayers as a simplified approximation for biological membranes has been investigated. The simulations provided a basis to judge
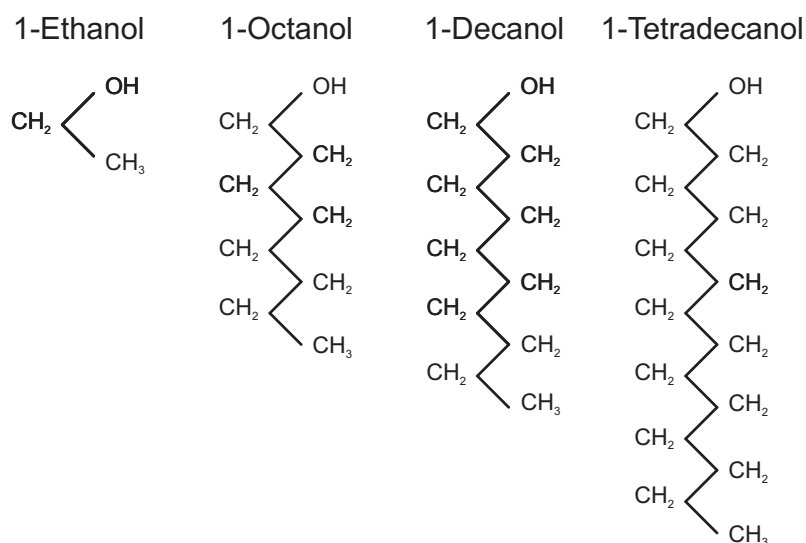
Figure 1.1: 1-alkanols (also called 1-alcohols) considered in this study. Characteristics are the polar hydroxyl headgroup bonded to the first carbon atom and the hydrophobic hydrocarbon chain. 1-alkanols with a chain length of up to 12 carbon atoms (dodecanol) are anesthetics (see, e. g., [206]).

different models previously proposed for anesthesia on an atomistic level, as 1-alkanols up to a chain length of approximately 12 carbon atoms act as anesthetics (see, e. g., [206]). Subsequently, effects of high pressure on lipid bilayers containing 1-alkanols were assessed in additional simulations, as *in vivo* anesthesia has been shown to be reversed by application of pressure. Emphasis was placed on the calculation of local lateral stresses within the bilayers, which have been suggested to play an important role in the mechanism of anesthesia [33–35]. Quantitative predictions for a shift in the conformational equilibrium of membrane proteins, described by simple geometric shapes, were possible. Finally, the influence of 1-alkanols on a membrane-embedded ion channel modeled in full atomistic detail was investigated.

The thesis starts with an introduction to biological membranes and membrane proteins, before the term anesthesia is specified and different models of anesthetic action that are currently discussed in literature are presented. In Chapter 2, an overview over the history and progress, as well as the limitations of molecular dynamics simulations is given, together with a detailed explanation of simulation algorithms and techniques. Results obtained within this part of the thesis are presented in the Chapters 3, 4, and 5, followed by concluding remarks in Chapter 6.

1.1 Biological Membranes

Biological membranes are abundant in nature. Each cell is surrounded by a membrane (a so-called plasma membrane or cell wall), segregating the cell cytoplasm from the surrounding medium, and also single organelles within cells are typically enclosed by their own membrane. By this compartmentalization of organisms in smaller, biologically active, and highly specialized subunits, chemical reactions can be performed more effectively. The membranes provide mechanical stability as well as high flexibility to the cell, and they serve as selective filters for the passive transport (e.g., diffusion or osmosis) of matter, being permeable only for some small, uncharged molecules, but impermeable for, e.g., ions or larger amino acids. In this way, concentration and charge gradients in the cell can be created and upheld. The transport of larger molecules and ions across cell walls is ensured by the mechanisms of endo- and exocytosis, where small carrier vesicles fuse with or constrict from the cell membrane (Fig. 1.2), and by specialized proteins inside the membrane (e.g., ion channels or transport proteins). Furthermore, plasma membranes are the site for receptor molecule binding (important for, e.g., cell-cell communication) and the site for metabolic activities and energy producing processes. Finally, biological membranes can propagate voltage pulses and are therefore also essential in signal transduction.
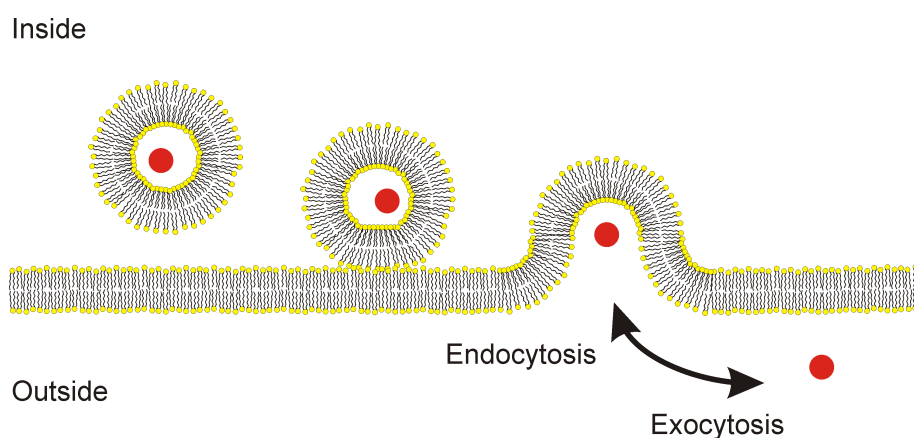
Figure 1.2: Mechanism of exo- and endocytosis. In exocytosis, material from the inside of the cell, that is enclosed in a small lipid vesicle, is released into the medium surrounding the cell by fusion of the transport vesicle with the cell membrane. Endocytosis is the reverse process allowing for the uptake of material into the cell.

Plasma membranes of animal cells (Fig. 1.3) consist of three layers [144]: the glycocalix at the outer membrane surface, a central lipid-protein layer, and the cytoskeleton at the inner cell wall. The glycocalix (cell coat) is a carbohydrate-rich, macromolecular film of several tens of nanometer thickness, built up by the extracellular domains of glyco-lipids and glycoproteins (i. e., lipids and proteins with covalently bound oligosaccharides (sugars)) that are anchored in the central lipid-protein layer. The cytoskeleton is a fibrous protein network that provides mechanical stability to the cell. The characteristic and main structural part of biological membranes is the lipid-protein layer (see Fig. 1.3), where functional membrane proteins are embedded in or attached to a lipid bilayer. The mass
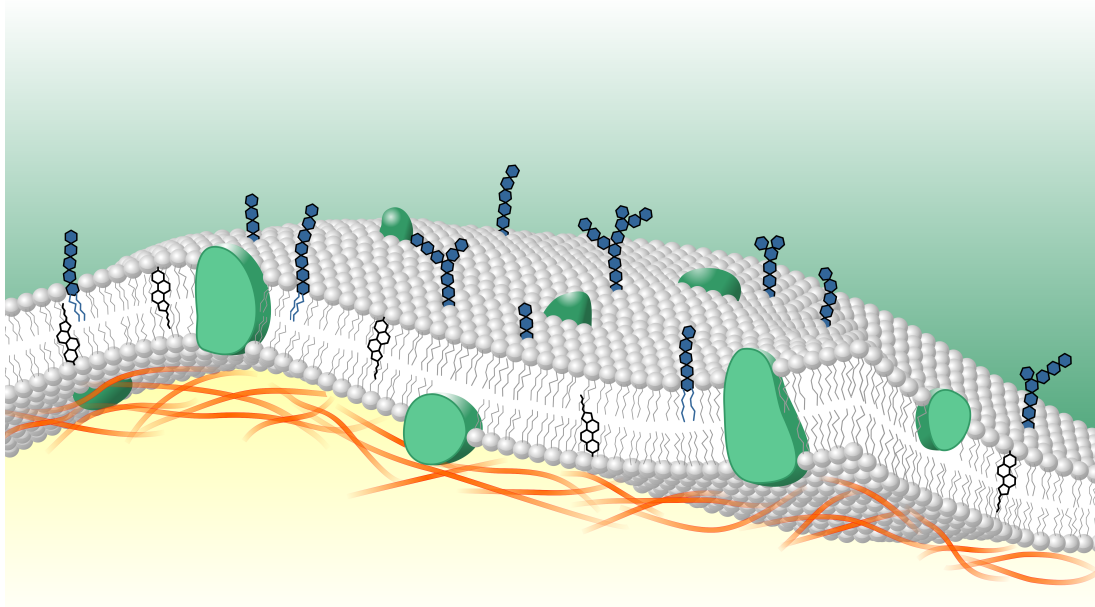
Figure 1.3: Schematic picture of a biological membrane. The central layer consists of different types of lipids (shown here in grey), glycolipids (blue), some sterols (black molecules, discernable by their ring structure; only in eukaryotic cell membranes), and embedded membrane proteins (green). At the cytoplasmic side (yellow), the lipid-protein layer is connected to the fibrous net-work of the cytoskeleton, depicted here in red. At the extracellular side (green), the lipid-protein layer is attached to the glycocalix, indicated by the carbohydrate moieties of the glycolipids (blue).

ratio of proteins to lipids depends on the membrane type and varies from 3.6 for mito-chondrial membranes to 0.25 for myelin membranes [67]. For plasma membranes it is about 1.0.

Lipids are amphiphilic molecules with a polar or negatively charged, hydrophilic head-group and one or more hydrophobic hydrocarbon chains[1]. There exists a wide variety of different lipids, varying in, e. g., the headgroup composition, the hydrocarbon chain length, or the chain unsaturation. Depending on the ratio of the headgroup volume to the chain volume and on the lipid concentration, lipids dissolved in water spontaneously

---

[1]In a broader sense, lipids can be defined as all naturally occurring molecules that are insoluble in water (see, e. g., [19]). Here, I follow the notion commonly used in membrane biophysics (see, e. g., [98]) defining lipids as amphiphilic molecules, i. e., molecules with one polar and one apolar part.

aggregate into micelles or bilayers. In such a bilayer, a broad variety of different lipids, mostly phospholipids (see Fig. 1.4) with two hydrocarbon chains of 8 to 22 carbon atoms each, is arranged in a planar, sandwich-like structure, where the hydrocarbon chains stretch into the bilayer core and the lipid headgroups are oriented towards the outside of the bilayer (Fig. 1.3). The thickness of these structures is about 5 to $10\,\mathrm{nm}$. At phy-
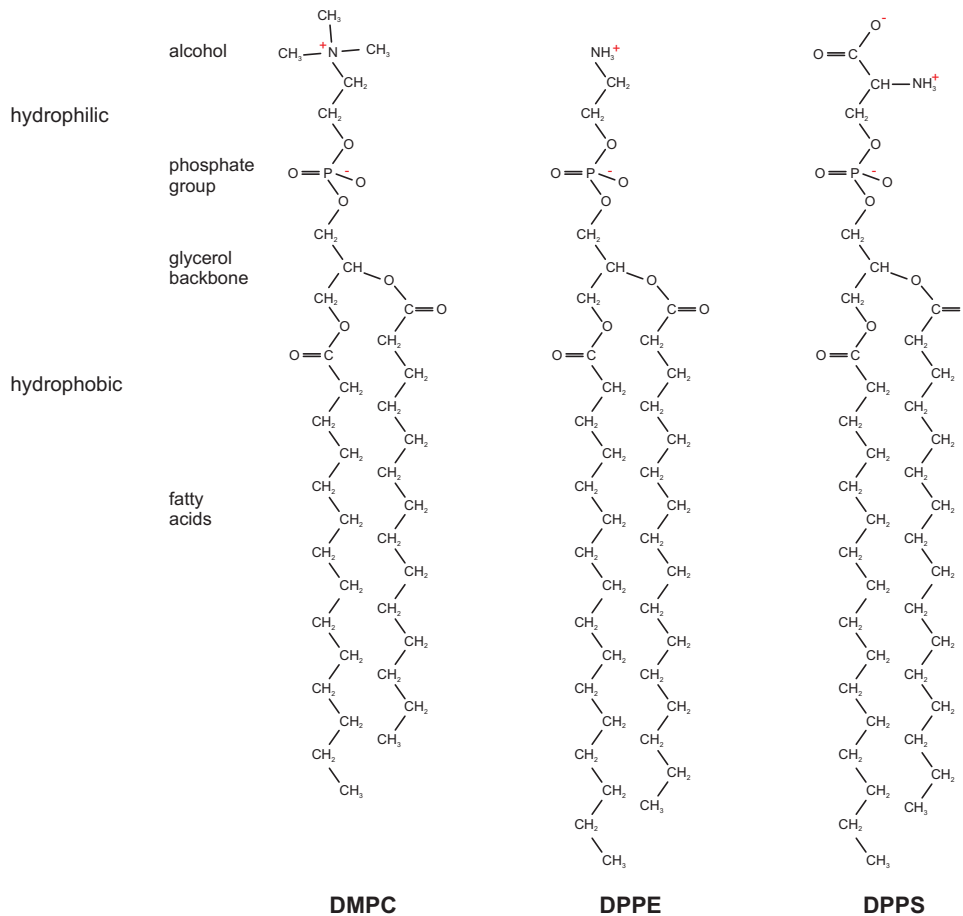
Figure 1.4: Structure of three phospholipids commonly found in biological membranes: dimyristoylphosphatidylcholine (DMPC), dipalmitoylphosphatidylethanolamine (DPPE), and dipalmitoylphosphatidylserine (DPPS). The hydrophilic lipid headgroup usually consists of an alcohol rest bound to a phosphate group. The hydrophobic part of phospholipids is typically built up by two fatty acid chains bound to a glycerol or a sphingosine moiety. Different lipids vary in the headgroup composition and in the length and unsaturation of the hydrocarbon fatty acid chains.

siological conditions, the lipid matrix is in the fluid, also called liquid disordered, phase, where the lipids as well as embedded proteins can (almost) freely diffuse within the membrane plane. This behavior was described by Singer and Nicholson in their famous "fluid mosaic model" [238]. At low temperatures or high pressures, lipid bilayers undergo a phase transition to a more ordered gel phase (see, e. g., [98]) or to a pressure-induced, partially interdigitated gel phase (see, e. g., [64]).

The lipid composition of biological membranes found in nature varies considerably, not only between different species, but also within single organisms and within domains of

one membrane. Depending on the mixture of lipids, membranes exhibit diverse structural and dynamical properties (see Section 1.1.1). In plasma membranes, three different kinds of lipids prevail: phosphatidylcholines (PC), phosphatidylethanolamines (PE), and the negatively charged phosphatidylserines (PS) (Fig. 1.4). These lipid species are usually asymmetrically distributed between the two monolayers, with more PC lipids in the outer membrane leaflet and more PE lipids in the inner leaflet. PS lipids are exclusively found in the inner leaflet, leading to a charge separation that is crucial for the orientation of membrane proteins in the plasma membrane ("positive-inside rule") and probably also for membrane fusion. The membrane composition can change in response to environmental conditions; for example, bacterial membranes have been shown to adopt their melting temperature when grown at higher temperatures ([98] and references therein). This diversity and adaptiveness strongly suggests a relation between the lipid composition and the function of a biological membrane, as assumed in lipid and lipid-mediated theories for anesthesia (see Section 1.3).

1.1.1 Structural and Dynamical Properties

Besides by their composition, lipid bilayers are characterized by structural and dynamical properties like the area per lipid, the bilayer thickness, the lipid tilt angle, the lipid dipole moment, the deuterium lipid order parameter, and the bilayer bending rigidity. As these parameters are used in the analysis of the trajectories obtained from the molecular dynamics simulations, they are introduced here. This section is of rather technical nature and can be omitted on a first reading.

The area per lipid is the area that each lipid occupies within the bilayer plane. In lipid bilayer simulations, it is usually obtained by dividing the total area of the simulation box in the membrane plane by the number of lipids in one monolayer. Although in this way only the projected area of the bilayer is taken into account and undulations of the membrane are neglected, the error is expected to be small in nanoscopic multilamellar systems simulated using periodic boundary conditions (see Section 2.2.5). As lipid bilayers are self-assembled structures, in thermal equilibrium the area per lipid adjusts itself to minimize the free energy and the bilayer is in a tension-free state.

The bilayer thickness depends on the length of the lipid carbon tails and on their order, commonly measured in terms of the (average) deuterium lipid order parameter S_{CD} (see Fig. 1.5). The order parameter at the position of the ith hydrocarbon atom C_i is given by [263]

$$S_{\mathrm{CD}} = -\frac{2}{3}S_{xx} - \frac{1}{3}S_{yy} \quad , \tag{1.1}$$

where $S_{\alpha\beta}$, $\{\alpha, \beta\} \in \{x, y, z\}$, is the order parameter tensor

$$S_{\alpha\beta} = \left\langle \frac{3}{2}\cos\theta_\alpha \cos\theta_\beta - \frac{1}{2}\delta_{\alpha\beta} \right\rangle \qquad (\alpha, \beta = x, y, z) \quad , \tag{1.2}$$
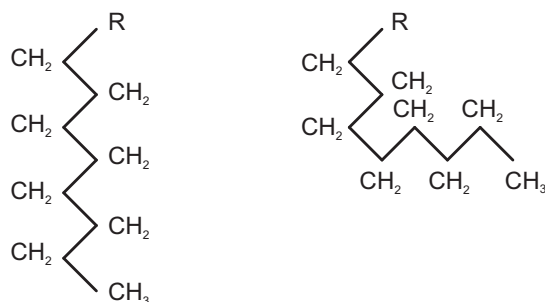
Figure 1.5: Illustration of the lipid order parameter definition. On the left hand side, a saturated lipid hydrocarbon chain (R denotes an arbitrary lipid headgroup) in an all *trans* (i. e., $\alpha \approx 180°$ for all dihedral angles α between four adjacent carbon atoms) conformation, corresponding to a large value of the average deuterium lipid order parameter, is given. On the right hand side, one dihedral angle is in a *gauche* (i. e., $\alpha \approx \pm 60°$) conformation, resulting in a decreased average deuterium lipid order parameter.

θ_α denotes the angle between the αth molecular axis and the bilayer normal, and $\delta_{\alpha\beta}$ is the Kronecker delta. Usually, at position C_i, the vector C_{i-1}-C_{i+1} is taken as the z-direction and the plane spanned by the atoms C_{i-1}, C_i, and C_{i+1} is taken as the y–z plane [263]. The bilayer thickness is furthermore influenced by the tilt of the lipid molecules with respect to the bilayer normal and by a possible intertwining of the lipid chains of the two opposite monolayers.

Due to the weak lipid-lipid interactions with no chemical bonds, but only hydrophobically driven aggregation, lipid bilayers exhibit only a small resistance to bending and are, at normal temperature and pressure, deformed by thermally excited bending undulations and single lipid protrusions. These surface fluctuations and undulatory motions are conveniently described in continuum elasticity theory, where lipid bilayers are modeled as two dimensional sheets with negligible thickness. This approximation is valid as long as the wavelength of the considered bending undulations λ_{und} is larger than the bilayer thickness d. The surface is most easily defined in the Monge[2] parametrization, where the 'height' $z = z(x, y)$ is given as a function of the coordinates x and y.

For membranes under tension [3], the free energy E is given by the product of the area (area segment $dA = dx \, dy \, \sqrt{1 + z_x^2 + z_y^2}$ in the Monge representation) and the surface tension γ [228]:

$$E = \gamma \int dx \, dy \, \sqrt{1 + z_x^2 + z_y^2} \quad . \tag{1.3}$$

Here, the notation $z_x = \frac{\partial}{\partial x} z(x, y)$ and $z_{xx} = \frac{\partial^2}{\partial x^2} z(x, y)$ is used. The free energy of surface fluctuations can be calculated from the free energy difference between the deformed and the flat surface. Expanding the square root in Eq. (1.3), $\sqrt{1 + x} \approx 1 + \frac{1}{2} x$, and keeping in mind that for a flat surface $z_x = z_y = 0$, the free energy of the fluctuations per unit

---

[2] Gaspard Monge, 1746-1818

[3] Although in the simulations only tension-free bilayers are considered, here first the general formula Eq. (3.4) is derived.

area e_fl is [228]

$$e_\mathrm{fl} \;=\; \frac{1}{2}\,\gamma\,(z_x^2 + z_y^2) \quad . \tag{1.4}$$

Bending undulations of the membrane can be described in terms of the mean and Gaussian curvatures $H = \frac{1}{2}(\kappa_1 + \kappa_2)$ and $K = \kappa_1 \kappa_2$, which are the invariants of the curvature tensor under rotation of the coordinate system [228]. κ_1 and κ_2 are the two prinicipal, i. e., extremal, curvatures of the membrane. Accounting for the rotational invariance, the free energy of curvature per unit area e_c, up to second order in the principal curvatures, can be most generally written as [103, 228]

$$e_c \;=\; \frac{1}{2}\,k_c\,(\kappa_1 + \kappa_2 - 2c_0)^2 + k_s\,\kappa_1\kappa_2 \tag{1.5}$$

$$\;=\; 2k_c\,(H - c_0)^2 + k_s K \quad . \tag{1.6}$$

The first summand comprises the energy contribution for deviations of the bilayer shape from the spontaneous curvature c_0 and the second term represents the energy of saddle-shaped deformations. The bending or curvature modulus k_c and the saddle splay modulus k_s both have the dimension of energies. For simulations of nanoscopic, symmetric bilayers under periodic boundary conditions (see Section 2.2.5), the spontaneous curvature is zero and only bending undulations, but no saddle splay deformations occur (see, e. g., [22]). These terms are therefore omitted in the following.

Choosing the Monge representation, the Gaussian curvature for a nearly flat surface ($z_x \ll 1$ and $z_y \ll 1$) can be expressed as $H \approx \frac{1}{2}(z_{xx} + z_{yy})$ [228]. The curvature free energy per unit area then becomes

$$e_c = \frac{1}{2}\,k_c\,(z_{xx} + z_{yy})^2 \quad . \tag{1.7}$$

The total free energy of the undulations per unit area, arising from both bending and fluctuations, is the sum of e_fl and e_c:

$$e_\mathrm{und} = \frac{1}{2}\,\left(k_c\,(z_{xx} + z_{yy})^2 + \gamma\,(z_x^2 + z_y^2)\right) \quad . \tag{1.8}$$

In Fourier space ($z(\vec{r}) = c \sum_{\vec{k}} \tilde{z}(\vec{k}) \exp(i\,\vec{k}\vec{r})$, with $\vec{r} = (x, y)$, $\vec{k} = (k_x, k_y)$, and c an appropriate normalization constant), the free energy per unit area simplifies to ($k := |\vec{k}|$)

$$e_\mathrm{und} = \frac{1}{2}\,\left(k_c\,k^4 + \gamma\,k^2\right)\tilde{z}(k)^2 \quad . \tag{1.9}$$

Considering the surface energy as a generalization of the harmonic oscillator problem (Gaussian model, see, e. g., [22, 228]), the average energy of each wave vector mode is $E_\mathrm{und} = e_\mathrm{und} A = \frac{1}{2}k_B T$ according to the equipartition theorem. A is the area of the simulation box, k_B the Boltzmann constant and T the temperature. The average mode amplitudes in Fourier space are then given by

$$\tilde{z}(k)^2 = \frac{k_B T}{A}\,\frac{1}{k_c k^4 + \gamma k^2} \quad . \tag{1.10}$$

As the surface tension γ in a self-assembled bilayer is zero, the bending modulus k_c can be obtained from a fit of the spectrum (Eq. (1.10)).

A quantity closely related to the bending elasticity is the area compressibility $K_A = \kappa_T^{-1} = \frac{\partial \gamma}{\partial A}$, with the isothermal compressibility κ_T, the surface tension γ, and the bilayer area A. In constant pressure simulations, it can be calculated from the mean square fluctuations σ_A^2 of the area of the system according to

$$\sigma_A^2 = \frac{k_B T}{K_A} A \quad .$$

(1.11)

This equation can be derived from general ensemble theory for systems of finite size by relating ensemble averages of observables obtained in two different thermodynamic ensembles[4] [4]. However, values of the area compressibilities obtained by Eq. (1.11) might be inaccurate, as the error of the area fluctuations in equilibrated simulation systems will be relatively large [72]. Additionally, application of algorithms like the Berendsen coupling scheme [16] (this coupling scheme yields no defined thermodynamic ensemble, see Section 2.2.3), and the use of periodic boundary conditions (see Section 2.2.5) might both suppress area fluctuations in the system and thereby bias the results. Together with a possible undersampling of the fluctuations caused by the limited simulation time, all this would lead to an imprecise result for K_A.

1.1.2 Pressure Distribution

Lipid bilayers are characterized by large lateral stresses resulting from packing constraints inside the bilayer and from molecular interactions of the lipids and the surrounding solvent. These internal forces vary strongly with the bilayer depth and are generally described within the formalism of local membrane pressures.

For a macroscopic system, pressure is defined either mechanically as the normal force acting per unit area, or thermodynamically as the partial derivative of the free energy E of the system with respect to the volume V at constant entropy, i.e., without exchange of heat:

$$p = -\left(\frac{\partial E}{\partial V} \right)_T \quad .$$

(1.12)

For homogeneous, isotropic systems, these two definitions are equivalent (see, e.g., [14, 102]). In order to generalize this concept to the nanoscopic systems investigated in atomistic simulations, a microscopic definition of pressure has to be found that in the limit of large ensembles and long time averages equals the macroscopic definition of pressure.

---

[4]These ensembles differ by the parameter that is kept constant: in the first ensemble, the extensive variable F (here: the area A) is fixed, while in the second ensemble, the conjugate intensive variable f (here: the surface tension γ) is kept constant.

In the mechanical definition, the local pressure in a system can be written as a tensor and is given by the sum of kinetic and configurational contributions[5]

$$\mathbf{p}_{\text{local}} = \mathbf{p}_{\text{kin}} + \mathbf{p}_{\text{config}} \quad . \tag{1.13}$$

The kinetic contribution can be easily evaluated in terms of the velocities of all particles within a confined volume. For the configurational pressure in a small volume element ΔV at position $\vec{r}$, Schofield and Henderson [230] derived a microscopic description

$$p_{\text{config}}^{\alpha\beta}(\vec{r}) = \frac{1}{\Delta V} \left\langle \sum_i F_i^{\alpha} \int_{C_{0i}} \delta(\vec{r} - \vec{r}_c) \, (d\vec{r}_c)^{\beta} \right\rangle \quad , \tag{1.14}$$

where the contour integral C_{0i} runs from a reference point $\vec{r}_0$ to the position $\vec{r}_i$ of particle i, and $d\vec{r}_c$ is a line element of this contour at position $\vec{r}_c$. Both, the reference point and the contour can be chosen arbitrarily. The sum is taken over all particles i in the system. $\vec{F}_i$ is the total force acting on particle i and $\{\alpha, \beta\} \in \{x, y, z\}$. The brackets indicate an ensemble average. Hence, the configurational pressure at position $\vec{r}$ is a sum over contributions from all particles i in the system, for which the corresponding contours C_{0i} pass through the volume element ΔV at position $\vec{r}$ [244]. In case of only pairwise additive interactions in the system, Eq. (1.14) can be written as [230, 244]

$$p_{\text{config}}^{\alpha\beta}(\vec{r}) = -\frac{1}{\Delta V} \left\langle \sum_{i<j} F_{ij}^{\alpha} \int_{C_{ij}} \delta(\vec{r} - \vec{r}_c) \, (d\vec{r}_c)^{\beta} \right\rangle \quad , \tag{1.15}$$

where $\vec{F}_{ij}$ are the forces acting between particles i and j. A popular choice for the contour C_{ij} in Eq. (1.15) is the Irving-Kirkwood (IK) contour, connecting the particles at positions $\vec{r}_i$ and $\vec{r}_j$ by a straight line[6].

For a semi-isotropic lipid bilayer in the liquid disordered phase, the configurational stress tensor is approximately diagonal [85]. Using the IK contour, the local pressure as a function of the bilayer normal (taken as the z-direction) can be calculated by dividing the bilayer in thin slices of thickness Δz and volume ΔV parallel to the membrane plane [142]:

$$\mathbf{p}_{\text{local}}(z) = \frac{1}{\Delta V} \sum_{i \in \text{slice}} \langle m_i \vec{v}_i \otimes \vec{v}_i \rangle - \frac{1}{\Delta V} \sum_{i<j} \left\langle \vec{F}_{ij} \otimes \vec{r}_{ij} \, f(z, z_i, z_j) \right\rangle \quad . \tag{1.16}$$

---

[5]Note, that the configurational contribution, and therefore the pressure tensor, is not uniquely defined, as a divergence free term can be added without changing the measurable force acting per unit volume (see, e. g., [14]).

[6]The IK contour is only suited for use with m-body interactions with finite number m. Therefore, in simulations applying lattice summation methods to evaluate electrostatic interactions (see Section 2.2.2), other contours, like the one suggested by Harasima [94], have to be used. To circumvent this problem, results for local pressures given in this thesis have been computed in a two-step process, where first the evolution of the system was simulated applying lattice summation methods, and only in a second step local pressures were calculated applying a cutoff for electrostatic interactions. This procedure has been shown to converge towards the correct results, as long as a large enough cutoff is used [244].

For the kinetic energy term, only the particles in the slice at position z contribute, while for the configurational term interactions between all particle pairs in the system have to be included. The z-coordinate, mass, and the velocity of particle i, and the force and the distance between particles i and j are denoted by z_i, m_i, $\vec{v}_i$, $\vec{F}_{ij}$, and $\vec{r}_{ij}$, respectively. The function $f(z, z_i, z_j)$ is the ratio between the length of the contour C_{ij} (Eq. (1.15)) within the slice at position z and the full length of this contour. It can be expressed as [85]

$$f(z, z_i, z_j) = \begin{cases} \Theta(z_i - z)\,\Theta(z + \Delta z - z_i) & \text{for} \quad z_i = z_j \\ \frac{1}{z_j - z_i} \int_{z_i}^{z_j} d\zeta\, \Theta(\zeta - z)\,\Theta(z + \Delta z - \zeta) & \text{otherwise,} \end{cases} \tag{1.17}$$

where $\Theta(z)$ denotes the Heaviside step function, with $\Theta(z) = 0$ for $z < 0$, $\Theta(0) = 1/2$, and $\Theta(z) = 1$ for $z > 0$. The local lateral and normal pressures are defined as $p_L(z) = (p_{xx}(z) + p_{yy}(z))/2$ and $p_N(z) = p_{zz}(z)$. The latter is approximately constant due to the translational invariance within the bilayer plane. The surface tension can be obtained from $\gamma = \int (p_N(z) - p_L(z))\, dz$.

As self-assembled lipid bilayers are only a few nanometer thick and the sum over all forces acting within the bilayer is zero, it is difficult to determine local pressures experimentally, and up to now, only quantitative measurements of the pressure distribution in lipid bilayers have been achieved [121, 258]. In many theoretical studies it has been found that large lateral pressures of several hundred bars act inside lipid bilayers[7] (see, e. g., [142]). These pressures result from a balance of forces acting at different depths inside the bilayer and adding up to zero only if integrated across the whole bilayer (zero surface tension). The main contributions to the pressure originate from forces due to the hydrophobic effect, striving to minimize the contact between the apolar lipid chains and the polar water molecules and therefore decreasing the area per lipid ($\Delta p(z) = p_L(z) - p_N(z) < 0$), and forces due to steric interactions between membrane components, expanding the bilayer ($\Delta p(z) > 0$)[8].

An idealized, not scalable pressure profile is given in Fig. 1.6. The profile is symmetric due to the symmetry of the bilayer in the direction of the bilayer normal. Within the hydrophobic core of the bilayer the difference between the lateral and normal pressure Δp is positive due to an entropic repulsion resulting from steric interactions of the lipid hydrocarbon chains[9]. At the hydrophobic-hydrophilic interface, where the glycerol backbones of the lipids are located, a large interfacial tension ($\Delta p < 0$) is caused by the hydrophobic

---

[7]A simple estimate of magnitude of lateral pressures in the bilayer has been given by Cantor [36]: As the surface tension of a lipid bilayer is zero, the interfacial tensions at each monolayer of typically $\gamma_{\text{interface}} \approx 0.05\,\text{N/m}$ have to be compensated by the entropic repulsion of the chains. Assuming a hydrophobic thickness of a bilayer of $d \approx 3\,\text{nm}$, the average lateral pressure in the bilayer core is $2\gamma_{\text{interface}}/d \approx 330\,\text{bar}$.

[8]Although not absolutely precise, the difference of pressures $\Delta p(z) = p_L(z) - p_N(z)$ as a function of the membrane normal is commonly referred to as the lateral pressure profile and this convention will be adopted in the following. The use of the pressure difference instead of only the lateral pressure is justified, as the normal pressure in lipid bilayers is approximately constant due to the translational invariance within the bilayer plane.

[9]The central maximum of Δp at $z = 0$ is related to the density minimum of lipid molecules in the center of lipid bilayers (Fig. 3.1). In this region, positive contributions to the pressure due to steric repulsions (part of the Lennard Jones interactions, see Section 2.2.1) are reduced, but also the absolute value of the negative contributions from bonded interactions (see Section 2.2.1) are decreased (Fig. 4.8).
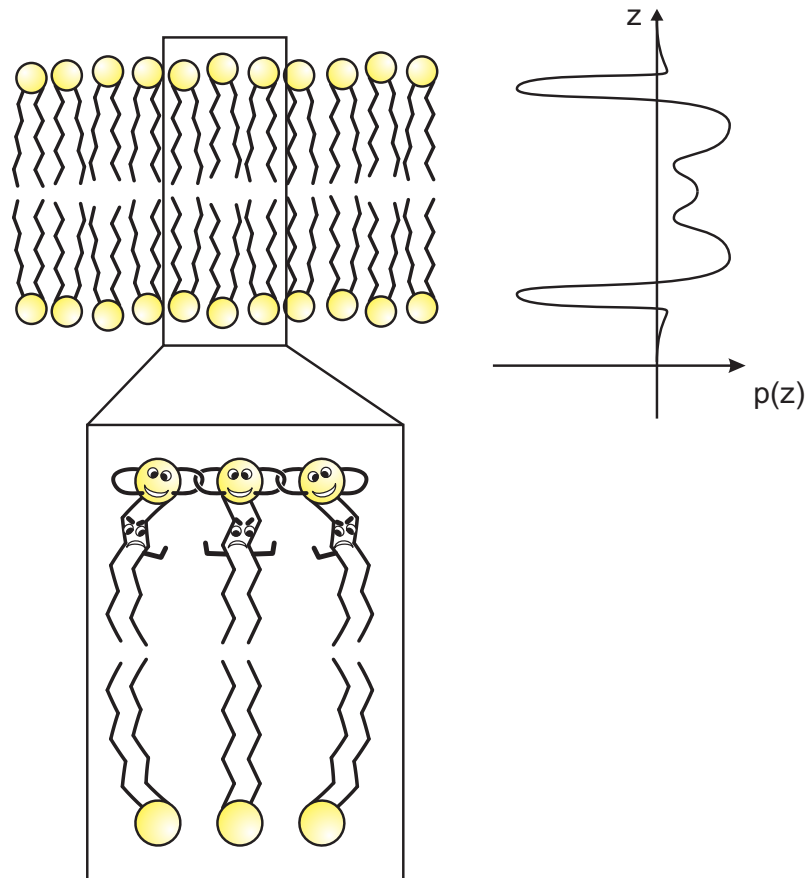
Figure 1.6: Illustration of the effective lateral pressures inside lipid bilayers. The upper panel shows an idealized, not scalable pressure profile (right hand side; adapted (modified) from [34]) and the spatial localization of the different peaks inside the bilayer (left hand side). The cartoon in the lower panel depicts the resulting effects for the lipids. Please note, that – although not shown in the illustration – water molecules play an important role for the overall shape of the lateral pressure profile.

effect described above. In the lipid headgroup region, interactions between the polar or charged lipid headgroups and (oriented) solvent molecules result in a small, positive peak, before the pressure difference drops to zero in the bulk water region.

1.2 Membrane Proteins

Membrane proteins are an important constituent of biological membranes. Depending on the membrane type, they can account for up to 75 mass-% of the membrane. Two different classes can be distinguished: peripheral membrane proteins, that are only attached to the surface of the membrane, and integral membrane proteins, stretching across the hydrophobic core of the lipid-protein layer of biological membranes. The transmembrane part of integral membrane proteins is either made up by a bundle of α-helices, or by β-sheets (β-barrel proteins) forming a transmembrane pore (Fig. 1.7).
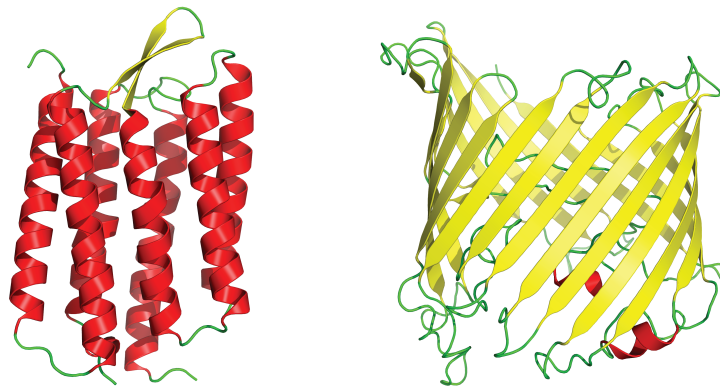
Figure 1.7: Examples for an α-helical (left, subunit of bacteriorhodopsin, protein data bank (PDB) entry 1KGB [69]) and a β-barrel (right, subunit of the sucrose-specific porin, PDB entry 1A0S [76]) membrane protein. The color coding refers to the secondary structure: α-helices are colored red, β-sheets yellow, and coil elements green.

Membrane proteins play an important role in the active and passive transport of biological substances – especially of ions – across cell walls, in the excitation and propagation of nerve pulses, and in cell-cell recognition. Besides, they act as receptors and enzymes, and they constitute the structural elements linking the lipid-protein layer to the cytoskeleton and the extracelluar matrix. The relevance of membrane proteins becomes evident by the fact that they account for $\sim 70\%$ of all known drug targets [147]. As proteins are very sensitive to their local environment, a modulation of membrane protein function can not only be affected by a specific binding of drugs to these proteins, but probably also by a change in the composition and the properties of the lipid matrix surrounding the protein (see, e. g., [147]).

1.3 Anesthesia

The term anesthesia originates from the greek word $\alpha\nu\alpha\iota\sigma\theta\eta\sigma\iota\alpha$, that describes the insensitivity of an organism to external stimuli. Two kinds of anesthesia can be distinguished: general and local anesthesia. Drugs causing general anesthesia act at the central nervous system, i. e., the brain and the spinal cord, and usually induce a reversible loss of consciousness. Local anesthetics act at the peripheral nervous system and selectively block the formation and propagation of nerve pulses in a spatially limited part of the body. In this thesis, only general anesthesia is considered.
The first public demonstration of anesthesia was achieved in 1846 by William Morton using diethyl ether as anesthetic. Since then, anesthesia has become a well established and widely used technique in medicine to keep patients free of pain not only during surgery, but also in intensive care.
General anesthesia is a complex phenomenon involving loss of consciousness (hypnosis), analgesia, amnesia, muscle relaxation, and suppression of reflexes. Despite an intensive

research, the underlying molecular mechanisms are still not understood. Today it is generally assumed that anesthetics either integrate into the lipid matrix of neuronal membranes, thereby modulating their physical properties, or that they bind specifically to membrane proteins involved in signal transduction at synapses. In both cases, they could hinder the propagation of nerve pulses and thereby induce anesthesia.

Molecules of very different structures and compositions, ranging from the inert noble gas xenon to more complex molecules like sevoflurane (Fig. 1.8), act as anesthetics. Corresponding to their way of application, these drugs are commonly divided into inhalational and intravenous anesthetics. All of them have different anesthetic (e. g., mainly analgetic, or only hypnotic, etc.) as well as different side effects; and as in general anesthetic effects are additive, usually a combination of drugs is used to maximize the desired effects and to minimize side effects in clinical applications.

Around 1901, Meyer and Overton discovered that the anesthetic potency of a drug correlates with its lipophilicity [165, 194]. This so-called Meyer-Overton correlation is the only common property found for almost all anesthetics up to now and suggests a hydrophobic site of anesthetic action. According to this rule, the anesthetic potency of a homologous series of molecules increases with increasing carbon chain length. However, there exists a cutoff length, where potency suddenly drops. For the 1-alkanols considered in this thesis, the cutoff length is approximately 12 carbon atoms, i. e., dodecanol (see, e. g., [206]).

1.3.1 Lipid-Mediated versus Protein-Binding Models

Following the work of Meyer and Overton, many models for the mechanism of general anesthesia have been suggested. According to the proposed site of action they can be grouped into lipid(-mediated) and protein-binding models[10]. Here, only the most recent examples of both classes will be briefly presented.

Based on the strong correlation between the lipophilicity and the anesthetic potency of a drug, and considering the large diversity of anesthetics, with even the noble gas xenon being a potent anesthetic, lipid theories assume a cooperative physical mechanism for anesthesia with the lipid layer of the plasma membrane as the site of anesthetic action. A recent example for such a lipid model was suggested by Heimburg and Jackson: they questioned the established Hodgkin-Huxley model [108] for signal propagation along neurons and instead proposed a thermodynamically motivated model, where nerve pulses travel as solitons along neuronal membranes [99]. Within this framework, anesthesia is explained by an anesthetic-induced decrease of the membrane phase transition temperature (see Section 1.1) that impedes soliton propagation [100, 101].

The basis for lipid-mediated theories is the assumption that membrane proteins are sensitive to their local environment. In this way, anesthetic-induced changes of the physical properties of the host lipid bilayer can alter the activity of membrane proteins and thereby suppress signal transduction. A recent example of such a theory will be presented in more

---

[10]In principal, the theories of Miller [167] and Pauling [197], where anesthesia is explained by the formation of clathrates in cell fluids, represent a third class of models. However, no evidence for such a model has been found and these theories will not be considered here.

Figure 1.8: Examples of general anesthetics. The molecular weights and volumes of different anesthetics can vary by as much as a factor of 10 [275].

detail in Section 1.3.2.

In protein-binding theories, a binding of drugs to membrane proteins is assumed to cause anesthesia. Many different ion channels and protein receptors have been suggested as potential anesthetic targets (for a review, see [275]), the most likely targets being γ-**a**mino**b**utyric **a**cid type **A**($GABA_A$) receptors , two-pore K^+ channels, and **N-m**ethyl-

D-aspartate (NMDA) receptors [77]. The greatest success for this kind of theories was the observation that the activity of the soluble protein luciferase from the North American firefly *Photinus pyralis* was suppressed by various anesthetics without any lipids present [78]. However, firefly luciferase is not involved in any kind of signal transduction. As the universality of the Meyer-Overton correlation suggests a unitary mechanism of anesthetic action, arguments against protein-binding theories can be found in the large diversity of anesthetics (see Section 1.3): it seems unlikely that all these chemically very different molecules bind in the same way to membrane proteins. Besides, most anesthetics have been found to have some effect on some protein receptor, but no channel could be identified that is influenced in the same way by all anesthetics.

1.3.2 Anesthetic Mechanism via Changes in the Local Pressure Distribution in Biological Membranes

As the results presented in this thesis are discussed within the framework of the lipid-mediated model for anesthesia developed by R. Cantor in 1997 [33–37], this work will be briefly presented in the following.

As explained in Section 1.1.2, biological membranes are characterized by large lateral stresses of several hundred bars varying non-monotonously with depth inside the membrane. Applying a statistical lattice model, Cantor has shown that the inclusion of 1-alkanols into lipid bilayers modifies these pressures in a non-uniform manner. Though the relative changes obtained in this way at clinical anesthetic concentrations are only small, the absolute changes in the pressure are still large due to the magnitude of the local pressures [33]. Provided that intrinsic membrane proteins exist in at least two different conformations r and t (interpreted as an open and a closed channel form) with varying difference of the cross section areas in the direction of the membrane normal, i. e., $\Delta A(z) = A_t(z) - A_r(z) \neq \mathrm{const.}$, an anesthetic-induced modification of the bilayer pressure profile will shift the thermodynamic equilibrium between different conformations of the protein, as illustrated in Fig. 1.9. By equating the chemical potentials μ_r and μ_t of both protein conformations for the case with and without anesthetics independently, and assuming that $\Delta A(z)$ is unaffected by the pressure redistribution caused by the anesthetics, Cantor derived a quantitative description of this effect (for the detailed formalism, see Section 4.4.2). In subsequent calculations he demonstrated that even small variations in lipid bilayer composition or small amounts of additives could change the equilibrium between two different conformations of membrane proteins, modeled by a simple geometric shape [36, 37]. However, the occurence of such a change depended strongly on the assumed protein shape and the additive.

The attractiveness of this model lies in the fact that for the first time a full mechanistic explanation for anesthesia has been given. Besides, the anesthetic effect is traced back to large changes in the pressure, and not – like in previously suggested lipid models – to only small variations in lipid properties like, e. g., the bilayer volume, that could also easily be achieved by an increase in temperature (which does of course not induce anesthesia). Furthermore, within this model two known exceptions to the Meyer-Overton correlation, the
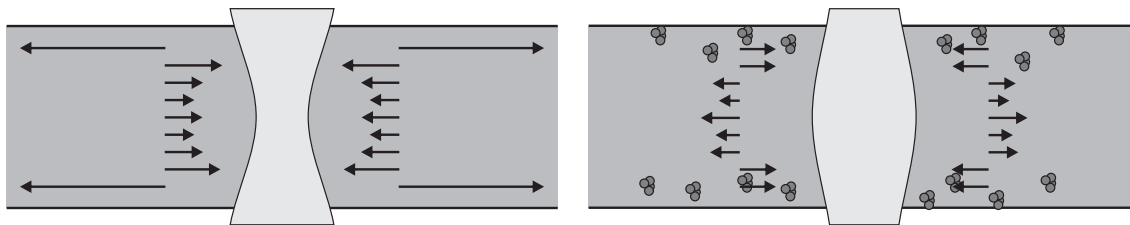
Figure 1.9: Mechanism of anesthesia as suggested by R. Cantor. The two drawings depict a lipid bilayer (grey) with an embedded membrane protein (light grey). The lateral pressure distribution is indicated by the black arrows. On the left hand side, without anesthetics, the large interfacial tension (outward pointing arrows) at the bilayer water interface and the entropic repulsion (inward pointing arrows) of the lipid hydrocarbon chains force the protein into a more open conformation in the outer bilayer region and a narrow conformation within the bilayer center. With anesthetics (small, dark grey molecules; right hand side), the pressure distribution inside the bilayer is changed and the protein adapts its shape accordingly. Please note, that the changes of the pressure profile upon addition of anesthetics are not the real changes, but are chosen here in order to illustrate the mode of operation.

cutoff in anesthesia for 1-alkanols and the anomalously low potency of very hydrophobic molecules, has been reproduced [33].

1.3.3 Pressure Reversal

General anesthesia can be reversed by the application of external pressure. First hints to this effect were found in experiments on bacterial luminescence [115], before in 1950 Johnson and Flagler [116] showed that tadpoles that had been anesthetized with alcohol resumed swimming after application of high external pressures between 140 and $350 \, \mathrm{bar}$. The effect on unnarcotized animals was an increased activity up to pressures of $140 \, \mathrm{bar}$, but paralysis at higher pressures. Similar pressure reversal effects were later reported applying other anesthetics to tadpoles [93] and to newts and mice [139]. Investigations of the dependence of pressure reversal on the anesthetic concentration let to the conclusion that pressure reversal is presumably not due to a decrease of the partition coefficient of anesthetics inside the membrane [166]. This result was supported by experiments of Trudell et al. [272], who showed that small molecules were not displaced from phospholipid membranes by application of external pressure.

2 Molecular Dynamics Simulations

2.1 Overview

In molecular dynamics (MD) simulations, the properties and the time evolution of many-particle systems are investigated by solving Newton's equations of motion

$$\vec{F}_i = m_i\,\vec{a}_i \qquad\qquad i = 1,\ldots,N \qquad\qquad (2.1)$$

for all atoms in the system simultaneously. In this equation, $\vec{F}_i$ is the total force acting on atom i, m_i is the mass of this atom, and $\vec{a}_i = \frac{d^2}{dt^2}\,\vec{x}_i$ denotes its acceleration. The total number of atoms in the system is N. In principle, such kind of deterministic approach has already been anticipated by Laplace at the beginning of the 19th century [55], but an analytical solution to the N-body-problem is not possible for $N \geq 3$ and only with the invention of computers a numerical solution for many particle systems became feasible.

The first MD simulations were performed in 1957 on two-dimensional hard spheres by Alder and Wainwright [2], who also outlined the theoretical basics of the method [3]. In the following, liquid argon [211], water [212], and also larger molecules [226], as well as systems containing ions [300] have been simulated. The method was subsequently applied to investigate the mobility of a folded protein first in vacuum [164], and later also in a solvent environment [283, 285, 286]. In an extremly long-time simulation of $1\,\mu\text{s}$, intermediate states of folding of a peptide in solution could be identified [60]. Simulations of preformed lipid bilayers were first accomplished in 1982 [277], before later also their self-assembly could be demonstrated [157].

Today, the technique of MD simulations is applied to a wide range of diverse biomolecular problems and technical applications. The first include the simulation of lipid vesicles, lipid bilayers, and membrane fusion, of large protein complexes in their native environment (e. g., [53]), of enzyme activity [23], and even of entire viruses [82]. The latter addresses technical problems like for example cracking in metals. Systems containing about 10^6 atoms can be simulated for time intervals of hundred nanoseconds, where the limiting factor is the available computing power. It is now generally acknowledged, that the molecular environment – water (with ions) in most cases – has a large influence and therefore has to be included in the simulations, although its explicit simulation is very time-consuming and usually accounts for about 90% of the overall computational cost. In order to avoid unwanted boundary effects when simulating nanoscopic samples, most simulations are currently carried out using periodic boundary conditions (see Section 2.2.5), enabling the use of effective techniques to calculate long-range electrostatic interactions fast and accurately (see Section 2.2.2). Sophisticated MD simulation packages have been developed, the four most popular ones being CHARMM (Chemistry at

Harvard Macromolecular Mechanics [29]), GROMACS (Groningen Machine for Chemical Simulations [18, 143, 278]), GROMOS (Groningen Molecular Simulation [281, 284]), and NAMD (Nanoscale Molecular Dynamics [202]).

The evaluation of interactions between the atoms is usually done using so-called force fields (see Section 2.2.1). In short, such a force field is a collection of interaction parameters and semi-empirical rules allowing to evaluate the forces between different types of atoms in a simple manner. Various force fields have been designed by several research groups, that are optimized for use under different environments (i.e., hydrophilic/hydrophobic solvent) and conditions (i.e., pressure, temperature). The best-known examples are probably AMBER [47, 198, 294, 295] and its generalization GAFF [241, 293], CHARMM [29, 152, 153], GROMOS [281, 284], and OPLS [118, 119]. Also, different models for the simulation of water molecules have been suggested, the most common ones being the (extended) simple point charge (SPC(/E)) model [15, 17], and the transferable intermolecular potential with three (TIP3P) or with four (TIP4P) particles [117].

Limitations of MD simulations result from the description of the atoms as classical particles. Thereby, the rapid movements of the light hydrogen atoms, fast vibrational motions, and bond-length fluctuations, where quantum effects cannot be neglected, are not treated adequately. Likewise, systems at very low temperatures (0-10 K) are not evaluated correctly. As a covalent bond is approximated by a simple harmonic spring between two atoms, chemical reactions requiring bond breaking cannot be simulated in conventional MD simulations.

An open challenge is the adequate sampling of the conformational space within the limited simulation time. Only if a statistically representative ensemble is sampled, macroscopic quantities can be correctly calculated as ensemble averages over the MD trajectory. In general, the energy landscape of a many-particle system is a rugged surface with many local minima and maxima, and MD simulations easily get trapped in a small part of the vast conformational space. Methods to address this problem involve smoothening of the potential-energy surface (e. g., [111, 203]), scaling of system parameters like atomic masses or the temperature [129, 155], or performing simulations of multiple copies of the same system at, e. g., different temperatures or pressures [168, 247, 248], allowing an exchange or interaction between the system replicas. An overview over these techniques has been given by van Gunsteren and Berendsen [280].

A possibility for extending the accessible time scales in simulations that has become very popular in the last years are coarse-grained (CG) molecular dynamics simulations. The idea of coarse-graining is to neglect unimportant or uninteresting degrees of freedom, such that less accuracy, but a faster time evolution of the system is achieved (see also Section 8.1).

Certainly, simulations are not meant to replace experiments, but to complement them. Simulations are important where "experiments are impossible (collision of stars, weather forecast), dangerous (flight simulation, explosion simulation), expensive (high pressure simulation, wind channel) or blind (many properties cannot be observed on very short time scales and very small space scales)" [280]. They give valuable details in the interpretation of experimental results, can be used to make semi-quantative predictions, and allow interpolation of experimental results to different environmental conditions.

As can be seen from this short overview, MD simulations are a large and active field of research and involve the application of many different techniques contributing in the

simulation algorithm as well as in the post-simulation trajectory analysis. A detailed description of all facets would go beyond the scope of this thesis and only the mechanisms applied in the presented simulations will be discussed in the following.

2.2 Methods

Any many particle system is completely described by the time-dependent Schrödinger equation

$$\widehat{H}\Psi = i\hbar\,\partial_t \Psi \quad , \tag{2.2}$$

with the Hamilton operator $\widehat{H}$, the wave function Ψ, and Planck's constant $h = 6.626 \times 10^{-34}$ Js $= 2\pi\hbar$. However, this equation cannot be solved analytically for more than two particles. For larger systems, approximations like the Born-Oppenheimer approximation [28], in which the motion of the light electrons and of the heavier nuclei are separated, have to be used. The basis of this approximation is the larger inertia of the nuclei as compared to the electrons, but the same (Coulomb) forces acting on both, resulting in a much slower motion of the nuclei. The electrons follow the motion of the nuclei almost instantaneously. Using this approximation, the solution of the Schrödinger equation can be divided into two-steps, first considering the electron motion for fixed positions of the nuclei and afterwards solving the Schrödinger equation for the nuclei moving in an effective potential.

In MD simulations, electrons are supposed to be in their ground state. They are not represented as explicit particles, but contribute to the potential in which the nuclei (referred to as atoms in the following) move. The atoms are treated as classical particles, obeying Lagrange's equations of motions. Interactions between atoms are assumed to depend only on the instantaneous coordinates of the atoms, such that the forces acting between different atoms are conservative, i. e., they can be calculated as the derivative of a potential V. This leads to Newton's equations of motion

$$\vec{F} = -\nabla_{\vec{r}} V(\vec{r}) = m\,\vec{a} \tag{2.3}$$

for the interacting atoms. The potential V is usually approximated by semi-empirical force fields (see Section 2.2.1).

Various algorithms have been developed to solve the equations of motion numerically and thereby follow the time evolution of a many-particle system. In general, any such algorithm should be time-reversible, as also the equations of motion are time-reversible, and it should conserve the phase space volume (Liouville theorem), a necessary precondition for energy conservation. From a computational point of view, the possibility to use a large time step at high accuracy is desirable.

The two most popular algorithms are probably the Verlet [291] and the equivalent leap-frog [107] integration schemes. The Verlet [291] algorithm can be derived from the Taylor

expansion of the atom coordinates at times $t - \Delta t$ and $t + \Delta t$

$$r(t + \Delta t) \;\; = \;\; r(t) + v(t)\Delta t + \frac{F(t)}{2\,m}\Delta t^2 + \frac{1}{3!}\frac{d^3 r}{dt^3}\Delta t^3 + \mathcal{O}(\Delta t^4) \qquad (2.4)$$

$$r(t - \Delta t) \;\; = \;\; r(t) - v(t)\Delta t + \frac{F(t)}{2\,m}\Delta t^2 - \frac{1}{3!}\frac{d^3 r}{dt^3}\Delta t^3 + \mathcal{O}(\Delta t^4) \qquad . \qquad (2.5)$$

It is assumed that the forces are constant during the small integration time step Δt. Adding up these two equations gives the defining equation for the Verlet algorithm [291]

$$r(t + \Delta t) = 2r(t) - r(t - \Delta t) + \frac{F(t)}{m}\Delta t^2 + \mathcal{O}(\Delta t^4) \qquad . \qquad (2.6)$$

The velocity of the atom is obtained from

$$v(t) = \frac{r(t + \Delta t) - r(t - \Delta t)}{2\Delta t} + \mathcal{O}(\Delta t^2) \qquad . \qquad (2.7)$$

The leap-frog algorithm makes use of half time steps and is determined by the two equations

$$r(t + \Delta t) \;\; = \;\; r(t) + v(t + \Delta t/2)\,\Delta t \qquad (2.8)$$

$$v(t + \Delta t/2) \;\; = \;\; v(t - \Delta t/2) + \frac{F(t)}{m}\,\Delta t \qquad . \qquad (2.9)$$

Although the leap-frog algorithm evaluates the coordinates and velocities at times differing for half a time-step, it is preferred over the Verlet algorithm, as in the latter the positions of the atoms do not depend on the particle velocities, rendering velocity scaling in order to keep the temperature constant (see Section 2.2.3) more difficult.

2.2.1 Force Fields

A crucial and non-trivial task in MD simulations is the evaluation of the potential V, from which the forces acting on the atoms are derived (Eq. (2.3)). This is mostly done in terms of so-called force fields, where parameters describing the interactions between all atoms are stored.

Ideally, force field parameters should be derived from quantum-mechanical ab initio calculations, be transferable between similar molecules, be robust against changes in the conditions (e. g., pressure, temperature) and in the environment, and accurately reproduce experimental results. In practice, most force fields are built on a semi-empirical approach, in the sense that a chemically motivated, preferably simple shape of the potential is assumed and free fit parameters are adjusted to reproduce experimental results. For calibration, mostly small molecule properties, like for example solvation free enthalpies in the case of the GROMOS96 [284] force field, are used.

The terms contributing to the potential can be subdivided into bonded interactions between neighbouring atoms and non-bonded interactions between any two atoms:

$$V(r_1, \ldots, r_N) \;\; = \;\; V_{\text{bonded}} + V_{\text{non-bonded}} \qquad . \qquad (2.10)$$

Neighboring atoms are defined as atoms that are connected via three (third neighbors) or less (first, second neighbors) covalent bonds. For simplicity, non-bonded interactions between first and second neighbors are excluded in most force fields. Bonded interactions are composed of energy terms for covalent bonds, angles, and improper and proper dihedrals (see also Fig. 2.1):

$$V_{\text{bonded}} = V_{\text{bonds}} + V_{\text{angles}} + V_{\text{imp.dih.}} + V_{\text{prop.dih.}} \tag{2.11}$$

$$\stackrel{\text{e.g.}}{=} \sum_{\text{bonds}} \frac{1}{2} K_b (b - b_0)^2 + \sum_{\text{angles}} \frac{1}{2} K_\theta (\theta - \theta_0)^2$$

$$+ \sum_{\text{imp.dih.}} \frac{1}{2} K_\xi (\xi - \xi_0)^2 + \sum_{\text{prop.dih.}} K_\varphi (1 + \cos(n\varphi - \delta)) \quad . \tag{2.12}$$
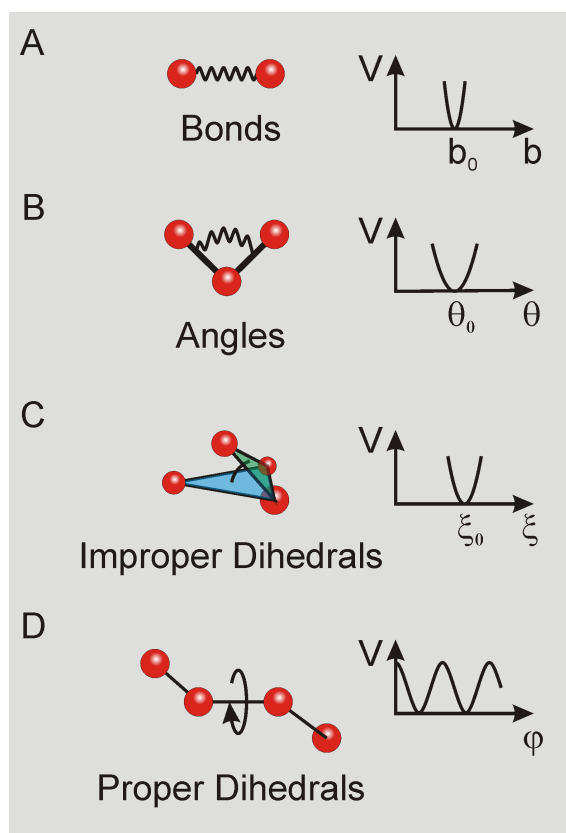
Figure 2.1: Schematic representation of all bonded interactions and the corresponding potential terms.

The explicit shape (Eq. 2.12) assumed for the interactions can vary depending on the force field used. In general, the quantum character of covalent bonds is neglected and the bonds are approximated by harmonic springs with force constants K_b and equilibrium length b_0 (Fig. 2.1 A). Angles between three atoms are treated in a similar way (Fig. 2.1 B). For neighboring interactions between four atoms, two kind of dihedral terms are defined. Improper dihedrals (Fig. 2.1 C) are designed to maintain the shape of planar ring

groups by confining the dihedral angle ξ to one fixed value ξ_0 using a harmonic potential. For proper dihedrals (Fig. 2.1 D), determining for example the *cis / trans* isomerism of a molecule, several dihedral angles φ can be adopted, allowing for transitions between different molecular structures. Preferences for certain dihedral orientations can be specified by additional 1–4 interaction terms (i. e., interactions between atoms connected via three covalent bonds) in the force field.

Non-bonded interactions include the Lennard Jones and Coulomb potentials between the atoms i and j (see Fig. 2.2):

$$
\begin{aligned}
V_{\text{non-bonded}} \;=\;& V_{\text{LJ}} + V_{\text{Coulomb}} \\
=\;& \sum_{\text{pairs(i,j)}} 4\varepsilon_{ij}\left(\left(\frac{\sigma_{ij}}{r_{ij}}\right)^{12} - \left(\frac{\sigma_{ij}}{r_{ij}}\right)^{6}\right) + \sum_{\text{pairs(i,j)}} \frac{1}{4\pi\varepsilon_0\varepsilon_r}\frac{q_i q_j}{r_{ij}} \quad (2.13)
\end{aligned}
$$
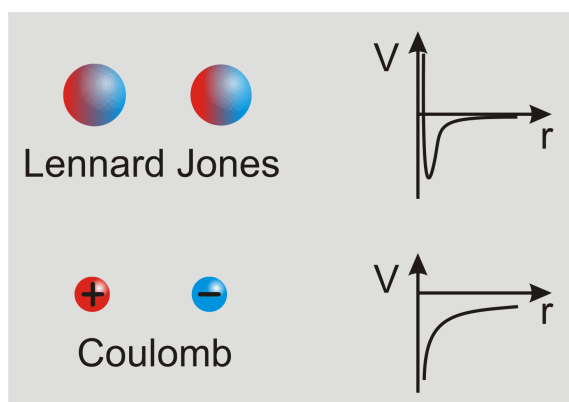
Figure 2.2: Schematic representation of the non-bonded interactions and the corresponding potentials.

Here, ε_{ij} and σ_{ij} are parameters determining the interaction strength and equilibrium distance between the two atoms i and j, respectively, r_{ij} is the interatomic distance, q_i and q_j are the charges of the atoms, and the sum is evaluated over all atom pairs in the system. The Lennard Jones terms comprise the strong repulsion (Pauli repulsion) preventing steric overlap of atom orbitals ($\propto r_{ij}^{-12}$) and the attractive London dispersion contribution (van der Waals interaction) between temporarily induced dipoles ($\propto - r_{ij}^{-6}$). The electrostatic potential is proportional to the charges of the particles and to their reciprocal distance. It should be noticed that in MD simulations also parts of an electron charge can be assigned to single atoms to adequately model the charge distribution in molecules. The dielectric permittivity ε_r enables the inclusion of environmental screening effects. In the representation of the non-bonded contributions chosen here, all terms are pairwise additive. However, this is no necessity and especially for the upcoming inclusion of polarization effects into force fields, higher order moments with interactions between multiple particles will become important.

Two features of current force fields should be mentioned: First, in order to speed-up simulations by a reduction of degrees of freedom, many force fields use a united atom

representation, treating non-polar carbon atoms and the hydrogen atoms bonded to them as single atoms. And second, to account for the chemical environment in which the atoms are located, current force fields often comprise many more atom types than occurring in nature. For example, in the GROMOS 53A6 [193] parameter set, different types of atoms are defined for a carbonyl oxygen, a carboxyl oxygen, a hydroxyl oxygen, an ether oxygen, and a water oxygen. In this thesis, the focus was on the prediction, analysis, and interpretation of average, macroscopic quantities of large biomolecular systems. Therefore, approved force fields from literature have been used. Although artifacts for the partitioning of ethanol into lipid bilayers have been observed (see Chapters 3, 4, and 5), no changes in the employed force fields have been made in order to maintain their internal consistency.

2.2.2 Treatment of Long-Range Interactions

For the calculation of the non-bonded interactions with their unlimited range of action, the sum over all particle pairs in the system has to be evaluated, requiring N^2 computations and making the simulations prohibitively slow for a large number of particles N in the system. Currently, three different methods are mainly employed to circumvent this problem: the truncation of forces or potentials by a spherical cutoff, the treatment of long-range interactions in terms of a reaction field, or the evaluation of the contributing terms by lattice summation methods.

In the cutoff method, all interactions with particles beyond a distance r_{cutoff} are set to zero. It is generally assumed (see, e. g., [229]) that such a truncation of the forces or the interatomic potentials by a sufficiently large cutoff (usually around $1\,\text{nm}$ in atomistic MD simulations) can safely be done for Lennard Jones interactions with their fast decay proportional to r_{ij}^{-6}, but leads to severe artifacts in the calculation of the longer-ranged electrostatic interactions. These artifacts can be reduced by the application of switch or shift functions, switching the potential or the forces smoothly to zero either in a buffer region with $r_{\text{buffer}} < r < r_{\text{cutoff}}$ (switch) or over the whole interaction range $0 < r < r_{\text{cutoff}}$ (shift). To avoid artificial separation of opposite charges at the cutoff distance, neutral charge groups can be introduced, such that either all or none of the group charges are included in the summation. A further reduction of the truncation errors can be obtained using a twin-range cutoff, where forces within a first sphere of radius r_1 are computed every integration step, while forces in a second sphere $r_1 < r < r_2$ are only evaluated every n-th integration step (n of the order of 10 to 100), allowing for a larger overall cutoff r_2. Nevertheless, truncating the electrostatic interactions introduces considerable errors in the results.

In the reaction field method [10, 179, 192, 266], the system around each interaction side is separated into an inner region of interest (not necessarily, but ideally a sphere), where the contributions to the Coulomb potential are treated explicitly, and the surrounding medium, that is approximated as a homogeneous bulk with dielectric constant ε and ionic strength I. The full electrostatic potential V at any point is then given by

$$V = V_d + V_{\text{rf}} \quad , \tag{2.14}$$

2 Molecular Dynamics Simulations

where the direct term V_d and the reaction field term $V_{\rm rf}$ are solutions of the Poisson equation in the inner region and the Poisson-Boltzmann equation in the outer region, respectively. The requirements of a continuous potential at the region boundary and of a vanishing potential at infinite distance determine the potential uniquely. The performance of this method depends critically on the quality of the approximation of the surrounding medium as a homogeneous bulk medium.

For simulations performed under periodic boundary conditions (see Section 2.2.5), variants of the Ewald summation technique [68] are widely used to exactly evaluate the Coulomb interactions. For these periodic systems, the sum of the electrostatic interactions has to be extended over all image cells yielding

$$V_{\rm Coulomb} = \frac{1}{2}\frac{1}{4\pi\varepsilon_0}\sideset{}{'}\sum_{\vec{n}}\sum_{i=1}^{N}\sum_{j=1}^{N}\frac{q_i q_j}{|\vec{r}_{ij}+\vec{n}|} \quad . \tag{2.15}$$

$\vec{n} = (n_x L_x, n_y L_y, n_z L_z)$, $\{n_x, n_y, n_z\} \in \mathbb{Z}$, is the vector of translation between the original box (with dimensions L_x, L_y, and L_z) and its periodic images. The prime indicates that for the simulation cell with $|\vec{n}| = 0$ the interaction term $i = j$ is excluded from the summation. The sum in Eq. (2.15) is only conditionally convergent, decaying very slowly for large distances $|\vec{r}_{ij}|$. The trick of the Ewald summation technique is to add a Gaussian charge distribution that neutralizes the original point charge distribution, and to subtract this same Gaussian charge distribution again at the same time. In this way, the total sum can be divided into two independent series. The series involving the original charges and their neutralizing Gaussian counterpart rapidly converges in real space, while the series over the additional pure Gaussian charge distribution contains long-range interactions, but is a smoothly varying periodic function and therefore converges in the reciprocal space. Evaluating these two terms separately using a cutoff both in real and reciprocal space yields accurate results for the electrostatic interactions. A disadvantage of this method is an enhancement of the artificial periodicity introduced into the simulations by the use of periodic boundary conditions (see Section 2.2.5). The Ewald summation itself is a slow procedure scaling with at least $N^{3/2}$ [201], but fast variants like the Particle Mesh Ewald (PME) algorithm [50], for which the required number of computations is reduced to $N \log N$, give accurate results in a reasonable amount of time.

2.2.3 Temperature and Pressure Coupling

In conventional MD simulations, solving Newton's equations of motion for many-body systems within a confined and fixed simulation box, the energy and the volume are conserved and the states of a microscopic ensemble are sampled. On the other hand, experiments are mostly conducted at constant pressure and temperature, i. e., within a canonical ensemble. As thermodynamic averages obtained in the different ensembles match only in the limit of infinite system sizes, for a comparison of experimental and simulation results it is desirable to simulate at constant pressure and temperature. In this way, also a practical problem of constant energy MD simulations could be solved: even in equilibrium, truncation of long-range interactions and numerical inaccuracies result in a slow drift of the temperature (and thereby also the energy) away from its starting value.

Different methods have been suggested to maintain a constant temperature and pressure during simulations. They can be grouped into constraint, stochastic, weak-coupling, and extended system dynamics algorithms [282]. Throughout this thesis, the Berendsen algorithm [16], mimicking a weak coupling to an external heat and pressure bath, has been used and will therefore be presented here in more detail following the description given by van Gunsteren and Berendsen [282].

In the Berendsen scheme [16], deviations of the instantaneous system temperature T from the reference temperature T_0 are corrected according to

$$\frac{dT}{dt} = \frac{T_0 - T}{\tau_T} \quad , \tag{2.16}$$

where t is the time and τ_T is the time constant for the exponential relaxation of the system temperature towards the reference temperature. The temperature adjustment is accomplished by scaling the velocity of all particles at each time step by a factor λ: $\vec{v}_i \rightarrow \lambda \vec{v}_i$. This scaling results in a kinetic energy change

$$\begin{aligned} \Delta E_{\text{kin}} &= \sum_i \frac{1}{2} m \left(\lambda \vec{v}_i \right)^2 - \sum_i \frac{1}{2} m \vec{v}_i^2 \\ &= (\lambda^2 - 1) \frac{1}{2} N_{\text{df}} k_B T \quad , \end{aligned} \tag{2.17}$$

where N_{df} is the number of degrees of freedom and k_B denotes the Boltzmann constant. In Eq. (2.17), the equipartition theorem, $E_{\text{kin}} = \sum_i \frac{1}{2} m \vec{v}_i^2 = \frac{1}{2} N_{\text{df}} k_B T$, has been used. The kinetic energy change is linked to a temperature change via the heat capacity C of the system by

$$\Delta T = \frac{\Delta E_{\text{kin}}}{C} \quad . \tag{2.18}$$

From the desired temperature adjustment per time step Δt (Eq. (2.16)), and using Eqs. 2.17 and 2.18, the scaling factor λ can be derived to be

$$\lambda = \sqrt{1 + \frac{2\,C}{N_{\text{df}}\,k_B} \frac{\Delta t}{\tau_T} \left(\frac{T_0 - T}{T} \right)} \quad . \tag{2.19}$$

The magnitude of the temperature correction can be adjusted by the choice of the time constant τ_T. In the limit of $\tau_T \rightarrow \infty$, microcanonical simulations are recovered. In the opposite limit of $\tau_T = \Delta t$, the temperature is constrained to its equilibrium value at each time step and no temperature fluctuations are allowed. For intermediate values of τ_T the generated ensemble cannot be characterized neither as a canonical nor as a microcanonical ensemble.

The total pressure in a microscopic system is given by the pressure tensor

$$\mathbf{p}_{\text{total}} = \frac{1}{V} \left(2\mathbf{E}_{\text{kin}} - \mathbf{\Xi} \right) \quad , \tag{2.20}$$

where $\mathbf{E}_{\text{kin}} = \frac{1}{2}\sum_i m_i \vec{v}_i \otimes \vec{v}_i$ is the kinetic energy tensor and $\boldsymbol{\Xi} = \sum_{i<j} \vec{r}_{ij} \otimes \vec{F}_{ij}$ is the virial tensor (compare to Section 1.1.2). Using these quantities, a pressure coupling can be achieved in the same way as for the above described temperature coupling according to

$$\frac{d\mathbf{P}}{dt} = \frac{\mathbf{P}_0 - \mathbf{P}}{\tau_P} \quad . \tag{2.21}$$

Instead of the velocities, the coordinates of the particles and the box volume are scaled at each time step in order to relax the system to the reference pressure. In case of an anisotropic system, the scaling factor itself becomes a tensor.

2.2.4 Constraints

A crucial factor in the speed of MD simulations is the magnitude of the time step: the larger the time step, the faster the simulation proceeds. The maximum time step that can be used is determined by the fastest motions in the system. In atomistic simulations, these motions are high frequency length fluctuations of covalent bonds and angular vibrations. As these high frequency oscillations are of essential quantum character, they cannot be correctly described by classical harmonic oscillators (compare Section 2.2.1) and correction terms to the energy would have to be introduced. Instead, these fluctuations can be removed from the simulations by constraining all bond lengths between covalently bound atoms to their equilibrium distance. This is possible, as the bond length fluctuations are in general decoupled from larger motions and are of minor interest for the evolution of the system; and it is justified by the fact that a high-frequency ($h\nu > k_B T$) quantum harmonic oscillator always remains in its ground state. Constraining angle vibrations in this way is however not possible, as this can affect the molecular motion [282].

Fixed bond lengths between different atoms can be imposed on a system as holonomic constraints. Using the method of Lagrange multipliers, this gives a system of $3N + m$ equations, where N is the number of particles in the simulation system and m is the number of constraints. For the case of small molecules and especially water, Miyamoto et al. derived and implemented an analytical solution to this set of equations based on geometrical considerations (SETTLE). For larger molecules, an analytical solution becomes very time-consuming and numerical solutions are preferred. The two most popular algorithms, SHAKE [227] and LINCS [106], first solve the unconstrained equations of motions, and afterwards reset the atomic coordinates such that the constraint equations are fulfilled. In SHAKE, this resetting is done iteratively, while LINCS uses a two-step matrix formalism.

2.2.5 Periodic Boundary Conditions

Due to the limitations of the currently available computing power, atomistic MD simulations are restricted to systems of about 10^6 atoms and to time scales of some hundred nanoseconds. Compared to their volume, these systems have a large surface area; thus the simulation outcome is dominated by edge effects resulting from the boundaries of

the system. Contrarily, most experiments are performed on large, macroscopic samples, where boundary effects have only a minor and localized influence. To minimize edge effects in simulations, most MD studies today are performed applying periodic boundary conditions, realized by simulating infinitely many translated, neighboring copies of a space-filling simulation box in all three spatial directions (see Fig. 2.3). Space-filling box types are for example a triclinic box, a rectangular box, a truncated octahedron, a hexagonal prism, or a rhombic dodecahedron. Within this approach, an artificial periodicity
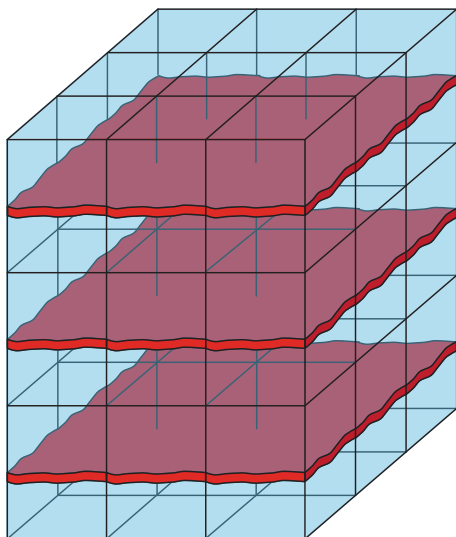
Figure 2.3: Schematic drawing of a simulation setup applying periodic boundary conditions. Translated copies of the simulation box are tightly packed in all three spatial dimensions.

is imposed on the system. However, errors resulting from this periodicity diminish with increasing system sizes and they are in general expected to be smaller than effects caused by system boundaries to a vacuum.

For the use of periodic boundary conditions, some restrictions have to be kept in mind. Usually, the minimum image convention is applied, meaning that for the calculation of short-range interactions (e. g., Lennard Jones interactions) between atoms A and B, only the nearest of all periodic images of atom A to atom B should be considered (see Fig. 2.4). Also, single atoms as well as larger molecules like proteins should not be allowed to interact with their own periodic image. For a rectangular box, this implies that the minimum box dimension must exceed the maximum length of the largest simulated molecule plus
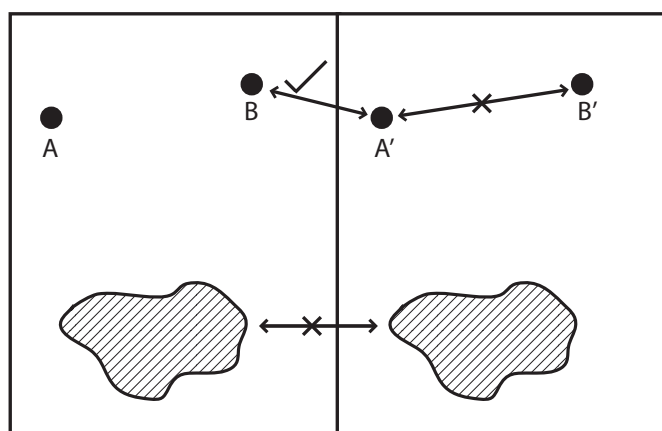
Figure 2.4: Allowed and forbidden short-range interactions in a periodic simulation setup.

twice the cutoff radius for short-range interactions. Long-range interactions that cannot be truncated without introducing severe artifacts are treated using lattice summation algorithms (see Section 2.2.2). To exclude divergent terms in these calculations, overall charge neutrality of the system must be ensured.

Applying periodic boundary conditions in lipid bilayer simulations, multi-lamellar phases are generated. In these layered structures, the amount of water between the periodic images of the bilayer has a critical influence on the bilayer properties (see, e. g., [109]). A sufficiently thick water layer must be ensured to obtain single-bilayer properties from the simulations. This condition is often referred to as 'full hydration of the lipid bilayer' and is generally assumed to be fulfilled by simulating a minimum of about 30 water molecules per lipid molecule.

3 1-Alkanols and Membranes: A Story of Attraction

Beate Griepernau [1] *, Simon Leis* [1] *, Matthias F. Schneider* [2] *, Martin Sikor* [2] *, Daniel Steppich* [2] *, and Rainer A. Böckmann* [1]

Although 1-alkanols have long been known to act as penetration enhancers and anesthetics, the mode of operation is not yet understood. In this study, long-time molecular dynamics simulations have been performed to investigate the effect of 1-alkanols of various carbon chain lengths onto the structure and dynamics of dimyristoylphosphatidylcholine bilayers. The simulations were complemented by microcalorimetry, continuous bleaching and film balance experiments. In the simulations, all investigated 1-alkanols assembled inside the lipid bilayer within tens of nanoseconds. Their hydroxyl groups bound preferentially to the lipid carbonyl group and the hydrocarbon chains stretched into the hydrophobic core of the bilayer. Both, molecular dynamics simulations and experiments showed that all 1-alkanols drastically affected the bilayer properties. Insertion of long-chain 1-alkanols decreased the area per lipid while increasing the thickness of the bilayer and the order of the lipids. The bilayer elasticity was reduced and the diffusive motion of the lipids within the bilayer plane was suppressed. On the other hand, integration of ethanol into the bilayer enlarged the area per lipid. The bilayer became softer and lipid diffusion was enhanced.

[1]Theoretical and Computational Membrane Biology, Center for Bioinformatics Saar, Saarland University, PO Box 15 11 50, 66041 Saarbrücken, Germany

[2]Department of Physics, Augsburg University, Universitätsstr. 1, 86159 Augsburg, Germany

3.1 Introduction

Since the demonstration of the phenomenon of anesthesia in the middle of the $19\mathrm{th}$ century by William Morton, there has been a keen research interest to elucidate the underlying mechanism. Special interest arises from the fact that there is a vast number of structurally and chemically different molecules — amongst them the 1-alkanols — which all cause anesthesia (see review [275]). To account for this variety of anesthetics, the hypothesis of a nonspecific or physical mode of action of anesthesia, mediated by lipid bilayers, rather than a chemical reaction mechanism with binding of anesthetics to membrane proteins was proposed (see, e. g., [135, 222, 274]). This hypothesis is supported by the fact, that the Meyer-Overton rule, after which the anesthetic effect of a drug correlates with its lipophilicity, is the only relation which was found to be valid for almost all general anesthetics [275].

Many different theories explaining the mode of action of anesthetics were suggested and investigated. Indirect, lipid-mediated theories proposed anesthetic action to be exerted by a change of membrane properties upon insertion of anesthetics — like the volume of the membrane [222] or the volume that anesthetics occupy within a membrane [175], the phase transition temperature [101], the lipid chain order, the thickness of the membrane, the lateral phase separations in membranes [271], or the lateral pressure profile [33]. The latter changes may influence the function of proteins embedded in the membrane, e. g., induce a shift of the conformational equilibrium between the closed and the open state of membrane channels [33, 271]. A similar mechanism of protein function regulation by bilayer elasticity was also suggested (for a review, see [147]). However, up to now there is no consensus neither about the site of action of anesthetics nor about the mechanism of their action.

Apart from anesthesia, an important application of aliphatic alkanols is their use as penetration enhancer in transdermal drug delivery [297]. Like in the case of anesthetics, neither the mechanism of action of penetration enhancers nor the exact site of action is known yet [297]. An interesting parallel between the potency of 1-alkanols as anesthetics and as penetration enhancer can be found for the so-called cutoff-effect for anesthetics: the potency of a homologous series of anesthetics — e. g., the 1-alkanols — is increasing until a certain chain length is reached. 1-Alkanols with a chain length above the cutoff length show no anesthetic potency anymore. Similarly, the permeation enhancing effect of 1-alkanols increases with increasing chain length up to decanol and decreases again for 1-alkanols with longer carbon chains [6]. Also, the potency of alcohols as anesthetics as well as penetration enhancers was found to decrease with branching of the carbon chain [135, 297]. For monounsaturated 1-alkenols the cutoff in potency for anesthesia was found to be shifted to longer carbon chains [206]; the same effect can be found for 1-alkenols as penetration enhancer [297]. Apart from the general interest in the mechanisms of anesthesia and penetration enhancement caused by alcohols, an understanding of these effects would possibly allow an improved design of anesthetizing and permeation enhancing drugs.

Up to now there have been only a few computational studies targeting the influence of anesthetics or alcohols on lipids. A recent study by Patra et al. [196] examined the influence of methanol and ethanol onto dipalmitoylphosphatidylcholine (DPPC) and palmitoyloleoylphosphatidylcholine (POPC) lipid bilayers by molecular dynamics (MD) simu-

lations, reporting a decreased order for lipids bound to ethanol and an increased fluidity of the bilayers upon insertion of ethanol. In two successive studies, Chanda and Bandyopadhyay [41, 42] studied the influence of ethanol onto dimyristoylphosphatidylcholine (DMPC) bilayers at moderate and high concentrations. Despite a short simulation time of 5 ns and pre-insertion of ethanol molecules into the bilayer according to experimental results, a change in the distribution of lipid headgroup dipoles and an increase of the in-plane and out-of-plane mobility of the lipids could be observed. The mobility of interfacial water was raised due to preferential hydrogen bonding of ethanol to the lipids. In a combined experimental and theoretical study of POPC bilayers with ethanol at low hydration, Feller et al. [71] found an interaction between the ethanol molecules and the lipid phosphate groups via formation of hydrogen bonds and a predominant localization of the ethanol molecules at the bilayer/water interface. Kranenburg et al. and Venturoli et al. [133, 134, 290] applied coarse-grained simulations to investigate the influence of alcohols on the phase diagrams and especially on the interdigitated phase of lipid bilayers. Concerning anesthetics, the influence of halothane on a pure DPPC bilayer [273] and on a simple transmembrane channel (gramicidin A) [146, 257] has been studied by means of MD simulations. Halothane molecules preferentially resided at the channel-lipid-water interphase. At physiologically relevant concentrations, only minimal effects on the gramicidin A structure, but profound changes in the channel dynamics were reported.

Here, we use MD simulations to investigate the effects of 1-alkanols of different chain lengths (below and above the cutoff length) on the structure and dynamics of lipid bilayers. Although lacking physiological components as, e. g., integral membrane proteins, phospholipid bilayers can be considered as a first approximation to understand the behavior of cell membranes [196]. Applying the technique of MD simulations allows to monitor the insertion of the 1-alkanols into the bilayer as well as modifications of the bilayer properties induced by the 1-alkanols in atomic detail. Special emphasis has been put on the analysis of the bilayer elasticity, volume changes of the bilayer, as well as the lipid ordering before and after addition of 1-alkanols, as these effects have been proposed to be central to the mechanism of action of anesthesia. The simulation results were endorsed by continuous bleaching, film balance and microcalorimetry experiments.

3.2 Materials and Methods

3.2.1 Molecular Dynamics Simulations

Simulation Setup

MD-simulations have been carried out using the GROMACS software package version 3.3 [18, 143, 278]. For the starting structure, a hydrated DMPC bilayer consisting of 128 lipids (kindly provided by Peter Tieleman) was used. This bilayer was placed into solutions of different alkanols — ethanol, octanol, decanol and tetradecanol — with water. The initial coordinates of the 1-alkanols were created with the help of the Dundee PRO-DRG2 Server [231] and then the 1-alkanols were randomly added to the water phase. The concentrations of the water-alkanol solutions were in the range of 0.0 to approximately

$0.6 \, \text{mol kg}^{-1}$ (0, 8, 24, and 72 1-alkanols). Suggested values for full hydration of lipid bilayers range from 20 to 32 water molecules per lipid [109, 142, 195]. To ensure full hydration, we chose a minimum total number of $5,000$ water molecules for the systems with 128 lipids, corresponding to a minimum ratio of 39 water molecules per lipid (compare Table 3.1). Additionally, for octanol and ethanol, systems at larger 1-alkanol concentrations of about 0.9 to $1.3 \, \text{mol kg}^{-1}$ were studied. Starting structures for systems with larger 1-alkanol concentrations were taken from systems at lower concentrations. The effect of ions (system E8) was analyzed by randomly adding sodium and chloride ions at a concentration of $215 \, \text{mM}$ to the water-phase of an equilibrated ethanol-DMPC-water system (E3 after $100 \, \text{ns}$, compare Table 3.1). Each system was simulated for $100 \, \text{ns}$.

To deduce the bilayer elasticity from the bilayer undulations (see below), larger patches were necessary. For this reason, we quadruplicated six equilibrated systems with different 1-alkanol solutions and simulated them for $30 - 50 \, \text{ns}$. In order to estimate the influence of the system size, three systems were increased sixteenfold (2048 lipids, simulation time $\geq 23 \, \text{ns}$). A summary of the simulation systems and times is given in Table 3.1.

All systems were simulated using periodic boundary conditions, a rectangular simulation box, and a constant number of atoms at fixed pressure and temperature (NPT ensemble). Constraining the bond lengths by the LINCS [106] and SETTLE [169] methods allowed for an integration step size of $2 \, \text{fs}$. The lipids and the water-alkanol solutions were separately coupled to a heat bath at $310 \, \text{K}$ using a coupling time constant of $0.1 \, \text{ps}$ [16]. The pressure was kept constant at $1 \, \text{bar}$ by a weak semi-isotropic coupling to a pressure bath [16] using a time constant of $1 \, \text{ps}$ and a compressibility of $4.5 \times 10^{-5} \, \text{bar}^{-1}$.

To ensure a correct treatment of the long-range electrostatic interactions, the Particle Mesh Ewald method [50] was applied using a Fourier grid spacing of $0.12 \, \text{nm}$, a 4th-order cubic interpolation and a relative accuracy of 1.0×10^{-5}. The short-range van der Waals interactions have been accounted for with a cutoff-scheme using a cutoff radius of $1 \, \text{nm}$. The neighborlist was updated every 10th integration step.

The force field for the lipids was taken from Berger et al. [20]. For water, the SPC model [17] was chosen. For the 1-alkanols, the GROMACS force field, modified for the partial atomic charges according to MacCallum and Tieleman [151], was adopted. A system with ethanol was additionally simulated using the recently developed GROMOS 53A6 force field [193]. The main difference between the two force fields used for the simulations of ethanol is an increased polarity of the hydroxyl group for the GROMOS 53A6 force field.

Membrane Thickness

The average headgroup-to-headgroup thickness d_{HH} of the bilayer was calculated by determining the center of mass coordinates of each lipid headgroup at each time step. These headgroup coordinates — weighted by a normalized Gaussian function — were assigned to a grid in the x–y–plane (lateral membrane plane) for each monolayer separately. The membrane thickness was taken as the space and time average of the distance between opposite grid points.

system name	number of lipids	number and type of 1-alkanol molecules	number of water molecules	simulation time (ns)
C1	128	none	5,673	100
C2	512	none	22,692	52
C3	2048	none	90,768	23
E1	128	8 Ethanol	7,470	100
E2	128	24 Ethanol	7,409	100
E3	128	72 Ethanol	9,394	100
E4	128	128 Ethanol	6,995	100
E5	512	288 Ethanol	26,800	31
E6	2048	1152 Ethanol	107,200	23
E7	128	72 Ethanol	6,146	100
E8	128	72 Ethanol	9,322	100
O1	128	8 Octanol	5,237	100
O2	128	24 Octanol	5,140	100
O3	128	72 Octanol	6,656	100
O4	128	128 Octanol	7,945	100
O5	128	185 Octanol	7,955	100
O6	512	96 Octanol	20,560	40
O7	512	288 Octanol	26,624	33
O8	2048	1152 Octanol	106,496	26
D1	128	8 Decanol	5,229	100
D2	128	24 Decanol	5,092	100
D3	128	72 Decanol	7,474	100
D4	512	288 Decanol	29,896	31
TD1	128	8 Tetradecanol	5,212	100
TD2	128	24 Tetradecanol	5,027	100
TD3	128	72 Tetradecanol	7,307	100
TD4	512	288 Tetradecanol	29,228	31

Table 3.1: The systems studied in the simulations. For the simulation E7, the GRO-MOS 53A6 [193] force field was used instead of the GROMACS force field. The simulation E8 contained ions in the aqueous phase.

Deuterium Order Parameter

The average fluctuations of the lipid and 1-alkanol chains around the bilayer normal are characterized by the order parameter tensor

$$S_{\alpha\beta} = \left\langle \frac{3}{2}\cos\theta_\alpha \cos\theta_\beta - \frac{1}{2}\delta_{\alpha\beta} \right\rangle \qquad (\alpha, \beta = x, y, z) \quad , \tag{3.1}$$

where $\cos\theta_\alpha$ denotes the angle between the αth molecular axis and the bilayer normal. The deuterium order parameter S_{CD} can be derived from the order parameter tensor by using the equation

$$S_{\mathrm{CD}} = -\frac{2}{3}S_{xx} - \frac{1}{3}S_{yy} \quad . \tag{3.2}$$

Here, the deuterium order parameters were calculated for the carbon atoms of the DMPC lipids as well as for the carbon atoms of the 1-alkanol molecules themselves. Both lipid chains were considered separately. The order parameters were averaged over time, starting at the respective equilibration time (Table 3.2).

Area per Lipid

Although there are various sophisticated methods to calculate the area per lipid in binary mixtures [62], we chose the conventional approach to divide the total area of the simulation box by the number of lipids in one monolayer and to neglect the area of the 1-alkanol molecules. In this way, the simulated results can be most easily compared to experiments. The fact that the area per 1-alkanol molecule is much smaller than the area per lipid further substantiates this procedure.

Calculation of the Bilayer Elasticity from Undulations

The elasticity of the bilayer has been derived from its undulations by performing a spectral analysis analogous to the procedure described by Lindahl and Edholm [141]. Similar methods have been applied by Goetz et al. [84], Marrink and Mark [158], and den Otter and Briels [57].
For modes with wavelengths larger than the membrane thickness, protrusions can be neglected and the bilayer can be approximated as a single surface. In Fourier space, the potential energy E_{und} of the surface undulations divided by the total area A of the bilayer can be expressed as a function of the spectral intensity $I(|\vec{k}|)$ (see, e. g., Safran [228])

$$\frac{E_{\mathrm{und}}(|\vec{k}|)}{A} = 0.5 \left(k_c |\vec{k}|^4 + \gamma |\vec{k}|^2 \right) I(|\vec{k}|) \tag{3.3}$$

with the wave vector $\vec{k}$, the bending modulus k_c and the surface tension γ. Using the equipartition theorem $E = \frac{1}{2}k_B T$ with the Boltzmann constant k_B and the temperature

T, a transformation of equation (3.3) yields the following relation between the spectral intensity and the bending modulus:

$$I(|\vec{k}|) = \frac{k_B T}{A} \left(k_c |\vec{k}|^4 + \gamma |\vec{k}|^2 \right)^{-1} \quad . \tag{3.4}$$

For the semi-isotropic pressure coupling applied in the simulations, the surface tension is approximately zero. The bending modulus can then be obtained from a fit of the spectral intensity as a function of the wave number.

The spectral intensity was computed by fitting a grid with a spacing of $g \approx 0.2\,\mathrm{nm}$ to the plane of the bilayer (x–y plane). For each grid point (x_i, y_j), the amplitude of the grid point normal to the bilayer plane $z(x_i, y_j, t)$ as a function of time was calculated by summing over the center of mass z-coordinates $z_l(t)$ of the lipid headgroups weighted by a coordinate-dependent Gaussian function:

$$z(x_i, y_j, t) = \frac{1}{2} \sum_m \frac{\sum_l z_l(t) \, \exp \left(\frac{-(x_l(t)-x_i)^2-(y_l(t)-y_j)^2}{2\sigma^2} \right)}{\sum_l \exp \left(\frac{-(x_l(t)-x_i)^2-(y_l(t)-y_j)^2}{2\sigma^2} \right)} \quad . \tag{3.5}$$

The sum $\sum_m$ adds up the contributions of the two monolayers and the sum $\sum_l$ is taken over all lipids of one monolayer. The elasticity has been computed both for the average of the two monolayers as well as for the monolayers separately. To ensure correct weighting of the contributions of all surrounding lipids to the amplitude of the undulations at a certain grid point, the width σ of the Gaussian function was chosen proportional to the grid spacing: $\sigma = 0.8\,g$. Thereby, all lipid headgroup coordinates can be attributed with a non-negligible contribution to specific grid points, while only a small smoothing between neighboured grid points is applied. A two-dimensional Fast Fourier Transformation (FFT) was applied to the function $z(x_i, y_j, t)$ yielding $\tilde{z}(k_x, k_y, t)$. Projection of the two spatial directions onto the absolute value of the wave vector $\vec{k}$ gave the k-space mode amplitudes $\tilde{z}(|\vec{k}|, t)$, the square of which is the spectral intensity $I(|\vec{k}|, t)$. A binning over the intensities for different wave numbers in intervals of $\frac{2\pi}{l_{\mathrm{box}}}$ was applied, where l_{box} is the length of the simulation box in x- and y-direction.

As mentioned above, such an analysis can only be conducted for modes with wavelengths larger than the bilayer thickness (see Fig. 3.6). Therefore, only the 4-fold bilayers consisting of 512 lipids ($\approx 12.8\,\mathrm{nm}$ box length in x- and y-direction) and the 16-fold systems (2048 lipids) (see Table 3.1) have been evaluated.

Additionally, the same analysis has been performed, but with a FFT in all three dimensions to resolve the intensity not only as a function of the wave number, but also the frequency. The total spectral intensity $I(|\vec{k}|)$ is then given by the sum over all frequencies except $\omega = 0$ (exclusion of $\omega = 0$ eliminates the translation of the bilayer).

Diffusion Coefficient

The lateral self-diffusion coefficient D of the lipids

$$D = \frac{1}{4} \lim_{t \to \infty} \left(\frac{1}{t} \left\langle |x(t_0) - x(t_0 + t)|^2 \right\rangle_{t_0} \right) \tag{3.6}$$

was estimated from the slope of the mean-square displacements d^2 of the center of mass coordinates x of the lipid headgroups in the bilayer plane (linear fit in the time interval from the 2nd to the 5th nanosecond):

$$d^2(t) = \frac{1}{N}\frac{1}{T-t}\sum_{i=1}^{N}\sum_{t_0=0}^{T-t-1}|x(t_0)-x(t_0+t)|^2 \quad .$$

(3.7)

The first sum runs over all N lipids and the second sum runs over all time frames smaller than $T-t$, where T is the sampling time (sliding window). The lateral mean-square displacements of the lipids were corrected for the center of mass motion of the respective monolayer [24]. The error was estimated by splitting the trajectories with 512 lipids into pieces of $10\,\mathrm{ns}$ length, and those with 128 lipids into pieces of $40\,\mathrm{ns}$ length.

3.2.2 Experiments

Diffusion Measurements and Continuous Bleaching

DMPC was purchased from Avanti Polar Lipids (Alabaster, AL, USA) and used without further purification. The fluorescent lipid probe TexasRed DHPE was purchased from Invitrogen (Karlsruhe, Germany). Branched polyethylenimine (PEI) (M.W. $1800\,\mathrm{g}\ \mathrm{mol}^{-1}$), potassium nitrate, ethanol (p.a.) and tetradecanol (purity 97%) were obtained from Sigma Aldrich (Munich, Germany).

Supported lipid bilayers on a cushion of PEI were recently shown to display quasi-free behavior [237] and thus were selected to study the lateral diffusion of the alkanol doped membranes. Multilamellar vesicles (MLVs) were prepared by hydration of a dried lipid film with $150\,\mathrm{mM}$ KNO_3/H_2O and subsequent incubation at $T > T_\mathrm{m}$ for several hours. Small unilamellar vesicles (SUVs) were obtained by sonication of MLVs with a probe sonicator for 15 minutes. Finally, the SUVs were centrifuged to remove titanium particles.

Solid supported bilayers for diffusion measurements were prepared by vesicle fusion on a microscope coverslip. The SUV solution with a concentration of $0.5\,\mathrm{mg}\ \mathrm{ml}^{-1}$ and a $0.2\,\%$ TexasRed DHPE content was incubated on the cover glass at $T > T_m$ for 6 hours, followed by extensive washing with buffer to remove the remaining SUVs. To obtain polymer-cushioned bilayers, a $10\,\mathrm{mg}\ \mathrm{ml}^{-1}$ PEI solution in $150\,\mathrm{mM}$ KNO_3/H_2O was added to the system and left to incubate for 15 minutes.

The diffusion measurements were performed on an Axiovert 200 Fluorescent Microscope (Zeiss, Göttingen, Germany) using the method of continuous photobleaching [59]. Briefly, a spot of approximately ten micrometers diameter (Area of Interest, AoI) was observed with a 63x oil immersion objective. The fluorophores inside the spot are continuously photobleached while new unbleached lipids diffuse into the AoI. For the radial intensity distribution near the edge of the AoI the following analytical expression holds [59]:

$$I(r) \propto \exp\left(\lambda r\right) \qquad \text{with} \quad \lambda^2 = \frac{B_0}{D} \quad .$$

(3.8)

In this equation, D is the diffusion constant of the fluorophore and B_0 is the bleaching rate. B_0 is determined from the exponential decay of the intensity in the center of the AoI,

$$I\left(t\right) \propto \exp\left(-B_0 t\right).$$ (3.9)

The results are given as the mean of three measurements performed within hours on a freshly prepared sample, with the standard deviation giving the error bars.

Incorporation of 1-Alkanols into the Membrane

Ethanol was directly added to the aqueous phase and is therefore given in vol%. Tetradecanol, however, is not water soluble and was therefore dissolved in chloroform and added to the chloroform/DMPC solution prior to vesicle or film preparation. Partition coefficients of tetradecanol are therefore missing.

Film Balance Experiments

To acquire the compressibility of lipid membranes with and without 1-alkanols, pressure-area-isotherms were measured using a regular film balance of Nima Technologies (Coventry, England). $500\,\mathrm{ml}$ of double distilled water was filled into a trough and the lipid-chloroform solution was spread onto the water surface. Due to the low solubility of tetradecanol in water, tetradecanol and DMPC molecules were mixed together in a ratio of 1 to 10 in a chloroform solution, while $2\,\mathrm{vol\%}$ of ethanol were directly added into the water subphase. After evaporation of the solvent the film was compressed with a speed of $3\,\mathrm{cm^2\ min^{-1}}$ ($1.3\,\mathrm{\mathring{A}^2}$/minute per molecule). The lateral pressure was monitored using a Wilhelmy plate. The isothermal compressibility κ_T was directly derived using

$$\kappa_T = \left.\frac{1}{A}\frac{dA}{d\pi}\right|_T.$$ (3.10)

From the compressibility profile we extracted κ_T of the liquid expanded phase (corresponding approximately to the fluid phase in lipid bilayers) by fitting two tangents at the lower left of the transition peak shoulder (compare Fig. 3.9). The intersection was taken as the onset of the fluid phase. From the same fit the error bar was calculated.

Microcalorimetry

Multilamellar Vesicles (MLVs) of DMPC were produced both in double distilled water and in a double distilled water/ethanol (9:1 v/v) solution. For DMPC/tetradecanol MLVs (20:1 mol/mol), the components dissolved in chloroform were mixed and after evaporation of the solvent hydrated in double distilled water. Differential heat capacity scans of the lipid dispersions ($0.5\,\mathrm{mg\ ml^{-1}}$) were recorded with a Microcal VP-DSC Micro Calorimeter (Microcal Inc., USA) at a heating rate of $5°\,\mathrm{C\ h^{-1}}$ at high feedback mode.

Measured data were analyzed using the routines of the Origin software (Microcal Inc., USA). The solubility of the 1-alkanols in the phospholipid membranes can directly be derived from the heat capacity experiment exploiting the shift in the phase transition temperature [8]

$$\Delta T \;=\; \frac{RT^2}{H}x_M \; .$$
(3.11)

R denotes the gas constant, T the transition temperature of the lipid-alkanol-suspension, and x_M the concentration of dissolved 1-alkanol in the membrane fraction in mol. The transition enthalpy H is extracted from the heat capacity by integrating over the transition regime

$$H \;=\; \int c_p \, dT \quad .$$
(3.12)

Hence, the thermodynamic partition coefficient K_p, defined as the ratio of the mole fraction of 1-alkanols in the bilayer and the mole fraction of 1-alkanols in the surrounding water, can be calculated directly from equation (3.11) and the amount of alkanol added to the solution.

3.3 Results and Discussion

3.3.1 Molecular Dynamics Simulations

Equilibration Times

All 1-alkanols went into the bilayer within a few nanoseconds. Only for the simulations with ethanol and the simulations with the highest octanol concentrations (O4 and O5), 1-alkanol molecules remained in the water. Long-chain 1-alkanols clustered prior to their membrane insertion, resulting in increased equilibration times. To determine the equilibration times, the concentration of the 1-alkanols in the water as well as the area per lipid and the lipid order parameter were monitored as a function of time. The equilibration times for the different simulations with 128 lipids are summarized in Table 3.2. All later analysis is done with respect to these equilibration times.

System	C1	E1	E2	E3	E4	E7	E8	O1	O2
Eq. time (ns)	5	5	16	31	25	20	20	10	25

System	O3	O4	O5	D1	D2	D3	TD1	TD2	TD3
Eq. time (ns)	30	40	30	10	20	60	13	60	50

Table 3.2: Equilibration times for the different simulated systems with 128 lipids. Please note that simulations at higher 1-alkanol concentrations were started from snapshots at lower concentrations.

Given that the building blocks for the large systems with 512 and 2048 lipids, i.e., the smaller patches, were already in equilibrium, the equilibration times for the 4-fold and 16-fold systems were expected to be small. Using the same criteria as before, the large systems were even found to be in equilibrium from the beginning. However, for the calculation of the bending modulus from the bilayer undulations, additionally all undulatory modes have to be fully developed. Therefore, the intensity of each mode, especially the modes with the longest wavelengths, which take the longest time to develop [158], was monitored as a function of time (not shown). Maximum intensity was reached within the first few nanoseconds and an equilibration time of 6 ns for the patches with 512 lipids and 7 ns for the patches with 2048 lipids was chosen accordingly.

Partition Coefficients

In the simulations presented here, the initial molalities of the 1-alkanol-water solutions were chosen in the range of $0.0 \, \text{mol kg}^{-1}$ to $1.3 \, \text{mol kg}^{-1}$ (mole fraction 0.000 to 0.023). After equilibration, in the simulations with 1-alkanols molalities of $0.09 \, \text{mol kg}^{-1}$ to $2.13 \, \text{mol kg}^{-1}$ (mole fractions of 0.06 to 0.59) were obtained within the bilayer, close to or above the 1-alkanol concentrations required to reach anesthesia ($10 \, \text{mM}$ to $100 \, \text{mM}$ [79, 130, 234]). However, the anesthetic effect depends strongly on the anesthetic used, the desired effect, and other factors.

The thermodynamic partition coefficient K_p, defined as the ratio of the mole fraction of 1-alkanols in the bilayer and the mole fraction of 1-alkanols in the surrounding water, could only be calculated for simulations for which the average number of 1-alkanol molecules outside of the bilayer was significantly larger than zero. Otherwise, lower bounds for the partition coefficient (determined by assuming that one alkanol molecule stayed inside the water) are given. The respective values are summarized in Table 3.3. Because for most of the simulations the number of 1-alkanols remaining in the water is very small, the standard deviation determined by block averaging is large.

System	E3	E4	E7	E8
Part. Coeff.	$(1.8 \pm 1.4) \times 10^3$	470 ± 119	76 ± 20	814 ± 331

System	O3	O5	D3	TD3
Part. Coeff.	$*2.4 \times 10^3$	$\left(5.5 \, {}^{+28.1}_{-4.8}\right) \times 10^4$	$*2.7 \times 10^3$	$*2.6 \times 10^3$

Table 3.3: Partition coefficients obtained for the simulations with 128 lipids and large concentrations of 1-alkanols. Values marked by $*$ define lower bounds. For the simulation E3, an equilibration time of $30 \, \text{ns}$ was used.

For decanol and tetradecanol, the lower bounds of K_p obtained here are consistent with measurements of the partition coefficients K (ratio of concentrations) of 1-alkanols into bilayers consisting of a mixture of egg lecithin, cholesterol and phosphatidic acid [79]. Seeman et al. [234] reported a remarkably lower value for the partitioning of decanol into erythrocyte ghost membranes ($K = 1226.31 \pm 92.13$ in units of molal membrane concentration over molar water concentration, i.e., $K_p \approx 4.4 \times 10^4$), but still this value is well above the lower bound for the partition coefficient found here ($K_p > 2.7 \times 10^3$).

Thermodynamic partition coefficients for octanol and various pure bilayers (DPPC, DOPC, DLPE, DOPG, and SAPC) were experimentally determined by Rowe et al. [225] ($K_p \approx 1.7 \times 10^4$, averaged over all different bilayers at $T = 45°$ C) and are in agreement with the lower bound for the octanol partition coefficient of system O3 ($K_p > 2.3 \times 10^3$), and comparable to the thermodynamic partition coefficient of system O5 ($K_p = \left(5.5^{+28.1}_{-4.8}\right) \times 10^4$). In a recent study, using NMR data and gas chromatography, Koenig and Gawrisch [130] found about 4% of the ethanol being bound to the lipids for a solution of ethanol and water at physiological concentration with a fraction of $14\,\mathrm{wt}\%$ lipids. This corresponds to a thermodynamic partition coefficient of $K_p \approx 10$. A value in the same order of magnitude was reported by Rowe [224] and was confirmed by our own experiments (see below). The thermodynamic partition coefficients obtained from the simulations E1 – E4 using the GROMACS force field parameters for ethanol are larger than these experimental values by at least two orders of magnitude. A similarly increased partition coefficient can be deduced from the recent simulations by Patra et al. [196], using the same force field. This discrepancy between experiment and simulations is at least partially due to the force field: usage of the refined GROMOS 53A6 force field [193] for the ethanol molecules (simulation E7) with an increased polarity of the hydroxyl group resulted in a considerably decreased partition coefficient of $K_p = 76 \pm 20$ as compared to the respective system using the GROMACS force field (E3, $K_p \approx (1.8 \pm 1.4) \times 10^3$). Further reasons for the deviating partition coefficient in the simulations could be inaccuracies in the lipid force field or the only implicit consideration of polarization effects in the region of the hydrophilic lipid headgroup. A possible influence of ions (Na^+ and Cl^-) was tested by a simulation at approximately $200\,\mathrm{mM}$ NaCl (GROMACS force field). Though in the simulation with ions a decrease of the partition coefficient by a factor of 2 was observed (simulations E3 and E8), this decrease is too moderate to account for the difference between the experiments and the simulations. Due to the considerably too large partition coefficient for ethanol, the observed effects are probably amplified with respect to experiments at comparable concentrations.

Distribution of 1-Alkanols inside the Bilayer

Initially, all 1-alkanols were randomly placed into the water. The 1-alkanols spontaneously moved into the bilayer on short timescales. Their tendency to cluster inside the water phase — resulting in a slowdown of membrane insertion — increased with the carbon chain length. Once inside the bilayer, the hydroxyl groups of the 1-alkanols were closely anchored to the lipid headgroups and their carbon tails stretched into the hydrophobic core of the bilayer (see Fig. 3.1).

The 1-alkanol integration process is very heterogeneous: head-first and tail-first insertion as well as initial aggregation on the membrane surface was observed for long-chain 1-alkanols. Aggregation of long-chain 1-alkanols on the membrane surface is followed either by a sequential membrane integration of the cluster-alkanols, or by penetration of the complete cluster into the lipid headgroup region. The latter case is illustrated in Fig. 3.2, showing a tetradecanol cluster insertion after several lipids gave way. After insertion, the 1-alkanol carbon chains aligned with the hydrophobic lipid tails and dispersed inside the monolayer (Fig. 3.2 C).
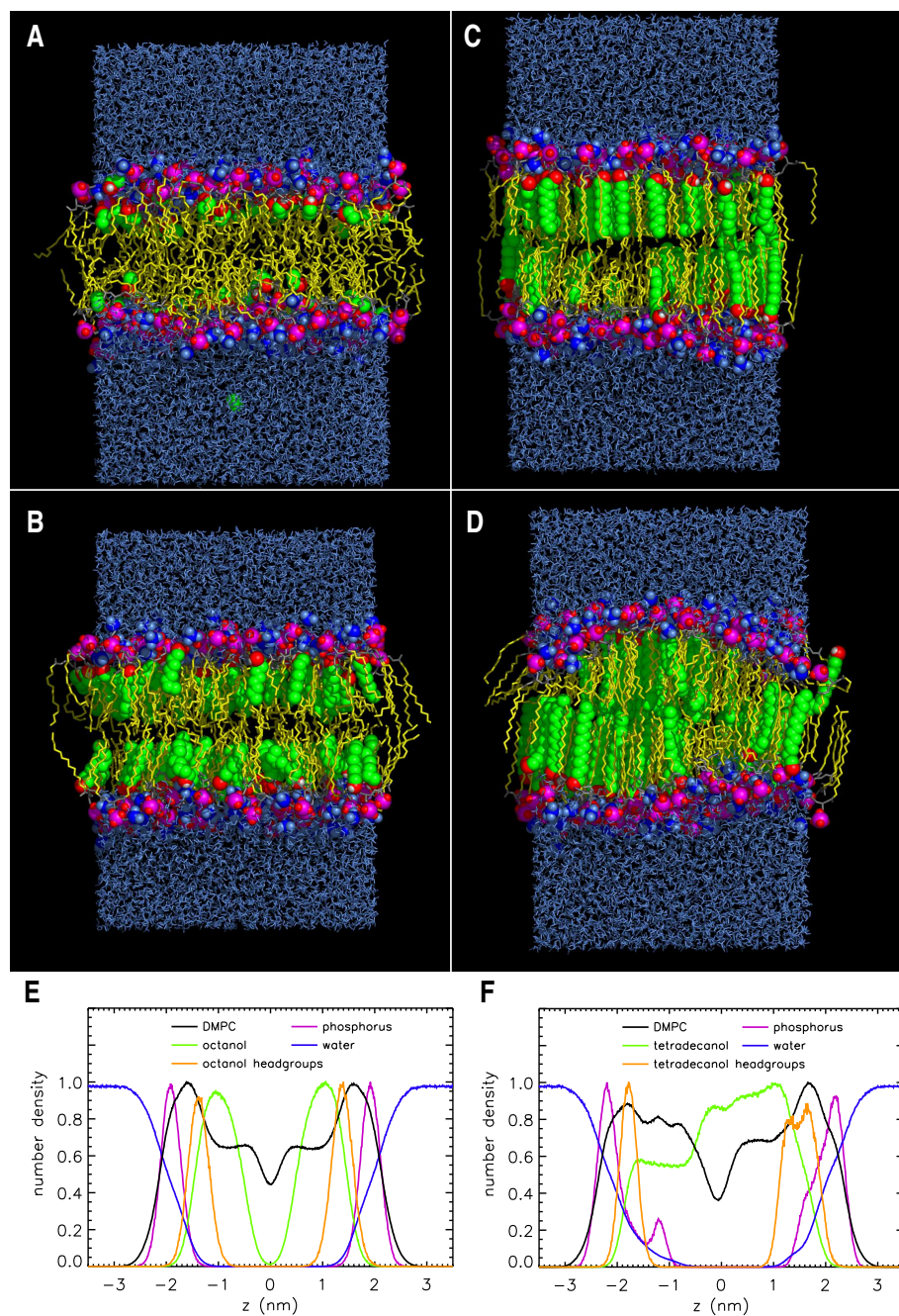
Figure 3.1: Snapshot of some of the simulation systems after 100 ns with ethanol (A), octanol (B), decanol (C), and tetradecanol (D) (128 lipids/72 1-alkanol molecules). The 1-alkanol chains are highlighted in green, their oxygens are represented by red spheres. Water is blue, the lipid chains are yellow, the phosphorus atoms are magenta, and nitrogen atoms are light blue). Additionally, the (number) density profiles across the lipid bilayer (normalized to one) both for the octanol-DMPC system (E) as well as for the tetradecanol-DMPC system (F) are given. The latter exhibits an asymmetric distribution of the tetradecanol molecules between the two monolayers.

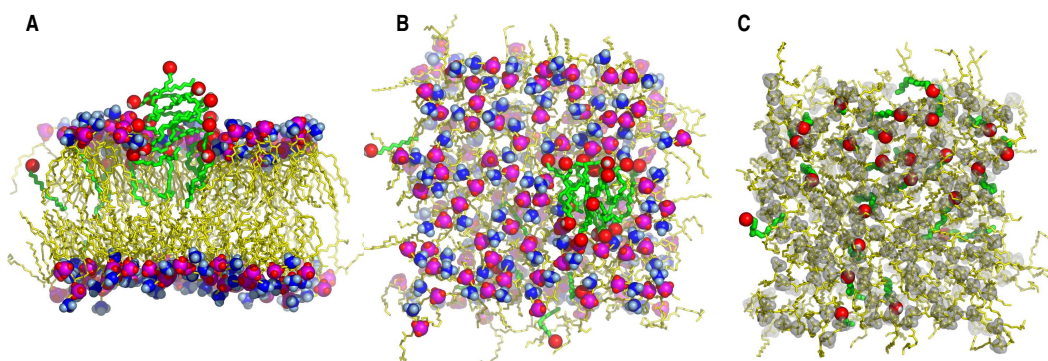Figure 3.2: A cluster of tetradecanol molecules (green: carbon chains, red: oxygen atoms) enters the bilayer. A and B show a side and a top view of a snapshot after 11 ns, C a top view after 100 ns. For clarity, water molecules have been omitted from the representation (in A, four lipids have been removed additionally). After 100 ns, the tetradecanol cluster is dissolved in the lipid bilayer (C).

No crossing events of tetradecanol molecules between the bilayer leaflets were observed. For octanol and decanol only one, and for ethanol many such crossing events were found (see also [196]).

For ethanol and octanol, the partitioning of 1-alkanol molecules between the monolayers was rather uniform (except for the two largest concentrations of octanol). Yet for decanol and tetradecanol, this distribution was asymmetric due to the clustering of the 1-alkanol molecules inside the water prior to membrane insertion.

Without 1-alkanols, a bilayer thickness of $d = 34.6$ Å was determined. This value is in line with results of experimental studies: e. g., Lewis and Engelman [140] reported a bilayer thickness (distance between the maxima in the electron density profile) of $d_{HH} = (34 \pm 1)$Å at $T = 36°$ C studying sonicated unilamellar DMPC liposomes (This value was later corrected by addition of 0.8 to 1Å [177]). Comparable values were found by Nagle et al. [177] and Kucerka et al. [136]. Depending on the concentration, the insertion of the long-chain 1-alkanols octanol, decanol, and tetradecanol *globally* increased the thickness of the bilayer by $0.5 - 6.1$ Å (compare Table 3.4).

# 1-alkanols	Ethanol d_{HH} (Å)	Octanol d_{HH} (Å)	Decanol d_{HH} (Å)	Tetradecanol d_{HH} (Å)
8	34.6 ± 0.2	35.1 ± 0.3	35.1 ± 0.4	35.2 ± 0.2
24	34.6 ± 0.4	36.0 ± 0.3	36.5 ± 0.3	37.3 ± 0.2
72	34.4 ± 0.2	38.2 ± 0.4	40.3 ± 0.2	40.7 ± 0.2
128	33.6 ± 0.2	39.8 ± 0.1	-	-
185	-	40.2 ± 0.1	-	-

Table 3.4: Average headgroup-to-headgroup thickness d_{HH} of the bilayer for the different simulations with 128 lipids. The thickness of the pure bilayer in water was (34.6 ± 0.3) Å. For simulations E2, E3, and TD3, equilibration times of 15, 30, and 15 ns were used.

However, due to the asymmetric integration of tetradecanol, a *local* thinning of the membrane could be observed: lipids of one monolayer were drawn to the other monolayer, such that the tetradecanol chains spanned the whole hydrophobic core of the bilayer (see Fig. 3.1 D). In Fig. 3.1 F, this thinning is reflected by an additional peak in the phosphorus density. The insertion of ethanol decreases the bilayer thickness by up to $1\,\text{Å}$. This is coupled to the well-known intertwining between the lipid fatty acyl chains [242]. In simulations with octanol, decanol, and tetradecanol, the central minimum in the density profile was more pronounced than for a pure DMPC bilayer (not shown).

The hydroxyl groups of inserted 1-alkanols preferentially hydrogen bonded to the lipid glycerol backbone. A hydrogen bond analysis, where a hydrogen bond was said to exist if the donor and acceptor atoms were $\leq 3.5\,\text{Å}$ apart and the angle hydrogen – donor – acceptor was $\leq 30°$, showed that for all simulations with 128 lipids and 72 1-alkanols (GROMACS force field) more than 50 hydrogen bonds between the lipid oxygen atoms and the 1-alkanols' hydroxyl groups existed at every time step. The favorite binding site was the carbonyl oxygen at the end of the sn2-chain (stereochemical numbering), where more than 49% of all hydrogen bonded 1-alkanols docked. For the simulation of ethanol with the GROMOS 53A6 force field, only approximately 33 hydrogen bonds between lipid oxygens and 1-alkanols existed on average per time step. Typical lifetimes of hydrogen bonds, defined as the inverse of the rate constant for hydrogen bond breaking [279], between the 1-alkanols and the carbonyl oxygen of the sn2-chain ranged from $434\,\text{ps}$ for ethanol to $1976\,\text{ps}$ for octanol. Experimental studies reported ethanol-lipid contact times of the same order ($1\,\text{ns}$ [110] up to $1.8\,\text{ns}$ [130]).

Deuterium Order Parameters

For the simulations using the GROMACS force field for the 1-alkanols, the insertion of any 1-alkanol into the lipid bilayer resulted in an increase of the (average) deuterium order parameter of the lipid carbon chains (Fig. 3.3). This order increase was larger for longer 1-alkanol chains and larger concentrations of the 1-alkanols inside the bilayer. The usage of the refined GROMOS 53A6 force field for ethanol slightly decreased the average order of the lipids in the presence of ethanol compared to pure bilayers. These findings are also reflected in a decreased gauche:trans ratio of the lipid tails (see Section *Supplementary Material*).

Addition of ethanol (GROMACS force field) mainly influenced the order of the outer carbon atoms. Relative to the pure bilayer, a steeper order decrease at the core of the bilayer was observed. This effect is probably due to intertwining of the lipids and is in line with the thickness decrease of the bilayer. The octanol, decanol, and tetradecanol molecules stretched further into the bilayer and raised the order of all carbon atoms. For these 1-alkanols, the maximum of the lipid order parameter was shifted towards the bilayer core. Both lipid chains (sn1 and sn2) showed a similar behavior; the values were only shifted by the additional carbon atom at the headgroup of the sn1 chain.

The deuterium order parameters strongly depend not only on the concentration of the solute [204], the temperature [205], and the hydration of the sample [204], but also on the specific lipid investigated as well as on the cholesterol content of the bilayer. Therefore, a comparison between the theoretically derived and experimentally found values requires
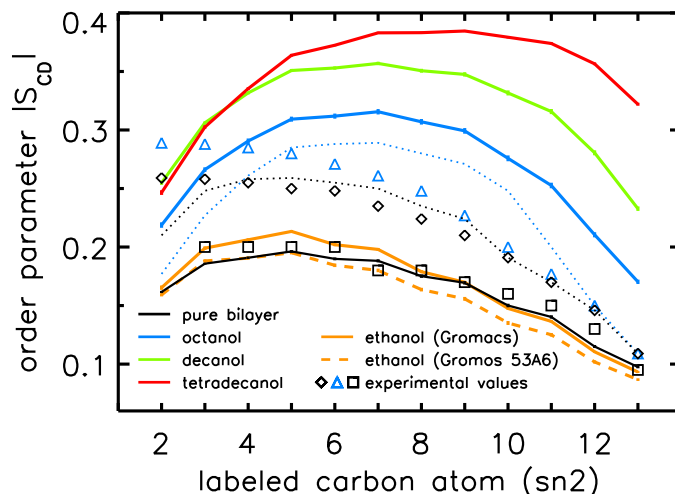
Figure 3.3: Deuterium order parameter of the DMPC lipids as a function of the carbon number, counted from the outside to the inside of the bilayer (128 lipids). Solid lines indicate values obtained from the simulations (sn2 chain, black: pure DMPC, orange: DMPC with 72 ethanol molecules, blue: DMPC with 72 octanol molecules, green: DMPC with 72 decanol molecules, and red: DMPC with 72 tetradecanol molecules). Standard deviations are included by error bars (hardly visible due to their smallness). The orange dashed line shows the lipid order parameters calculated from the simulations of ethanol with the GROMOS 53A6 force field (simulation E7). Symbols denote experimental values from ^{2}H-NMR measurements (black squares: pure DMPC measured by Nevzorov [180]; black diamonds: pure DMPC measured by Pope and Dubro [204]; blue triangles: DMPC with octanol (lipid/solute/water molar ratio of $1.0/0.4/9.0$, $T \approx 34°C$) measured by Pope and Dubro [204]). Rearrangements of the experimental order parameters of Pope and Dubro [204] according to the overall shape of the curve obtained in the MD simulations (see text) are shown as dotted lines (pure DMPC: black; DMPC with octanol: blue).

a careful analysis of the respective conditions. ^{2}H-NMR measurements of the lipid order parameter were done by Pope and Dubro [204] and Nevzorov et al. [180]. Their results are included in Fig. 3.3. While for pure DMPC bilayers the results of Nevzorov et al. [180] agree very well with the simulations, the measurements of Pope and Dubro [204] show an increased lipid order as compared to our simulations. This is probably due to the comparably low hydration (9 water molecules per lipid) and temperature ($T \approx 34°C$) in the experiments. As in the simulations, Pope and Dubro [204] observed a lipid order increase upon addition of octanol. However, the lipids were perdeuterated in various positions simultaneously. Therefore, the measured order parameters could not be assigned unambiguously to the lipid carbon atoms [204]. Based on the results of our simulations, we suggest a rearrangement of the experimental values as indicated by the dotted lines in Fig. 3.3. For this rearrangement, the experimental values have been reassigned to the carbon atoms such that the order parameters as a function of the carbon atom number adopt the same shape as the order parameters determined from the simulations.

The order of the 1-alkanol carbon chains was found to depend on the chain length and the 1-alkanol concentration in the bilayer (Fig. 3.4) in the same way as the lipid order. A

comparison to ^{2}H-NMR experiments qualitatively confirms the simulation results: Pope and Dubro [204] investigated the influence of solute concentration and hydration onto the order of octanol molecules dissolved in DMPC bilayers. As in the simulations, they found an increase in the octanol order as the octanol concentration was raised. An increase in hydration reduced the order of the octanol molecules. Values for tetradecanol and decanol order parameters can be found in publications of Westerman et al. [296] and Thewalt et al. [260], where the order of selectively deuterated 1-decanol molecules was measured using multilamellar dispersions. As can be seen from Fig. 3.4, the order parameters calculated from the simulations are in most cases larger than the experimentally found values. For decanol and tetradecanol, this discrepancy is probably due to the considerably larger temperatures ($T = 323\,\mathrm{K}$ and $T = 330\,\mathrm{K}$) in the experiments.
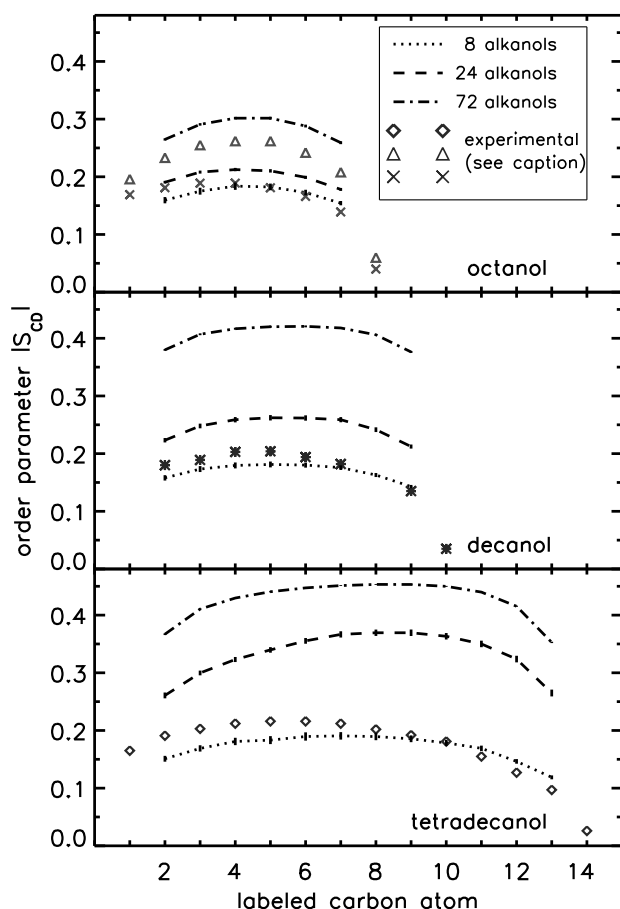
Figure 3.4: Deuterium order parameter of the 1-alkanols' carbon chains as a function of the carbon number, counted starting at the hydroxyl group. The dotted/dashed/dash-dotted lines correspond to the simulations with 8/24/72 1-alkanols in 128 lipids. Experimental values are taken from Pope and Dubro [204] (crosses), Pope et al. [205] (triangles), Thewalt et al. [260] (asterisks), and Westerman et al. [296] (diamonds).

Area per Lipid

For the pure DMPC bilayer in water, the average area per lipid was $64.15 \pm 0.77\,\text{Å}^2$, in agreement with experimental results ranging from $60.01 \pm 0.75\,\text{Å}^2$ [9] to $65.7 \pm 3.0\,\text{Å}^2$ [140] at $309\,\mathrm{K}$ and with previous simulation studies applying the same force field (e. g., [92, 109, 298]). The area per lipid increased for membranes containing ethanol, while it

decreased for membranes containing decanol or tetradecanol (see Table 3.5 and Fig. 3.5). For the lower octanol concentrations, the analysis showed a slight decrease of the area per lipid, while for high concentrations an increase was found. For a DMPC-ethanol system containing monovalent ions (system E8), the area per lipid was 63.75 ± 0.81 Å^2 due to the coordination of cations by the lipid carbonyl groups [24].

The increase in the area per molecule for ethanol is in agreement with micropipette aspiration experiments by Ly and Longo [148, 149] as well as our own experimental results (see below).

# 1-alkanols	Ethanol ApL (Å^2)	Octanol ApL (Å^2)	Decanol ApL (Å^2)	Tetradecanol ApL (Å^2)
8	64.38 ± 0.56	63.60 ± 0.59	63.88 ± 0.88	64.03 ± 0.54
24	64.74 ± 0.98	63.45 ± 0.78	62.69 ± 0.67	61.49 ± 0.53
72	67.18 ± 0.54	63.44 ± 0.96	59.80 ± 0.32	60.57 ± 0.31
128	70.96 ± 0.53	64.38 ± 0.28	-	-
185	-	68.49 ± 0.25	-	-

Table 3.5: Average area per lipid (ApL) for the different simulations with 128 lipids. For the simulation of a pure bilayer in water, the average area per lipid was calculated to be 64.15 ± 0.77Å^2. For simulations E2, E3, and TD3, equilibration times of 15, 30, and 15 ns were used.
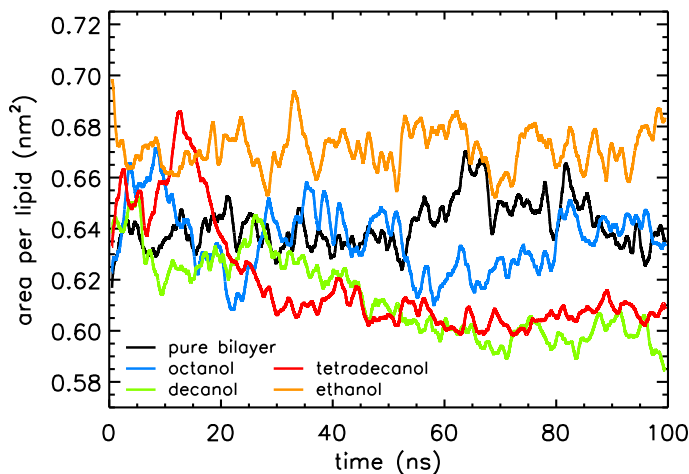
Figure 3.5: Area per lipid for the bilayer in the solutions with 72 molecules of the respective 1-alkanol as a function of time. The values were smoothed by averaging over time intervals of 1 ns (sliding window procedure).

Combining the results for the area per lipid and the thickness of the bilayer (Table 3.4), the volume per lipid was computed (Table 3.6). For the pure bilayer, the volume per lipid was $V_{\mathrm{DMPC}} = (1.11 \pm 0.01)$ nm^3. This compares well to the experimental value of

$V_{\mathrm{DMPC}} = 1108\,\mathrm{\AA}^3$ at $T = 309\,\mathrm{K}$ reported by Nagle and Wilkinson [178]. The average lipid volume increased only slightly with increasing 1-alkanol concentration.

# 1-alkanols	Ethanol V (nm^3)	Octanol V (nm^3)	Decanol V (nm^3)	Tetradecanol V (nm^3)
8	1.11 ± 0.01	1.12 ± 0.01	1.12 ± 0.02	1.13 ± 0.01
24	1.12 ± 0.02	1.14 ± 0.02	1.14 ± 0.02	1.15 ± 0.01
72	1.16 ± 0.01	1.21 ± 0.02	1.20 ± 0.01	1.23 ± 0.01
128	1.19 ± 0.01	1.28 ± 0.01	-	-
-	-	1.38 ± 0.01	-	-

Table 3.6: The volume V per lipid for the different simulations with 128 Lipids. For the pure bilayer in water, a value of (1.11 ± 0.01) nm^3 was found.

Bending Modulus and Elasticity

In the following, we investigated the influence of 1-alkanols on the elastic properties of the DMPC bilayer. The bending moduli of the different systems were calculated by a fit of the intensity of the bilayer undulations observed in the simulations (compare Section *Materials and Methods* and see Fig. 3.6). The values are summarized in Table 3.7. They were obtained using a time resolution of $\Delta t = 10\,\mathrm{ps}$, a grid spacing $g \approx 0.2\,\mathrm{nm}$, and a width of the Gaussian function of $\sigma = 0.8\,g$. The first 6 ns (7 ns) (512 (2048) lipids) of the trajectories were omitted in the analysis to account for equilibration of the systems (see Section *Equilibration Times*). The error was estimated by block averaging over time. The time window was adjusted such that the autocorrelation of the undulatory modes with the largest wavelength drops below 0.2. The bending moduli denoted with a superscript 'av' were calculated by averaging the grid coordinates of both lipid monolayers; values denoted with 'up' or 'low' correspond to the analysis of individual monolayers.

System	# DMPC	k_c^{av} (10^{-20} J)	k_c^{up} (10^{-20} J)	k_c^{low} (10^{-20} J)
C2	512	2.5 ± 0.2	1.5 ± 0.1	1.5 ± 0.1
C3	2048	3.2 ± 0.1	2.1 ± 0.1	2.1 ± 0.1
E5	512	2.2 ± 0.1	1.5 ± 0.1	1.3 ± 0.1)
E6	2048	2.6 ± 0.3	1.7 ± 0.2	1.6 ± 0.2
O6	512	2.5 ± 0.2	1.7 ± 0.1	1.5 ± 0.1
O7	512	3.6 ± 0.3	2.1 ± 0.2	2.5 ± 0.2
08	2084	4.5 ± 0.1	3.2 ± 0.1	3.2 ± 0.1
D4	512	3.6 ± 0.4	1.9 ± 0.3	2.1 ± 0.4
TD4	512	2.7 ± 0.2	1.8 ± 0.2	1.1 ± 0.1

Table 3.7: The bending moduli for the different simulation systems. k_c^{av} was calculated by averaging over the two monolayers; $k_c^{\mathrm{up/low}}$ gives the bending modulus for the upper/lower monolayer separately.
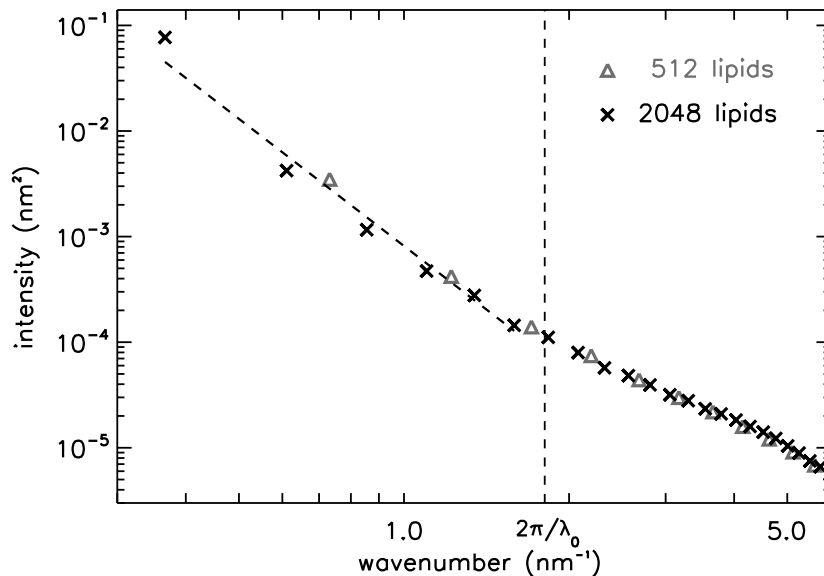
Figure 3.6: Intensity of undulations (scaled for the different patch sizes) versus wave number for the simulation systems C2 (512 lipids) and C3 (2048 lipids) (pure bilayers). The elasticity is obtained by fitting the intensity at low wavenumbers ($< 2\pi/\lambda_0$, λ_0 = membrane thickness).

In agreement with the experiments of Ly et al. [148, 149], ethanol decreased the bending modulus of the bilayer. On the other hand, at larger concentrations the long-chain 1-alkanols octanol and decanol stiffened the bilayer.

The asymmetric distribution of the tetradecanol molecules inside the bilayer (62.5% of the tetradecanol molecules went into the upper monolayer), led to a persistent (asymmetric) local thinning of the membrane. Thereby, the flexibilities both of the monolayers and of the bilayer are presumably overestimated. For symmetric insertion, we would thus expect a stiffening also for tetradecanol-containing membranes. In general, the bending moduli of the monolayers are smaller than the ones of the corresponding bilayer, because in the latter case peristaltic motions were averaged out, while these motions contribute when calculating the bending moduli of the separate monolayers. Systems with 2048 lipids shifted the bending moduli to $20 - 30\%$ larger values compared to the four times smaller systems, reflecting possibly not fully developed undulations at large wavelengths.

An analysis of the spectral intensity as a function of the frequency and the wave number showed that small frequencies dominate in the small wave number region ($2\pi/\lambda_0 \approx 1.8\,\mathrm{nm}^{-1}$), that is crucial in the calculation of the bending modulus (Fig. 3.7).

For direct comparison to compressibility experiments (see below), the area compressibility K_A was determined as well. Assuming a statistical ensemble, it can be calculated from the area fluctuations of the bilayer according to [4, 72, 141]

$$K_A = \frac{k_B T \cdot A}{\langle \delta A^2 \rangle} \quad , \tag{3.13}$$

where A is the bilayer area. Within the large error margins, long-chain alkanols at mod-
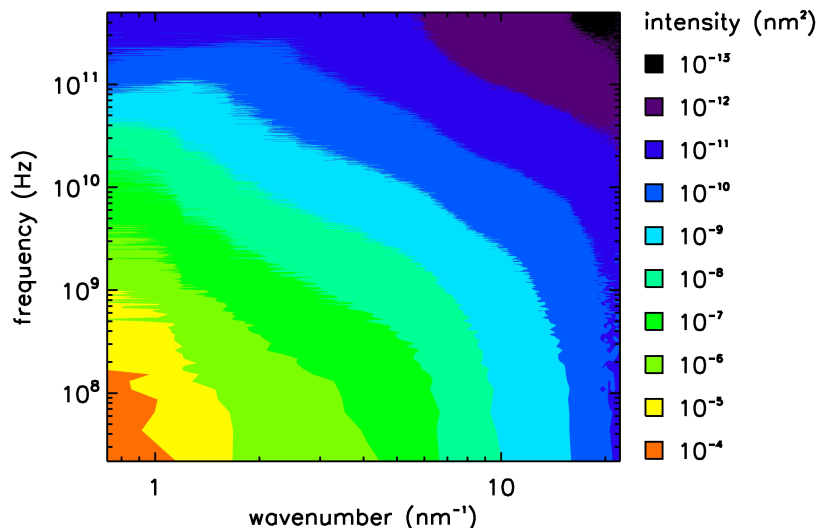
Figure 3.7: A contour plot of the intensity as a function of the wave number and the frequency for the system C2. A time interval of $46\,\mathrm{ns}$ was analyzed with a time resolution of $1\,\mathrm{ps}$. The intensity shows a sharp peak for low frequencies and small wave numbers.

erate to high concentrations increased the area compressibility by a factor of $3-8$ with respect to pure DMPC bilayers, while no effect was seen for ethanol (within the error bars). The area compressibility for pure DMPC ($K_A = 300\ldots700\,\mathrm{mN\,m^{-1}}$) is at least a factor of two larger than the respective experimental values ([65] and values in this manuscript). However, the results (see Section *Supplementary Material*) show a strong dependence on the length of the simulation as well as on the selected time interval, indicating undersampling of the fluctuations [72]. This undersampling is presumably coupled to an underestimation of the fluctuations, impeding a quantitative comparison to experiment.

Diffusion Coefficient

In Fig. 3.8 the lateral diffusion coefficients of the lipid headgroups, calculated and averaged for the systems with 128 and 512 lipids containing 72 and 288 1-alkanols, respectively, and for the control simulations of pure DMPC, are compared with results from the continuous bleaching experiments (see below). The addition of long-chain 1-alkanols decreased the lipid diffusion coefficient compared to pure DMPC, while addition of ethanol slightly increased it. These results are in line with the described changes in the area per lipid. For octanol, decanol, and tetradecanol, the area per lipid was decreased, i. e., the lipids were more closely packed than for a pure DMPC bilayer. Additionally, hydrogen bonds that were formed between the long-chain 1-alkanols and the lipids were rather long-lasting and thereby larger complexes with a decreased diffusion coefficient could be formed. For ethanol in turn the opposite effect held true: the area per lipid was enlarged,

resulting in an increase of the average distance between the lipids. Ethanol-lipid complexes are comparable to single lipids in size and weight and are therefore expected to exhibit similar diffusion properties as lipids in ethanol-free bilayers.

Quantitatively, the simulation result $D_{\mathrm{L}}^{\mathrm{sim}} = (10.4 \pm 0.6)\ \mu\mathrm{m}^2\ \mathrm{s}^{-1}$ for the pure DMPC bilayer compares well with published values; for example, Filippov et al. [73] reported a value $D_{\mathrm{L}} \approx 11\ \mu\mathrm{m}^2\ \mathrm{s}^{-1}$ at $T = 308\,\mathrm{K}$ for the lateral diffusion coefficient of lipids in DMPC bilayers with $35\,\mathrm{wt\%}$ of $^2\mathrm{H}_2\mathrm{O}$. In agreement with our simulation results, an increase in the lipid diffusion in the presence of ethanol was reported in earlier experimental studies of ethanol-altered membrane fluidity in erythrocyte and brain membranes by Chin and Goldstein [44] and in studies of the lipid mobility in neural crest cells by Chen et al. [43].
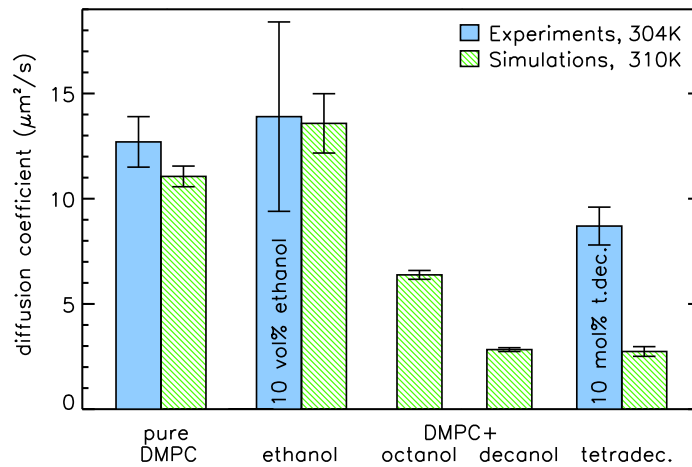

Figure 3.8: Comparison between the experimental and simulated values for the lateral self-diffusion coefficient of the lipids. The simulation data were taken from the systems with 512 lipids and 288 1-alkanol molecules.

3.3.2 Experiments

Diffusion Coefficient

Continuous bleaching (CB) experiments were performed using solutions of $10\,\mathrm{vol\%}$ of ethanol or $10\,\mathrm{mol\%}$ of tetradecanol. In the presence of ethanol the diffusion constant remained almost constant (minimal increase) in relation to a pure membrane. However, the data exhibit a rather large error bar. We assume that the presence of ethanol disturbs the membrane cushion causing some heterogeneity in the lipid bilayer, which would indeed result in an increased error bar. This assumption was confirmed by diffusion measurements on the bare glass slide without further support; here, the error decreased while the diffusion coefficient remained slightly enlarged.

In the case of tetradecanol, a clear decrease in the diffusion coefficient was found in agreement with the simulation (Fig. 3.8). Although the general tendency as well as the order of magnitude is preserved, there are discrepancies in the absolute values. The difference in temperature and the necessity of a soft support cannot be excluded to affect the measurement of the diffusion constant. Considering all these factors the good agreement between the experiments and the simulations is remarkable.

Film Balance Experiments

A: Compressibility Measurements

By monitoring a pressure-area isotherm on a film balance, the isothermal compressibility κ_T of a monolayer can be calculated by applying Eq. (3.10). In Fig. 3.9, the isothermal compressibility of a pure DMPC monolayer compared to a DMPC monolayer with 2 vol% ethanol in the subphase or $10 \, \text{mol}\%$ tetradecanol in the monolayer is shown. The presence of a pronounced peak, which represents the lipid phase transition, was necessary to assign the compressibility of the fluid phase. To assure such a clear criterion for the distinction between the two phases the compressibility of DMPC/ethanol and DMPC/tetradecanol was measured at slightly different temperatures. As described in the Section *Materials and Methods*, the onset of the fluid phase was taken as the lower left of the shoulder in Fig. 3.9 defined by the two adjacent tangents (dotted lines).

Although the absolute value of κ_T might slightly depend on the temperature, the order of magnitude and the change in κ_T when adding 1-alkanols are not expected to vary significantly over the relatively small relevant temperature interval. From Fig. 3.9 we find an increase in isothermal compressibility in the presence of ethanol by approximately 80%. When adding tetradecanol however, the membrane becomes roughly 30% stiffer. In the fluid phase with non-coupling monolayers, the bending modulus k_c of a bilayer can be approximated by the monolayer isothermal compressibility according to [22, 66, 216]

$$k_c \quad \approx \quad \frac{2}{a} \frac{d^2}{\kappa_T} \, , \tag{3.14}$$

where d denotes the membrane thickness of the bilayer, κ_T is the isothermal compressibility of the monolayer in the fluid phase, and a is a numerical constant which depends on the details of the model. For two leaflets free to slide past each other, a was estimated to be 48 [22]. This model has been applied here. Taking d from the simulations (Table 3.4) and κ_T from the experiment, Eq. (3.14) yields a bending modulus of $(3.0 \pm 0.6) \times 10^{-20}$ J $((2.0 \pm 0.4) \times 10^{-20}$ J) for the pure DMPC membrane at $13.0°$ C $(7.5°$ C). For the ethanol treated membrane the bending modulus is decreased $((1.6 \pm 0.3) \times 10^{-20}$ J), while it is increased for the membrane containing tetradecanol $((3.2 \pm 0.6) \times 10^{-20}$ J). This is in good agreement with the simulation results for the bending moduli (Table 3.7). Both theoretical and experimental findings therefore demonstrate that addition of tetradecanol in the membrane decreases the compressibility and consequently increases the bending modulus, while ethanol has the reverse effect (see also Tierney et al. [264]).
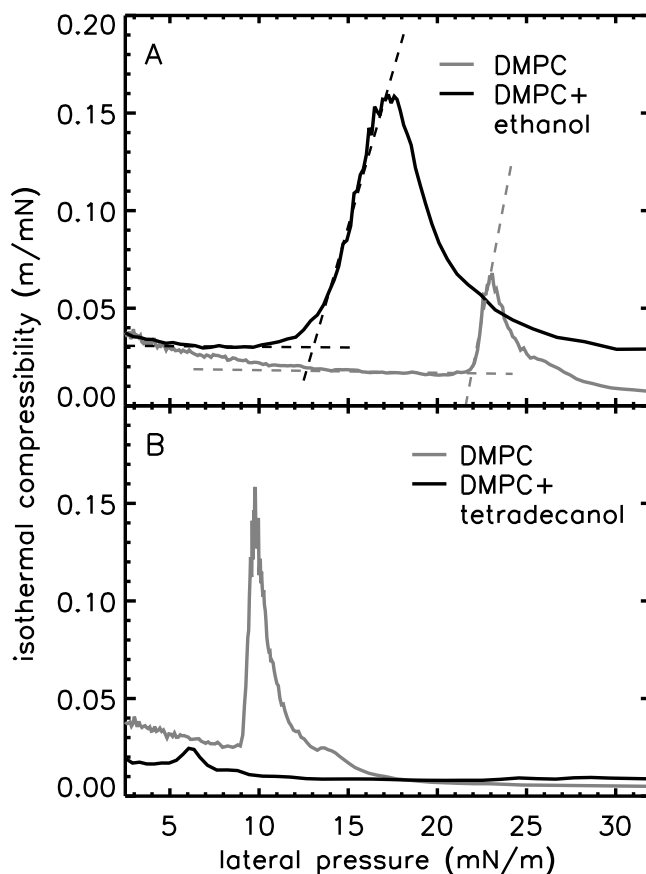
Figure 3.9: Isothermal compressibility as a function of applied lateral pressure as obtained from film balance experiments on DMPC monolayers with and without ethanol ($T = 13°$ C) or tetradecanol ($T = 7.5°$ C). The left side from the intersection of the tangents (dotted lines) denotes the liquid expanded phase. The x-coordinate of this intersection distinguishes the onset of the liquid expanded phase while the y-coordinate defines the isothermal compressibility κ_T ($\kappa_T \approx 0.017 \frac{m}{mN}$ for a DMPC monolayer with water subphase and $\kappa_T \approx 0.031 \frac{m}{mN}$ for a DMPC monolayer on a water subphase containing 2 vol% ethanol at $T = 13°$ C). For the sake of clarity only two pairs of tangents are shown. During analysis several tangents have been applied providing the error bar given in the text. Different temperatures have been chosen for experimental convenience, as it allows to clearly define the onset of the liquid expanded phase, which can only be observed in certain temperature intervals.

B: Area per Lipid

Film balance experiments allow to monitor the change in the average area per molecule as a function of temperature and pressure in the presence and absence of 1-alkanols very precisely. As the fluid phase extends over a certain pressure or temperature interval, the average area per molecule in this phase is not constant. In order to compare our experimental data to the simulations, we calculated the relative change in area per molecule

with and without 1-alkanol for some reference point taken as the lower left of the shoulder in Fig. 3.9. When looking at the isotherm (data not shown), the resulting pressure corresponds to an increase in area per molecule of approximately 20% in the presence of 2 vol% ethanol in the subphase. The change in area per molecule in the presence of tetradecanol was evaluated following the same protocol. However, since tetradecanol is not water soluble, it was not added into the subphase, but directly mixed with the DMPC/chloroform solution before spreading. A decrease in the area per molecule of roughly 10% could be calculated from Fig. 3.9 and the corresponding isotherm. Thus, experiment and simulations do agree in their general tendency of an increase in area per lipid in the presence of ethanol and decrease with tetradecanol.

Microcalorimetry

In Fig. 3.10, the heat capacity profiles for DMPC in the presence and absence of 1-alkanols are illustrated. The existence of $10\,$vol% ethanol in the bath shifts the phase transition temperature of DMPC with respect to the pure system by $2.2\,$K to lower temperatures. This clearly indicates that ethanol incorporates into the membrane and stabilizes the fluid phase. Thus one would expect a reduced order parameter and a decreased packing density with increasing ethanol concentration at constant temperature.

These findings are in agreement with our simulations (see Fig. 3.3) and NMR studies by Barry and Gawrisch [11]. Assuming that ethanol only incorporates into the fluid phase of the lipid membrane, the formula for the melting point depression (see Eq. (3.11)) can be applied. A shift of $2.2\,$K at $10\,$vol% ethanol leads to a fraction of approximately six ethanol molecules per 100 DMPC molecules. The thermodynamic partition coefficient is therefore estimated to $K_p \approx 2$, in good agreement with earlier studies [130]. In contrast, the addition of tetradecanol stabilizes the gel phase of the membrane by shifting the phase transition to higher temperatures. Therefore, tetradecanol is expected to increase both the order parameter and the packing density of the lipids. Since the number of tetradecanol molecules in the subphase is unknown (see Section *Materials and Methods*), a partition coefficient cannot be given. However, experiments and simulations are once more in excellent agreement.

Our conclusion of an enhanced packing density for DMPC membranes treated with tetradecanol and a decreased packing density after incorporation of ethanol derived from the DSC experiments are qualitatively in agreement with findings of Aagaard et al. [1], obtained by vibrating tube densitometry.
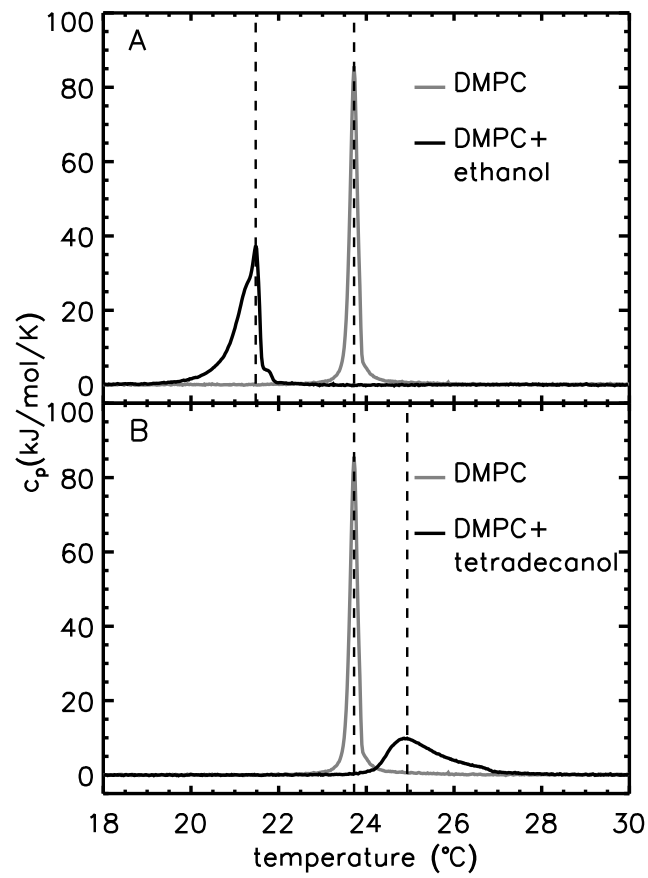
Figure 3.10: Heat capacity profile for DMPC in the presence and absence of ethanol and tetradecanol.

3.4 Summary and Conclusions

We have shown that 1-alkanols of different chain length exert a profound influence onto the structure and dynamics of DMPC bilayers. In the simulations, all 1-alkanols diffused into the bilayer very quickly. While the partition coefficients of the long-chain 1-alkanols octanol, decanol, and tetradecanol matched experimental values, the partition coefficient of ethanol was overestimated. Usage of a refined force field could partially resolve this issue. The 1-alkanol's hydroxyl group preferentially hydrogen bonded to the lipid carbonyl atoms and the carbon chains of the long-chain 1-alkanols aligned with the lipid carbon chains. In agreement with differential scanning calorimetry (DSC) experiments, the simulations showed that long-chain 1-alkanols increase the lipid order and decrease the fraction of lipids being in gauche conformation (see Section *Supplementary Material*). Order parameters determined from the simulations allowed to unambiguously reassign the peaks in the spectra obtained by NMR experiments on multiple deuterated lipids. The area per lipid is increased and the bilayer is slightly thinned by adding ethanol. In contrast, long-chain 1-alkanols had the reverse effect on the membrane structure (Fig. 3.11).
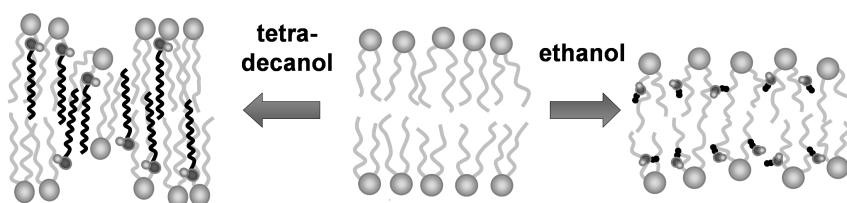

Figure 3.11: Sketch of structural lipid bilayer changes upon addition of ethanol and tetradecanol.

For the lipid dynamics and the elasticity of the bilayer, the same antagonism held true: ethanol increased the diffusion coefficient of the lipids (in the simulations) and decreased the bending modulus of the bilayer, while the long-chain 1-alkanols decreased the lipid diffusion coefficient and increased the bending modulus. The total volume of the hydrophobic bilayer core was slightly increased by the inclusion of any 1-alkanol, yet these changes seem to be too small to lend support to volume expansion theories of anesthesia. The main predictions of the MD simulations were confirmed by continuous bleaching experiments, DSC measurements, and film balance experiments for ethanol and tetradecanol. Qualitative agreement was obtained between the simulations and the experimental results for the diffusion coefficient and the bilayer elasticity. In DSC measurements, differential shifts of the phase transition temperature were found for ethanol and tetradecanol. The increase in lipid order by long-chain 1-alkanols in combination with the increase in bending modulus and the thickening of the bilayer can be interpreted as a stabilization of the lipid bilayer gel phase.

The reported structural and dynamical changes of the bilayer properties by the insertion of 1-alkanols may partly be responsible for the anesthetizing and permeation enhancing effect of these drugs: the changes in the bilayer thickness could cause a mismatch between the lipid matrix and embedded membrane proteins and modify protein-bilayer

hydrophobic interactions. Thus, for proteins undergoing conformational changes at the protein-bilayer interface, the conformational equilibrium between different states could be shifted. In a similar way, the protein function could as well be regulated by the bilayer elasticity [147], which was modulated by 1-alkanols, too. Asymmetric insertion of long-chain 1-alkanols may moreover lead to a considerably transient local thinning and probably destabilization of the membrane.

In order to elucidate the mechanism of anesthetics at the atomic scale and to distinguish between indirect effects via a change of the membrane properties and direct effects upon binding of anesthetics to the respective target proteins, future work will require the study of potential targets for anesthetics like ion channels embedded in explicit multicomponent membranes.

3.5 Acknowledgment

Author Contributions:

Rainer A. Böckmann designed research. The experiments were done in the group of Matthias F. Schneider in Augsburg. The simulations were set up by Beate Griepernau. Analysis was done by Beate Griepernau and partly by Simon Leis within the scope of his Bachelor thesis, in cooperation with Beate Griepernau. The article was written by Beate Griepernau and Rainer A. Böckmann and the experimental sections were contributed by Matthias F. Schneider.

3.6 Appendix: Supplementary Material

3.6.1 Molecular Dynamics Simulations

Trans/Gauche Distribution of Lipid Tails

The changes in the lipid order parameters are mirrored by the distribution of dihedral angles of the lipid carbon chains. A conformation is called *gauche⁻* state for dihedral angles $\alpha = -60° \pm 60°$, it is called *gauche⁺* state for $\alpha = +60° \pm 60°$ and *trans* state for $\alpha = 180° \pm 60°$.

Fig. 3.12 shows the fraction of dihedral angles in the gauche$^\pm$ conformations. All investigated 1-alkanols with the exception of ethanol reduced the fraction of lipid chain dihedrals in the gauche$^\pm$ conformations. This ordering effect increases with the length of the 1-alkanols.
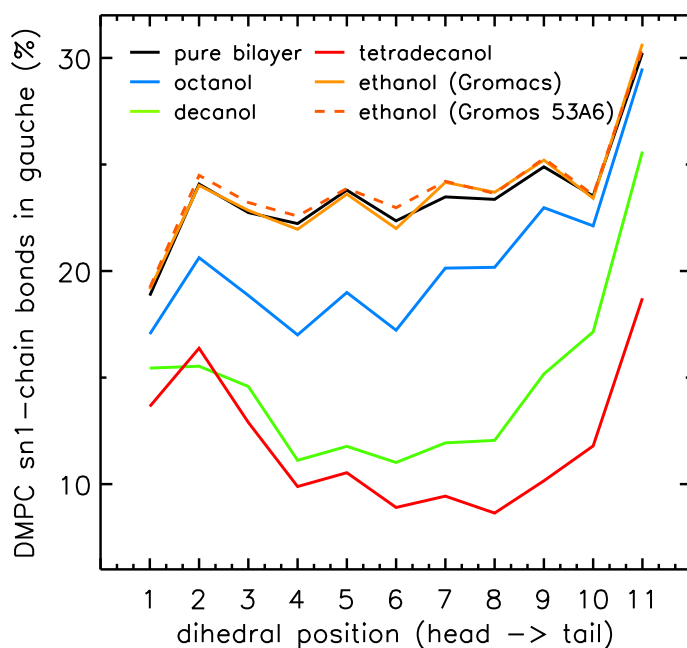
Figure 3.12: The percentage of dihedral angles in gauche conformation averaged over all bilayer lipids and over a time interval of $10\,\mathrm{ns}$. The dihedral angles are numbered from the outside to the inside of the bilayer.

Dipole Moment of the Lipid Headgroups

According to Seelig et al. [232], changes in the dipole orientation of the lipid headgroups can induce high local electric fields of up to $10^5\,\mathrm{V}\,\mathrm{cm}^{-1}$. Such high fields can be of importance in any process depending on the permeability of the bilayer. Therefore, the orientation of the lipid dipole moments and the electric field across the bilayer are investigated here.

For pure phosphatidylcholine bilayers, neutron diffraction experiments of Seelig et al. [30,

31, 233] established an "essentially parallel (within 30°) alignment" of the phosphoglyc-
erol polar groups to the plane of the membrane. In the simulations with 72 1-alkanols and
128 lipids, a broad distribution of angles θ between the lipid dipoles and the membrane
normal was observed (see Fig. 3.13). In the case of the pure DMPC bilayer, the aver-
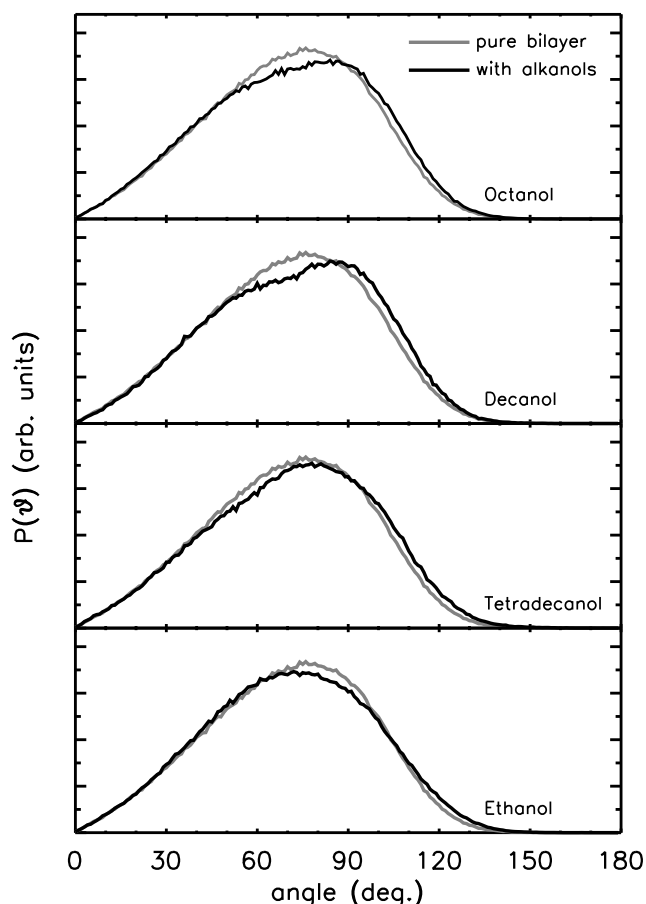
Figure 3.13: Distribution of angles between the lipid dipole moments and the bilayer normal for the simulation systems O3, D3, TD3 and E3 (containing 72 1-alkanol molecules each).

age angle was $\bar{\theta} = 70.6°$. After insertion of 1-alkanols, the angle distribution broadened
slightly (see Fig. 3.13) with the mean angles shifted towards larger values for the long-
chain 1-alkanols (see Table 3.8). The maximum θ_{max} of the angle distributions increased
with increasing 1-alkanol concentration for octanol and decanol, but decreased for an in-
creasing number of tetradecanol molecules. These changes in the lipid dipole orientations
had only minor influence on the electrostatic potential across the lipid bilayer (Fig. 3.14).

Area Compressibilities Derived from MD Simulations

Area compressibilities have been derived from all simulations according to

$$K_A = \frac{k_B T \cdot A}{\langle \delta A^2 \rangle} \tag{3.15}$$

# 1-al-kanols	Ethanol angle (°)		Octanol angle (°)		Decanol angle (°)		Tetradecanol angle (°)	
	$\bar{\theta}$	$\theta_{\max} \pm \tilde{\theta}$	$\bar{\theta}$	$\theta_{\max} \pm \tilde{\theta}$	$\bar{\theta}$	$\theta_{\max} \pm \tilde{\theta}$	$\bar{\theta}$	$\theta_{\max} \pm \tilde{\theta}$
8	70.6	78^{+29}_{-43}	71.0	75^{+32}_{-40}	70.8	76^{+31}_{-41}	70.8	81^{+26}_{-45}
24	70.9	72^{+35}_{-37}	70.9	80^{+28}_{-45}	71.1	83^{+24}_{-47}	71.3	80^{+27}_{-42}
72	70.9	72^{+35}_{-38}	71.5	84^{+26}_{-50}	72.3	84^{+26}_{-49}	72.4	78^{+31}_{-42}

Table 3.8: Average angle $\bar{\theta}$ between the lipid dipole moment and the bilayer normal, angle $\theta_{\max}$ at the maximum of the angle distribution function (see Fig. 3.13), and width of the distribution $\tilde{\theta}$ at half maximum averaged over all times starting at the respective equilibration times (see Table 3.2). For the pure DMPC bilayer, an average angle of $70.6°$ was found ($\theta_{\max} = 76°^{+30}_{-39}$).
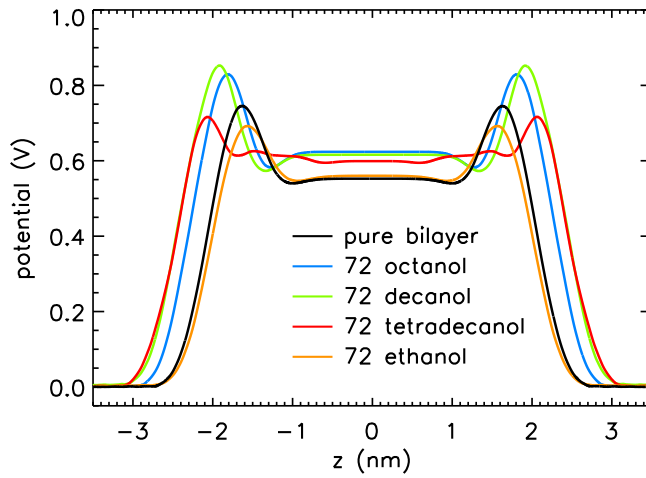
Figure 3.14: Electrostatic potential across the DMPC bilayer (128 lipids) for different inserted 1-alkanols. The broadening of the potential resulted from the increased thickness of the bilayer after insertion of long-chain 1-alkanols.

and are summarized in Table 3.9. The analyzed simulation time intervals were chosen equal for all simulations of similar size. Where possible, two independent intervals of the same length are given, reflecting the large statistical error caused by an undersampling of the fluctuations. The statistical error of the respective area compressibilities were calculated by approximating the error of the area fluctuations. The latter depends on the relaxation time τ of the correlation function of the area fluctuations according to $\sigma^2 = (2\tau/T)\langle \delta A^2 \rangle^2$ (discussed thoroughly in [72]).

# lip.	# alk.	time (ns)	Ethanol K_A ($\frac{\text{mN}}{\text{m}}$)	Octanol K_A ($\frac{\text{mN}}{\text{m}}$)	Decanol K_A ($\frac{\text{mN}}{\text{m}}$)	Tetradecanol K_A ($\frac{\text{mN}}{\text{m}}$)
128	8	$60-100$	437 ± 121	638 ± 133	527 ± 135	405 ± 102
		$20-60$	730 ± 161	511 ± 96	215 ± 89	821 ± 140
	24	$60-100$	409 ± 107	325 ± 101	492 ± 139	720 ± 173
		$20-60$	214 ± 78	-	450 ± 136	-
	72	$60-100$	493 ± 125	414 ± 180	1141 ± 265	1794 ± 449
	128	$60-100$	621 ± 117	2360 ± 403	-	-
	185	$60-100$	-	3935 ± 753	-	-
512	96	$6-31$	-	409 ± 137	-	-
	288	$6-31$	579 ± 151	476 ± 158	1889 ± 362	2457 ± 676
2048	1152	$8-23$	389 ± 127	662 ± 243	-	-

Table 3.9: Area compressibilities calculated from the bilayer area fluctuations. For the simulations without 1-alkanols the values for the area compressibilities are as follows: 128 lipids: $(335 \pm 148) \frac{\text{mN}}{\text{m}}$ ($60-100$ ns) and $(692 \pm 128) \frac{\text{mN}}{\text{m}}$ ($20-60$ ns); 512 lipids: $(347 \pm 123) \frac{\text{mN}}{\text{m}}$ ($6-31$ ns) and $(663 \pm 112) \frac{\text{mN}}{\text{m}}$ ($27-52$ ns); and 2048 lipids: $(542 \pm 125) \frac{\text{mN}}{\text{m}}$ ($8-23$ ns).

4 The Influence of 1-Alkanols and External Pressure on the Lateral Pressure Profiles of Lipid Bilayers

Beate Griepernau [1]   *and Rainer A. Böckmann* [1]

The suggestion by Robert Cantor, that drug-induced pressure changes in lipid bilayers can change the conformational equilibrium between open and closed states of membrane proteins and thereby cause anesthesia, attracted much attention lately. Here, we studied the effect of both large external pressure and of 1-alkanols of different chain lengths – some of them anesthetics, others not – on the lateral pressure profiles across dimyristoylphosphatidylcholine (DMPC) bilayers by molecular dynamics simulations. For a pure DMPC bilayer, high pressure both reduced and broadened the tension at the interface hydrophobic/hydrophilic and diminished the repulsion between the phospholipid headgroups. Whereas the effect of ethanol on the lateral pressure profile was similar to the effect of a large external pressure on a DMPC bilayer, long-chain 1-alkanols significantly amplified local maxima and minima in the lateral pressure profile. For most 1-alkanols, external pressure had moderate effects and did not reverse the changes 1-alkanols exerted on the pressure profile. Nevertheless, assuming the bent helix model as a simple geometric model for the transmembrane region of a membrane protein, protein conformational equilibria were shifted in opposite directions by addition of 1-alkanols and additional application of external pressure.

---

[1]Theoretical and Computational Membrane Biology, Center for Bioinformatics Saar, Saarland University, PO Box 15 11 50, 66041 Saarbrücken, Germany

4.1 Introduction

Although the phenomenon of general anesthesia has been known for a long time, the underlying mechanism is not yet understood [275]. There is an ongoing debate about whether general anesthesia is caused by a specific binding of anesthetics – amongst them the 1-alkanols, up to a chain-length of about 12 carbon atoms (see, e. g., Pringle et al. [206]) – to membrane proteins [81] or by a nonspecific, lipid-mediated mode of action. In the latter case, the drugs are supposed to induce changes in lipid bilayers, which in turn alter the conformational equilibrium between different states of membrane proteins. A further alternative lipid-mediated mechanism for anesthetic action has recently been suggested on the basis of a soliton model for signal propagation in nerves [99]: Assuming that nerve pulses travel as solitons along cell membranes, a melting point depression caused by anesthetics would impede signal transduction and thereby cause anesthesia [100, 101]. General anesthesia can be reversed by the application of external pressure [93, 115, 116, 139, 166]. These two antagonizing mechanisms – anesthesia and its pressure reversal – are not necessarily coupled, but it is likely that they are related in some way. Here, we tested whether the model for a lipid-mediated mode of operation suggested by Robert Cantor [33–35] can also account for pressure reversal of anesthesia in a simple manner.

Cantor's idea [33–35] is based on the premise that there is a variation of the cross-sectional area difference between the closed and the open conformation of membrane proteins in the direction of the bilayer normal. If this assumption is fulfilled, a change in the lateral pressure profile of lipid membranes caused by anesthetics could shift the equilibrium between the open and closed conformation of membrane ion channels and thereby cause anesthesia. A simple mechanism for pressure reversal of anesthesia would then be a shift of the conformational equilibrium of these membrane proteins in the opposite direction by external pressure.

Cantor's model has not been tested yet, as the lateral pressure profile of membranes or lipid bilayers is difficult to determine in experiments. Up to now, only qualitative measurements of the pressure distribution in the bilayer chain region were achieved: Templer et al. [258] doped mixed bilayers composed of varying concentrations of dioleoylphosphatidylcholine and dioleoylphosphatidylethanolamine with di-pyrenyl phosphatidylcholine probes of different chain lengths. These doped bilayers were then used for fluorescence measurements, where the rate of the eximer to monomer signal of the pyrenes was assumed to be a measure of the pressure in the bilayer. Upon increase of the dioleoylphosphatidylethanolamine concentration, the total lateral pressure in the chain region was increased and a transfer of lateral pressure away from the heads towards the ends of the carbon chains occurred. Applying a similar technique, Kamo et al. [121] found that the lateral pressure in mixed bilayers composed of 1-palmitoyl-2-oleoylphosphatidylcholine and 1-monoolein increased as a function of the monoolein fraction as long as the bilayer was in the lamellar phase, had a discontinuity in the phase transition regime, and was approximately constant in the cubic phase. Addition of the peptide 18A lowered the lateral pressure only in the acyl chain region at the bilayer interface.

In theoretical studies, analytical and statistical methods, mean-field approaches, Monte Carlo techniques, and coarse-grained models [33, 35–38, 83, 85, 95, 172, 236, 249, 250, 289, 302] as well as all-atom molecular dynamics (MD) simulations [40, 90, 91, 142, 184,

190, 191, 195, 259] have been used to calculate lateral pressure profiles of lipid bilayers. Based on all-atom MD simulations, Lindahl and Edholm [142] classified all terms contributing to the lateral pressure according to their physical origin (electrostatic, Lennard Jones, dihedral, or other bonded interactions) and the interacting molecules (pairwise contributions of lipid chains, headgroups, or water molecules) and distinguished between energetic and entropic contributions to the surface tension. Similar studies have been performed by other authors: Gullingsrud and Schulten [91] explored the impact of simulation and analysis parameters on the calculation of pressure profiles across bilayers consisting of various lipids and studied the influence of the lateral pressure distribution on the gating process of the mechanosensitive channel MscL applying a simple geometric model. Later, Gullingsrud et al. [90] computed the pressure profile of a protein-lipid system (melittin embedded in a dimyristoylphosphatidylcholine (DMPC) bilayer) and found that the overall pressure distribution of this system was only moderately changed compared to a pure DMPC bilayer. Patra [195] investigated the changes in the lateral pressure profile of a dipalmitoylphosphatidylcholine (DPPC) bilayer upon addition of cholesterol. Carrillo-Tripp et al. [40] detected that the magnitude of the chain pressure near the headgroup-tail interface was enlarged for lipid bilayers containing docosahexaenoic acids (DHA) compared to simulations of bilayers made of only saturated or monounsaturated lipids. The usage of docosapentaenoic acid instead of docosahexaenoic acid, that is accompanied by a shift of the maximum density of unsaturated bonds towards the bilayer core, did not yield such effect. Niemela et al. [184] probed the pressure profiles of raft-like bilayers. Various sterols, all of them with a structure very similar to cholesterol, exerted significant changes on the pressure profiles of lipid bilayers, especially in the case of unsaturated bilayer lipids [190]. Ollila et al. [191] observed that the central maximum in the lateral pressure profile decreased upon increasing lipid chain unsaturation whereas all other peaks increased in height. Recently, Terama et al. [259] reported that ethanol diminished the magnitude of the peaks in the lateral pressure profiles of DPPC and palmitoyl-docosahexaenoyl-phosphatidylcholine lipid bilayers in the region of the lipid headgroups. Using a coarse-grained approach, Frischknecht and Frink [83] found that ethanol, butanol, and hexanol did not alter the shape of the pressure profile curve of the pure bilayer, but that these alcohols reduced the magnitude of all peaks. Thickness changes of the bilayers upon addition of alcohols were reflected by a shift of the pressure profile peaks along the bilayer normal.

Here, we investigated in all-atom MD simulations, in which way 1-alkanols modify the lateral pressure of lipid bilayers, and in particular whether observed changes are reversed by the application of external pressure. 1-Alkanols are an especially interesting test case, as it was suggested that small alcohols change the lateral pressure in membranes and thereby cause dissociation of embedded KcsA potassium channels [276]. Changes in the structure, the dynamics, and in the local pressure distribution of lipid bilayers in response to anesthetics and external pressure were analyzed from MD simulations of lipid bilayers containing 1-alkanols of different chain lengths at two different pressures. Hypothetical shifts in the conformational equilibria for some simple geometric models of the transmembrane region of a membrane protein upon addition of 1-alkanols and application of large external pressure were calculated.

4.2 Methods

4.2.1 Molecular Dynamics Simulations of Membrane-Alkanol Systems

MD simulations of fully hydrated lipid bilayers containing 1-alkanols of different chain lengths have been carried out at pressures of $1\,\mathrm{bar}$ (see also a previous study [89]) and $1000\,\mathrm{bar}$ using the GROMACS software package version 3.3.1 [18, 143, 278]. Each bilayer consisted of 512 DMPC lipids and was hydrated by a minimum of $22,600$ water molecules; 288 molecules of ethanol, octanol, decanol or tetradecanol were dissolved in each simulation system. The systems were built by quadruplicating equilibrated membrane-alkanol-water systems with 128 DMPC molecules [89]. Additionally, control simulations without 1-alkanols were run. Simulations for the long-chain 1-alkanols octanol, decanol, and tetradecanol at normal pressure were taken from the previous study [89]. Equilibrated snapshots of these simulations were chosen as starting structures for high-pressure simulations. A summary of all simulations is given in Table 4.1.

System name	Number and type of 1-alkanol molecules	Number of water molecules	Pressure (bar)	Simulation time (ns)	Equilibration time (ns)
C1*	none	22,692	1	52	6
C1000	none	22,692	1000	32	6
E1	288 ethanol	24,584	1	53	10
E1000	288 ethanol	24,584	1000	75	20
O1*	288 octanol	26,624	1	33	6
O1000	288 octanol	26,624	1000	70	45
D1*	288 decanol	29,896	1	31	6
D1000	288 decanol	29,896	1000	32	6
TD1*	288 tetradecanol	29,228	1	31	6
TD1000	288 tetradecanol	29,228	1000	34	6

Table 4.1: All simulated systems containing various 1-alkanols. Systems marked by * were already partially analyzed in the previous study [89]. All analysis was done with respect to the given equilibration times.

Hydrostatic pressures to reverse anesthesia in tadpoles range from 140 to $350\,\mathrm{bar}$ [116]. Due to large pressure fluctuations ($\approx \pm 200\,\mathrm{bar}$) in MD simulations of nanoscopic systems, we chose an external pressure of $1000\,\mathrm{bar}$. Experimentally, even higher pressures are applied to lipid bilayers.
All systems were simulated for a minimum of $31\,\mathrm{ns}$ using periodic boundary conditions, a rectangular simulation box, and a constant number of atoms at fixed pressure and temperature $T = 310\,\mathrm{K}$ (NPT-like ensemble). Constraining the bond lengths by the LINCS [106] and SETTLE [169] methods allowed for an integration step size of $2\,\mathrm{fs}$. The lipids and the

water-alkanol solutions were separately coupled to a heat bath at $310\,\mathrm{K}$ using a coupling time constant of $0.1\,\mathrm{ps}$ [16]. External pressures of $1\,\mathrm{bar}$ and $1000\,\mathrm{bar}$ (see Table 4.1) were applied using a weak semi-isotropic coupling to a pressure bath [16] with a time constant of $1\,\mathrm{ps}$ and a compressibility of $4.5 \times 10^{-5}\,\mathrm{bar^{-1}}$.

The simple point charge (SPC) water model [17] was chosen. The force field for the lipids was taken from Berger et al. and Chiu et al. [20, 45]. For the long-chain 1-alkanols, the GROMACS force field (based on GROMOS87) was applied, modified for the partial atomic charges according to MacCallum and Tieleman [151]. Ethanol was simulated using the recently developed GROMOS 53A6 force field [193], as this has been shown to result in a lower partition coefficient in better agreement with experimental values [89]. Note that the Lennard Jones parameter of the lipid hydrocarbon chains and of the 1-alkanols slightly differ from each other. For phospholipids, they were adjusted to reproduce the heat of vaporization for pentadecane [20].

To ensure a correct treatment of the long-range electrostatic interactions, the particle mesh Ewald (PME) method [50] was applied using a Fourier grid spacing of $0.12\,\mathrm{nm}$, a fourth order cubic interpolation, and a relative accuracy of 1.0×10^{-5}. The short-range van der Waals interactions have been accounted for with a cutoff-scheme using a cutoff radius of $1\,\mathrm{nm}$. The neighborlist was updated every 10th integration step.

For details of the calculations of the lipid order parameter, the average headgroup-to-headgroup bilayer thickness d_{HH}, the area per lipid, and the lateral lipid diffusion coefficient, please refer to the previous study [89]. The orientation of the lipid chains was determined in terms of two angles γ and α. γ denotes the angle between the lipid chains and the membrane normal, while α is the angle between the lipid chain vector (defined by the centers of mass of the 3rd and 4th and the 11th and 12th carbon atom of the respective lipid chain), projected onto the membrane plane, and an arbitrarily chosen vector $(1, 0, 0)$. The partition coefficient was calculated from the number of 1-alkanols inside and outside the bilayer at every time step. The criterion for inside/outside was based on the comparison of the z-coordinates of the center of mass of the lipid headgroups (shifted by $0.2\,\mathrm{nm}$ to the bulk water phase) and of the 1-alkanols. The given error is the standard deviation of the partition coefficient obtained by block averaging ($5\,\mathrm{ns}$ windows).

4.2.2 Calculation of Lateral Pressure Profiles

The difference between the lateral and the normal pressure as a function of the normal coordinate of the bilayer, often referred to as local lateral pressure profile, was calculated analogous to the procedure described by Lindahl et al. [142]: The pressure tensor is given by

$$\mathbf{p} = 2\langle \mathbf{E} \rangle - \mathbf{\Sigma} \qquad , \qquad (4.1)$$

where $\mathbf{E}$ is the kinetic energy density tensor and $\mathbf{\Sigma}$ is the configurational stress tensor. In the case of exclusively pairwise interactions between the particles, the bilayer can be divided into horizontal slices of thickness Δz. Here, 100 slices per box were used, result-

ing in a thickness of approximately 1 Å per slice. The local pressure tensor can then be calculated according to the formula [142]:

$$\mathbf{p}_{\text{local}}(z) = \frac{1}{\Delta V} \sum_{i \in \text{slice}} \left(m_i \vec{v}_i \otimes \vec{v}_i \right) - \frac{1}{\Delta V} \sum_{i<j} \left(\vec{F}_{ij} \otimes \vec{r}_{ij} \, f\left(z, z_i, z_j\right) \right) \qquad . \qquad (4.2)$$

The first sum is taken over all particles in the slice at z, whereas all particle pairs in the system contribute to the second term. The z coordinate, mass and the velocity of particle i, and the force and the distance between particles i and j are denoted by z_i, m_i, $\vec{v}_i$, $\vec{F}_{ij}$, and $\vec{r}_{ij}$, respectively. The volume of the slice is ΔV. The function $f\left(z, z_i, z_j\right)$ assigns a weight to the virial depending on the position of the two particles i and j. It is given by [85]

$$f(z, z_i, z_j) = \begin{cases} \Theta(z_i - z)\,\Theta(z + \Delta z - z_i) & \text{for} \quad z_i = z_j \\ \frac{1}{z_j - z_i} \int_{z_i}^{z_j} d\zeta \, \Theta(\zeta - z)\,\Theta(z + \Delta z - \zeta) & \text{otherwise.} \end{cases} \qquad (4.3)$$

$\Theta(z)$ denotes the Heaviside step function, with $\Theta(z) = 0$ for $z < 0$, $\Theta(0) = 1/2$, and $\Theta(z) = 1$ for $z > 0$.

To obtain the pressure profiles from the simulations, reruns of the original trajectories were performed using a modified version of GROMACS 3.0.2, kindly provided by Lindahl and Edholm [142]. Here, the SHAKE [227] algorithm was applied instead of LINCS [106], because pairwise interactions could then be extracted more easily [142]. Sonne et al. [244] showed that the results obtained using PME for the simulations and a cutoff scheme in the reruns are converging towards the correct Ewald results as long as the chosen cutoff is large enough (r_{cutoff} at the order of 1.6-2.0 nm). Here, electrostatic interactions in the reruns were truncated at a cutoff radius of 3.0 nm. For each bin, the diagonal elements of the local pressure tensor were calculated every 100 ps. The values were then averaged over time and a Gaussian smoothing over neighboring bins was performed. Finally, the profiles were symmetrized with respect to the bilayer center.

4.3 Results

4.3.1 Equilibration Times

All starting structures for the high pressure simulations had been equilibrated at a pressure of 1 bar in the previous study [89]. The systems were further equilibrated at high pressure until the thermodynamic partition coefficient K_p of the 1-alkanols in the bilayer, the area per lipid, and the average lipid order parameter had become constant. An equilibration time of 6 ns was found to be sufficient for most of the systems (see Table 4.1). Exceptions were the simulations containing ethanol and the simulation with octanol at a pressure of 1000 bar with equilibration times between 10 ns and 45 ns. For octanol at high pressure, we observed a drastic decrease in the area per lipid and an increase in the lipid order parameter. These changes could possibly hint to a phase transition of the lipid bilayer, as discussed below.

4.3.2 Partition Coefficients

For the simulations with ethanol, thermodynamic partition coefficients (ratio of the mole fraction of 1-alkanols inside the bilayer and the mole fraction of 1-alkanols in the surrounding water) of $K_p = 68 \pm 7$ (1 bar) and $K_p = 61 \pm 5$ (1000 bar) were determined (on average, $189 \pm 8/182 \pm 6$ ethanol molecules were inside the bilayer at $1/1000$ bar). Experimental values for the ethanol-lipid partition coefficient at normal pressure are considerably lower and range from $K_p \approx 2$ to $K_p \approx 28$ [89, 130, 224, 259, 268, 269], depending on the kind of lipids and the experimental conditions. This discrepancy between experiments and simulations has also been observed and discussed in previous studies [89, 196, 259]. Reasons for the overestimated ethanol partition coefficients in the simulations could be inconsistencies in current force fields [241, 262], only implicit consideration of polarization effects in the region of the hydrophilic lipid headgroup [89], or artifacts due to the limited size of the simulation system as compared to experimental setups and the use of periodic boundary conditions [259]. Also, at low ethanol concentrations, the partition coefficient strongly depends on the alcohol concentration [259], rendering high precision experiments in this regime difficult. Due to the too large partition coefficient for ethanol, observed effects are probably amplified with respect to experiments at comparable concentrations [89].

Also for the long-chain 1-alkanols, the partitioning between solvent and membrane was unaffected by the large external pressure. As for normal pressure, all 1-alkanols were located within the bilayer, their hydrocarbon chains being aligned with the phospholipid tail region.

4.3.3 Structural Changes

It has been shown that the simulation of the pure DMPC bilayer at standard pressure (simulation C1, see Table 4.1) reproduces experimental values for the area per lipid, the bilayer thickness, the lipid order parameter, the lipid diffusion, and the bilayer elasticity quantitatively [89]. Also, alkanol-induced changes of these parameters predicted in the simulations were in good agreement with the limited experimental data available [89].

High external pressure had a small to moderate effect on the structural properties of the ethanol-, decanol- and tetradecanol-phospholipid systems. For these membranes, the area per lipid and the bilayer thickness were reduced by 3.5 - 4.7% and 1 - 2% with respect to the systems at 1 bar (see Tables 4.2 and 4.3).

	Without 1-alk-anols (Å^2)	Ethanol (Å^2)	Octanol (Å^2)	Decanol (Å^2)	Tetradecanol (Å^2)
1 bar	64.1 ± 0.4	67.8 ± 0.5	62.5 ± 0.4	59.3 ± 0.1	60.2 ± 0.1
1000 bar	61.2 ± 0.6	64.6 ± 0.5	54.6 ± 0.1	56.6 ± 0.1	58.1 ± 0.1

Table 4.2: Average area per lipid calculated from simulations of a DMPC bilayer containing different 1-alkanols at pressures of 1 bar and of 1000 bar.

	Without 1-alk-anols (Å)	Ethanol (Å)	Octanol (Å)	Decanol (Å)	Tetradecanol (Å)
1 bar	34.6 ± 0.2	34.0 ± 0.2	38.6 ± 0.2	40.5 ± 0.1	41.0 ± 0.1
1000 bar	33.9 ± 0.3	33.3 ± 0.2	40.6 ± 0.1	40.1 ± 0.1	40.6 ± 0.1

Table 4.3: Average headgroup-to-headgroup thickness of a DMPC bilayer containing various 1-alkanols at normal and high external pressures.

The bilayer containing octanol (systems O1/O1000) underwent the largest changes with an area per lipid decrease of 7.9 Å^2 and a thickness increase of 2.0 Å (see also Fig. 4.1).
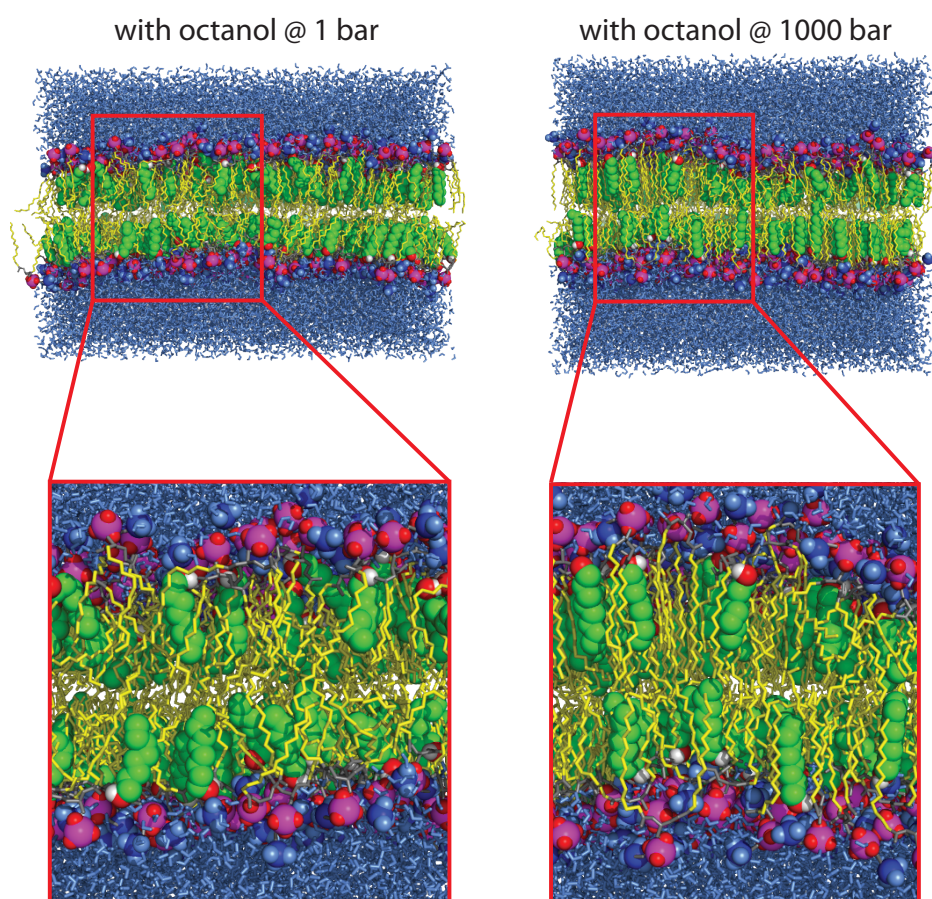

Figure 4.1: Simulation systems containing octanol at 1 bar (snapshot after 33 ns, left side) and at 1000 bar external pressure (70 ns, right side) . The 1-alkanol carbon atoms are represented by green spheres, connected to the hydroxyl group (red and white spheres). Lipid tails are shown as yellow sticks. The lipid headgroup atoms are shown as spheres (phosphorus atoms, magenta; oxygen atoms, red; choline groups, blue) and grey sticks (carbon atoms). The surrounding water is depicted as blue sticks. In the enlarged view, the increased order and the decreased tilt of the lipid chains with respect to the membrane normal can be seen.
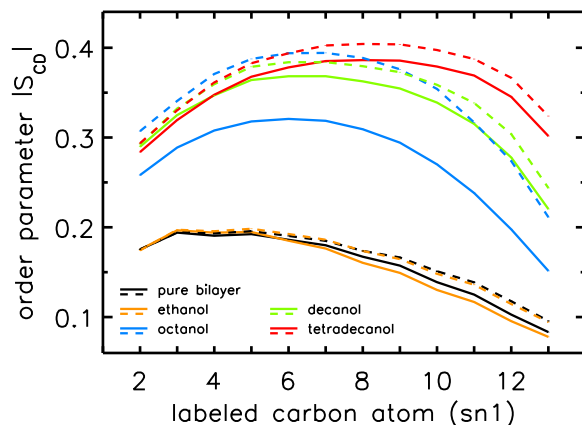
Figure 4.2: Deuterium lipid order parameter (sn1 chain) for simulations with various 1-alkanols at external pressures of $1\,\mathrm{bar}$ (solid lines) and $1000\,\mathrm{bar}$ (dashed lines). Error bars are included, but are too small to be seen.

Application of external pressure exerted an ordering effect on the lipid tails by lateral compression of the bilayer. In agreement with the measurements of, e. g., Reyes Mateo et al. [217], the hydrocarbon chain order, measured by the deuterium lipid order parameter, was enlarged for all systems at $1000\,\mathrm{bar}$ (see Fig. 4.2). This order increase was additionally reflected in the reduction of the fraction of *gauche* dihedrals of the hydrocarbon chains (data not shown). Again, the largest changes induced by high external pressure were found for the octanol systems O1/O1000. The structural rearrangements of the bilayers under pressure were accompanied by an enhanced interdigitation of the lipid – and in the case of decanol and tetradecanol also of the 1-alkanol – chains. This is reflected by an increased density in the core region of the bilayer, exemplarily shown for DMPC in Fig. 4.3.
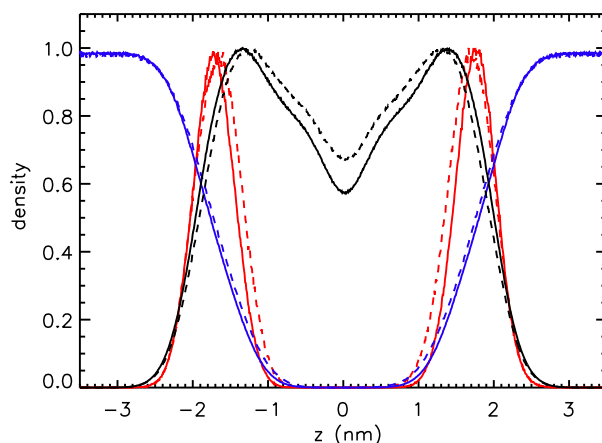
Figure 4.3: Normalized number density profiles across the bilayer for the simulations of the pure DMPC systems (C1, solid lines; C1000, dashed lines). A Gaussian smoothing has been applied. The blue, black, and red lines represent the water, the lipid bilayer, and the phosphorus densities, respectively. Error bars are insignificantly small and are omitted here for clarity. The maxima of the phosphorus density curve mark the approximate headgroup location.

For the pure DMPC bilayer at standard pressure, the majority of the lipid chains were tilted with angles γ ranging from $0°$ to $20°$ with respect to the bilayer normal (Fig. 4.4). The angles α, a measure for the lateral orientation, were homogeneously distributed for pure DMPC bilayers and for the ethanol-DMPC system. Addition of long-chain 1-alkanols to the bilayer decreased the tilting of the lipid chains. For tetradecanol (especially for the upper monolayer), the lateral distribution was narrowed.

High external pressure aligned the lipid tails with the membrane normal in the presence of long-chain 1-alkanols, reflected by a shift of the distribution towards smaller angles γ. The increased order in the octanol-phospholipid system (see Fig. 4.2) is additionally seen in the strong alignment of the hydrocarbon tails (pronounced maximum in the distribution of α for the upper monolayer; Fig. 4.4). The increase in lipid chain order, the increased packing density, and the alignment of the lipid tails for the octanol-DMPC system at high pressure are clearly seen in snapshots of the simulation system, too (Fig. 4.1).
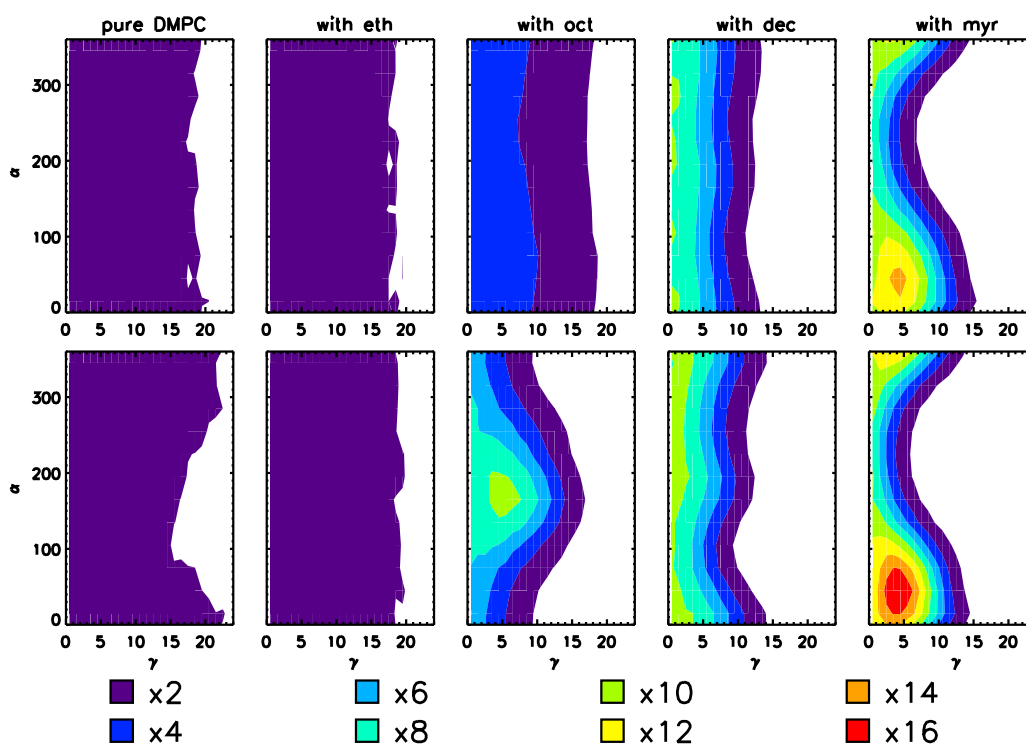
Figure 4.4: Orientation of the lipid chains (upper monolayer) of the different simulations. The chain orientation is given as a function of the angle γ between the lipid chains and the bilayer normal and the angle α defined by the projection of the lipid chains onto the bilayer plane and the arbitrarily chosen vector $(1, 0, 0)$. The top row shows results from the simulations at standard pressure, the bottom row for the high pressure simulations. The color coding is chosen relative to an equal distribution in the angles α and γ. Occupancies with lower than two times this number are colored white, between two and four times this number are colored purple, between four and six times this number dark blue, etc.

4.3.4 Diffusion Coefficient

At standard pressure, lipid diffusion was enhanced in a DMPC bilayer containing ethanol with respect to pure bilayers, whereas it was suppressed in systems containing octanol, decanol, or tetradecanol (see Table 4.4 and the previous study [89]). The diffusion coefficients predicted from the simulations were shown to be in agreement with values found in continuous photobleaching experiments [89]. External pressures of 1000 bar decreased the lipid motion in all systems: for the pure DMPC, the ethanol-, the decanol-, and the tetradecanol-DMPC systems, the lipid diffusion was decreased by a factor of 1.6-2.3. In contrast, for the octanol-DMPC system, a roughly 5-fold decrease in lipid diffusion was observed.

	Without 1-alk-anols ($\frac{\mu m^2}{s}$)	Ethanol ($\frac{\mu m^2}{s}$)	Octanol ($\frac{\mu m^2}{s}$)	Decanol ($\frac{\mu m^2}{s}$)	Tetradecanol ($\frac{\mu m^2}{s}$)
1 bar	11.5 ± 0.6	17.0 ± 0.7	6.6 ± 0.4	2.9 ± 0.1	3.0 ± 0.1
1000 bar	7.1 ± 0.3	7.5 ± 0.3	1.4 ± 0.1	1.7 ± 0.1	1.8 ± 0.2

Table 4.4: Lipid diffusion coefficients for simulations of a DMPC bilayer with various 1-alkanols at a pressure of 1 bar and of 1000 bar.

4.3.5 Pressure Profiles

The symmetrized pressure profiles calculated from the MD simulations of the pure DMPC bilayer at 1 bar and at 1000 bar and the difference between them (for the calculation of the difference pressure profile the bilayer at 1000 bar was scaled to the same thickness as the bilayer at 1 bar) are shown in Fig. 4.5. Results obtained at standard pressure (Fig. 4.5A) are in agreement with previous studies [40, 90, 91, 142, 184, 190, 191, 195, 244, 259]: large tensions, which are due to strong electrostatic interactions and hydrophilic forces minimizing the contact between water and the hydrocarbons, were observed in the region of the glycerol group ($z = \pm 1.44$ nm). At the water-lipid interface ($z \approx \pm 2.2$ nm) a second, slightly smaller tension peak was resolved. This two peak pattern was observed also in the separate contributions of the various interaction groups to the pressure profile (Fig. 4.6). The tension peaks are caused by solvent-lipid interactions forming a hydrogen bonded network. Due to the increased order of interfacial water molecules (see, e. g., Siu et al. [241]), solvent-solvent interactions are repulsive at the interface (Fig.4.6). Pressure maxima resulting from the entropic repulsion of the lipid chains were found in the region of the 5th-7th carbon atom. The vanishing pressure in the bulk water region may be used as a signature of full hydration of the lipid bilayer.

At an external pressure of 1000 bar (see Fig. 4.5B) , the general shape of the curve was maintained, whereas the amplitudes of all local maxima and minima, especially the chain repulsion term, were strongly suppressed leading to a smoothed profile. The tension maxima in the headgroup region are merged and cover the whole headgroup region. Inclusion of 1-alkanols into the bilayer strongly modified the pressure profiles (see
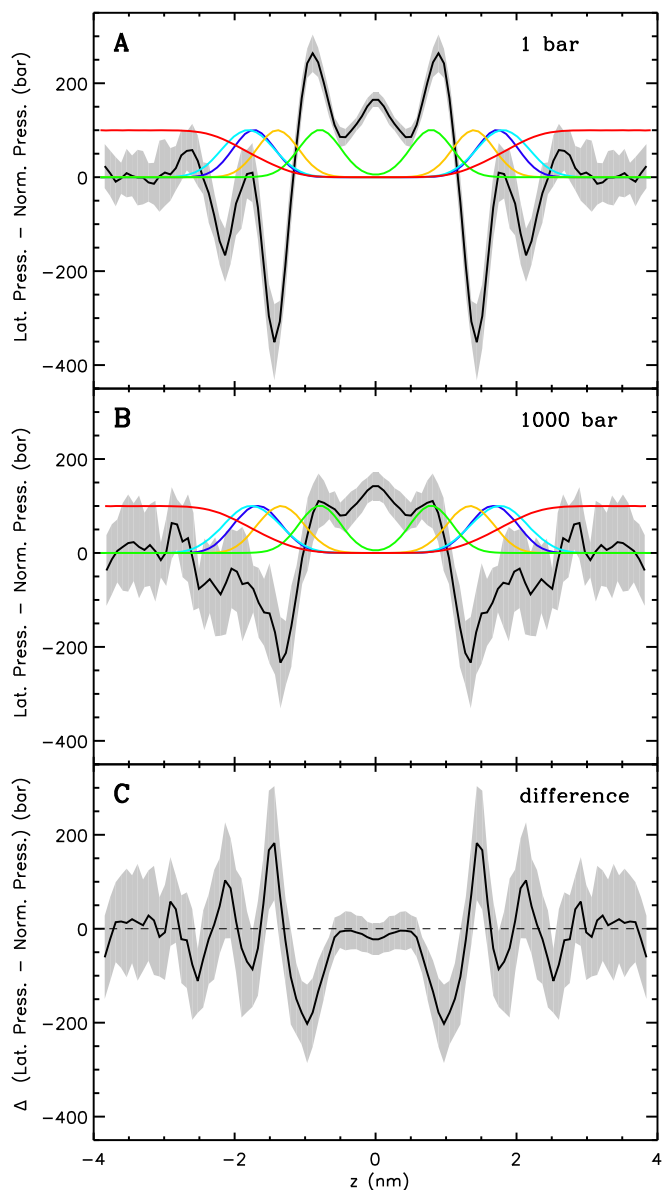
Figure 4.5: Lateral pressure profiles of a DMPC bilayer consisting of 512 lipids at normal pressure (top) and at 1000 bar (middle). The local lateral pressure, i.e., the difference between the lateral and normal components of the pressure tensor, is plotted as a function of the normal coordinate z of the bilayer (solid black line, $z = 0$ at the bilayer center). The error, calculated by averaging over time intervals and using error propagation for the smoothing procedure, is indicated by the grey shaded area. As a reference, the normalized, dimensionless number densities of various lipid components across the bilayer are given (dark blue: phosphorus group, light blue: choline group, yellow: glycerol group, green: 6th and 7th carbon atoms of the lipids, red: water). The bottom panel shows the difference between the pressure profiles at 1000 bar (bilayer at 1000 bar scaled to the thickness of the bilayer at normal pressure) and at 1 bar.

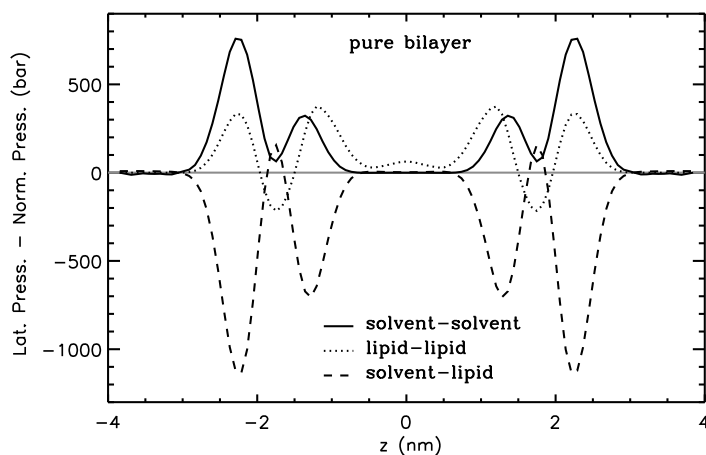Figure 4.6: Contributions of the different interaction groups to the total lateral pressure of the pure lipid bilayer at normal pressure. Errors are comparable to those for the total pressure profile.

Fig. 4.7). Ethanol mainly reduced the magnitude of the chain repulsion terms, which was, however, less pronounced if the GROMACS force field with modified partial charges [151] was used for ethanol (results not shown). This is in agreement with coarse-grained calculations of Frischknecht and Frink [83], whereas Terama et al. [259] found no significant changes at this peak in all-atom simulations using a DPPC bilayer. Both Frischknecht and Frink [83] and Terama et al. [259] reported a pronounced decrease of the interfacial tension upon addition of ethanol, whereas we observed only a slight, insignificant decrease. A splitting of the total pressure into the contributions from the interacting groups (data not shown) showed a decreased solvent-lipid tension at the interface and at the region of the glycerol group, and a peak for alkanol-lipid interactions in the latter region. Therefore it can be concluded that ethanol replaced solvent molecules in the region around the glycerol backbone. The above-mentioned difference in the total pressure profile to the study of Terama et al. [259] is probably due to different force fields used for ethanol and different cutoffs for Coulombic interactions.

Addition of long-chain 1-alkanols amplified the local pressure maxima and minima in the bilayer core. Due to the thickening of the bilayers, the peaks were shifted outwards. Remarkably, a tension peak was now seen within the hydrophobic core. This peak was caused by increased bonded interactions (see Fig. 4.8) from alkanol-alkanol and lipid-lipid interactions (data not shown). These bonded interactions are probably enlarged due to the increased order of the lipids and the 1-alkanols (see also the previous study [89]) (increased number of dihedrals in *trans* conformation). Upon addition of long-chain 1-alkanols, the repulsive Lennard Jones interactions of the lipids and of the 1-alkanols were enhanced (see Fig. 4.8). With ethanol, decanol, and tetradecanol at high pressure, only moderate changes in the total pressure profile were found as compared to the respective pressure profile at 1 bar. The Lennard Jones interactions in the high-pressure systems with decanol or tetradecanol are increased, but this change is compensated for by increased bonded interactions and decreased 1-4 interactions. Drastic changes in the lateral pressure profile were obtained for the octanol-DMPC system at high pressure: the interfacial tension minimum almost vanished, but the first minimum (counted from the center of the bilayer) became much more pronounced.
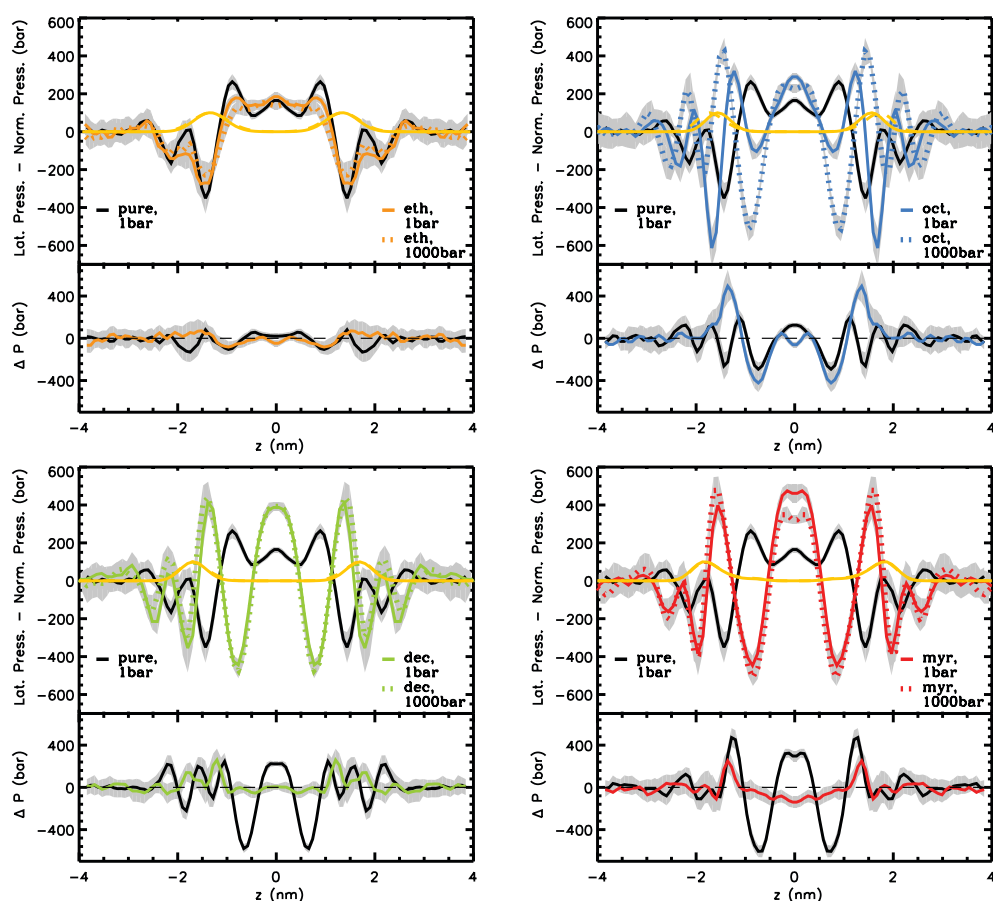
Figure 4.7: Upper section of each panel: Lateral pressure profiles of DMPC bilayers containing various 1-alkanols at external pressures of $1\,\mathrm{bar}$ (colored solid lines) and $1000\,\mathrm{bar}$ (colored dotted lines). For comparison, the lateral pressure profile of a pure DMPC bilayer is drawn (black solid line). Errors are indicated by gray shadows. The normalized dimensionless density of the lipid glycerol group is shown in yellow (solid line: $1\,\mathrm{bar}$, dashed line: $1000\,\mathrm{bar}$; mostly, these two curves overlap). Lower section of each panel: Difference between the lateral pressure profiles with and without 1-alkanols (black line) and the difference of the curves with 1-alkanols at $1000\,\mathrm{bar}$ and $1\,\mathrm{bar}$ (colored lines). For the calculation of the difference-pressure profiles, the contributing terms were scaled to the thickness of the pure bilayer at normal pressure.

4.4 Discussion

4.4.1 Partition Coefficient

One hypothesis explaining the pressure reversal of anesthesia could have been a shift of the bilayer-water partitioning equilibrium of anesthetics such that less anesthetics dissolve in the lipid bilayer. Here, neither in the case of ethanol nor in the case of long-chain 1-alkanols, significant changes of the partition coefficients at a pressure of $1000\,\mathrm{bar}$ were observed. However, due to the large partition coefficients of long-chain 1-alkanols [79, 225, 234], moderate changes in the partition coefficient of these alkanols would hardly
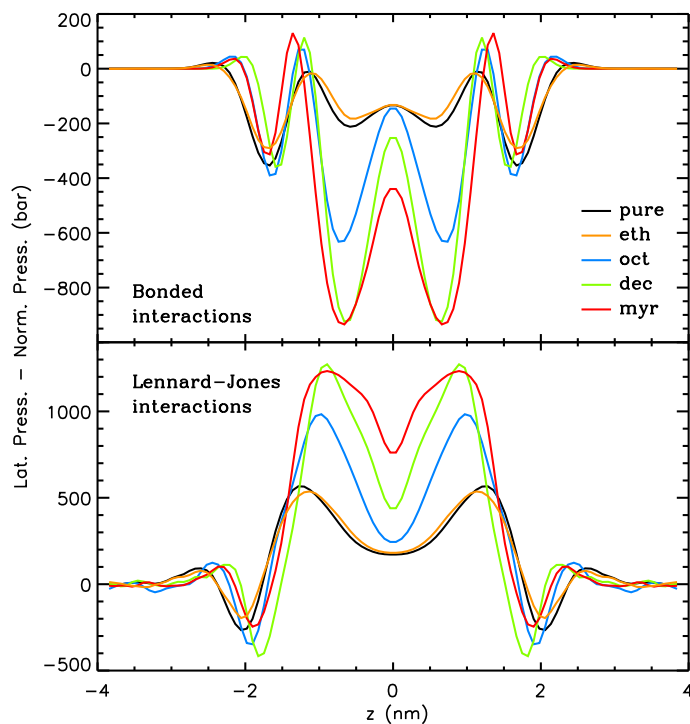
Figure 4.8: Bonded and Lennard Jones contributions to the total lateral pressure profile for all systems at normal pressure. All systems are scaled to the thickness of the pure bilayer at normal pressure. Errors are comparable to those for the total pressure profile.

emerge in MD simulations with their inherent limited system size. Our results are in agreement with a study of Trudell et al. [272], where electron spin resonance techniques were used to investigate the partitioning of TEMPO (2,2,6,6 tetramethylpiperidine-1-oxyl) molecules in phospholipid vesicles. Only a very moderate shift of the distribution of TEMPO molecules between the aqueous and lipid phase, too small to account for the reversal of anesthesia, was found. Therefore, the assumption of reversal of anesthesia by a pressure-driven change of the 1-alkanols' partitioning behavior can be discarded, in agreement with the work by Miller et al. [166], who – based on thermodynamic analyses – showed in 1973 that a pressure-induced shift of partitioning is not able to explain the pressure-dependence of the anesthetic concentration.

4.4.2 Pressure Profiles

The lateral pressure profile of a DMPC bilayer at normal pressure was not only largely modified by the addition of 1-alkanols studied here, but the long-chain 1-alkanols caused even a tension in the bilayer core. The conformational equilibrium of membrane-embedded proteins could easily be shifted by this effect. Therefore, the results presented here lend support to a lipid-mediated mode of anesthetic action via the lateral pressure inside a membrane as suggested by Cantor [33–35].

To illustrate this idea further, we calculated the hypothetical shift in the conformational equilibria of some model proteins [36, 91] upon addition of 1-alkanols using the pressure profiles obtained from the MD simulations. For the notation and calculations, we follow

the work by Cantor [36]: At a given lateral pressure distribution p_0, the conformational equilibrium between conformational states ($s = r, t, \ldots$) of membrane proteins is given by $K_0 = \frac{[t]_0}{[r]_0}$. If the cross-sectional area difference $\Delta A(z) = A_t(z) - A_r(z)$ varies in the direction of the bilayer normal, a change in the lateral pressure profile $p(z)$ results in the change of energy

$$\Delta W = \int_{-h}^{h} \Delta p(z) \Delta A(z)\, dz\,, \tag{4.4}$$

with $\Delta p(z) = p(z) - p_0(z)$ and the thickness h of one monolayer. For $\Delta A(z) = \text{const.}$, it follows that

$$\Delta W = \Delta A(z) \int_{-h}^{h} \Delta p(z)\, dz = \Delta A(z) \left(\int_{-h}^{h} p(z)\, dz - \int_{-h}^{h} p_0(z)\, dz \right) = 0, \tag{4.5}$$

since a self-assembled bilayer is always in a tension-free state [163]. Induced by the change in lateral pressure, a new conformational equilibrium $K = \frac{[t]}{[r]}$ will be established. For the result of the integration (Eq. (4.4)), the definition of the bilayer thickness $d = 2h$ is crucial (see Fig. 4.9), as there exists a large tension at the lipid-water interface. Here, we defined the bilayer thickness by the maxima of the phosphorus density of the pure lipid bilayer at $1\,\text{bar}$ and scaled the bilayers of all other simulations to the thickness of this bilayer. This approximation is reasonable, since lipid membranes in close vicinity of an embedded membrane protein adjust to its central hydrophobic surface. By equating the chemical potentials μ_r and μ_s of the two conformational states at each lateral pressure distribution $p(z)$ and $p_0(z)$, and assuming that $\Delta A(z)$ is independent of $\Delta p(z)$, Cantor deduced the relation $K = K_0\, e^{-\Delta W/(k_B T)} =: K_0\, e^{-\alpha}$, with k_B and T denoting the Boltzmann constant and the temperature, respectively [33–36].

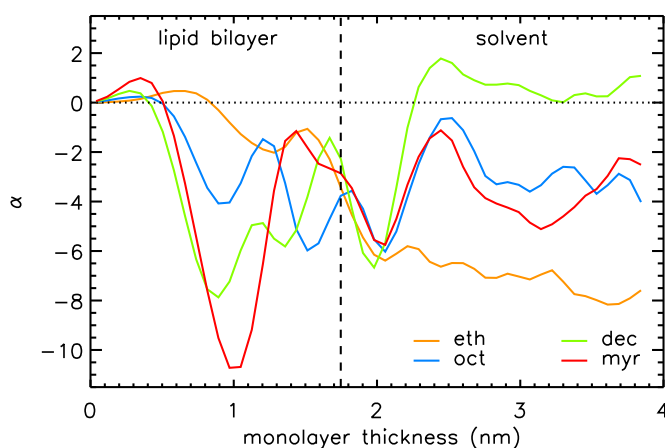Figure 4.9: Values of $\alpha = W/(k_B T)$ (for the comparisons at $1\,\text{bar}$) as a function of the monolayer thickness chosen for the integration (see Eq. (4.4)). The bilayer center is located at $z = 0$. The position of the phosphorus density maximum for the pure bilayer at $1\,\text{bar}$, used as the criterion for the monolayer thickness in our calculations, is marked by the dashed vertical line.

Assuming, as Cantor did [36], an expansion of the cross-sectional protein area in powers of z with different expansion coefficients in the two bilayer leaflets, i.e., $A_s(z) = A_s(0) + a_{1,s}^{\pm}|z| + a_{2,s}^{\pm}z^2 + \dots$ with $a_{j,s}^{\pm} = a_{j,s}^{+}$ for $z > 0$ and $a_{j,s}^{\pm} = a_{j,s}^{-}$ for $z < 0$, and a symmetrical bilayer (i.e., $p(z) = p(-z)$), α can be expressed in terms of the difference of the integral moments of $p(z)$ and $p_0(z)$ [36]

$$\alpha = (k_B T)^{-1} \sum_j \Delta a_j \Delta P_j \qquad (4.6)$$

with $\Delta a_j = \Delta a_j^+ + \Delta a_j^-$, $\Delta a_j^{\pm} = a_{j,t}^{\pm} - a_{j,r}^{\pm}$, and $\Delta P_j = \int_0^h z^j \Delta p(z)\, dz$ for $j \geq 1$. ΔP_0 is zero as the bilayer is always in a tension-free state [163]. The first two integral moments of the DMPC bilayer at $1\,\text{bar}$, calculated from our pressure profiles, are $P_1/(k_B T) = (-0.11 \pm 0.04)\,\text{Å}^{-1}$ and $P_2/(k_B T) = -3.26 \pm 0.78$. Using a statistical thermodynamic lattice model for bilayers, Cantor [36] derived values for $P_1/(k_B T) = -1.74\,\text{Å}^{-1}$ and $P_2/(k_B T) = -29.4$, about an order of magnitude smaller than the respective moments from the MD simulations. The differences probably arise from the simplified model and the neglected headgroup repulsion in the calculations of Cantor [36].

Three models for different membrane proteins have been suggested [36, 91]: The *cooperative tilt* model [36] describes a helix bundle, that is twisted along the bilayer normal (in opposite directions for the two monolayers). In the *bent helix* model [36], a membrane protein is built up by kinked helices forming a non-uniform bundle that can be inscribed by one truncated cone per monolayer. The cross-sectional area of such a membrane protein is $A_s(z) = \pi \left(\xi_s(0) + |z| \tan(\phi) \right)^2$, with the radius of the helix bundle $\xi_s(0)$ and the angle $\phi = \phi^{\pm}$ between the cone-shaped envelope of the kinked helix bundle at the upper/lower monolayer and the bilayer normal (for a more detailed description see [36]). The mechanosensitive channel MscL was approximated by a truncated cone stretching over the whole bilayer (*conical shape model* [91]). Different protein conformations are given by different slopes.

Using the results for the lateral pressure profiles from our simulations, we calculated the exponent α, characterizing the shift between two conformations of a protein, for these three protein models. As for the parameters of these models, we used values that were previously suggested from the respective authors: $\tan^2(\theta_t) - \tan^2(\theta_r) = 0.05$ for the cooperative tilt model ([36], corrected), with the twist angle θ_s of the respective conformation, a change of the cone slope from 0.0 to 0.2 for the MscL model of Gullingsrud and Schulten [91], and angles $\phi_r^+ = \phi_r^- = 0°$ and $\phi_t^+ = \phi_t^- = 6°$ between the bilayer normal and the envelope of the kinked helices (assuming a symmetrical protein) for the bent helix model [36]. A change in the conformational equilibria was considered as significant, if K and K_0 differed by at least a factor of 2, i.e., if $|\alpha| \geq \ln(2) \approx 0.69$.

According to this definition, we found no significant changes in the protein conformational equilibrium upon addition of 1-alkanols or application of external pressure for the cooperative tilt and the conical shape model. However, assuming a bent helix model, the computed lateral pressure profiles for 1-alkanols and external pressure exert opposing effects on the conformational equilibrium of a hypothetical membrane protein, in line with the anesthetic action of 1-alkanols and the reversal of the anesthetic effect by external pressure (see Table 4.5): for addition of 1-alkanols at normal pressure, α was negative for all four investigated 1-alkanols.

System	Reference system	$\Delta P_1/(k_B T)$ (Å^{-1})	$\Delta P_2/(k_B T)$	α	Significance
E1	C1	-0.125 ± 0.053	-1.803 ± 0.794	-3.43 ± 1.39	yes
O1	C1	-0.140 ± 0.060	-1.048 ± 0.898	-3.77 ± 1.60	yes
D1	C1	-0.088 ± 0.059	0.673 ± 0.853	-2.27 ± 1.56	yes
TD1	C1	-0.109 ± 0.067	0.246 ± 1.017	-2.86 ± 1.77	yes
C1000	C1	-0.112 ± 0.059	-0.771 ± 0.860	-3.02 ± 1.57	yes
E1000	E1	0.011 ± 0.054	0.690 ± 0.828	0.33 ± 1.44	no
O1000	O1	0.293 ± 0.072	5.983 ± 1.077	8.16 ± 1.91	yes
D1000	D1	0.225 ± 0.068	3.357 ± 0.976	6.17 ± 1.81	yes
TD1000	TD1	0.041 ± 0.075	0.958 ± 1.139	1.16 ± 1.99	no

Table 4.5: Changes in the first and second integral moments upon the transition from $p_0(z)$ (reference system) to $p(z)$ and corresponding changes in the conformational equilibrium of bent helix model proteins, measured by α. The error was calculated by error propagation.

The decreasing difference (within error margins) in the moments ΔP_1 and ΔP_2 for longer hydrocarbon chains of the 1-alkanols correlates with the cutoff effect for anesthetics, i. e., 1-alkanols with a chain length of 12 carbons or more do not show any anesthetic potency (see, e. g., Pringle et al. [206]). However, the cutoff is probably dependent on the membrane composition. Application of external pressure resulted - except for the control simulation - in positive values of α, and thus a reversal of the effect of 1-alkanols on the distribution of states, significant only for simulations containing octanol and decanol. The computed pressure-induced shift in the conformational equilibrium of a hypothetical protein in a pure lipid bilayer (negative α) correlates with the experimentally observed "pressure paralysis" [93].

Thus, – although the application of external pressure did not reverse the alkanol-induced changes in the lateral pressure profile – a pressure-reversal mechanism of anesthesia for the bent helix model is seen: 1-alkanols moved the protein conformational equilibrium in one direction, whereas external pressure changed the equilibrium in the opposite direction. However, this pressure-reversal mechanism crucially depends on the type of change in protein shape upon activation or deactivation. Therefore, simulations of lipid bilayers containing explicit membrane proteins and eventually also different lipid species and cholesterol will be necessary.

4.4.3 Phase Behavior

A different mechanism for anesthesia relies on shifts in the membrane phase transition temperatures by anesthetics [101]. Depending on thermodynamic parameters such as temperature and pressure, lipid bilayers exist in different phases. Upon heating, pure DMPC bilayers at standard pressure exhibit a so-called pretransition from a gel to a ripple phase

at $14°\,C$ and a main transition from a ripple to a liquid-disordered phase at $24°\,C$ (see, e. g., [97, 113, 299]). By application of external pressure, further distinct phases can be induced [64]; for example, for saturated phosphatidylcholine bilayers with chain lengths of 13 to 18 carbon atoms, a pressure-induced interdigitated phase has been found [112].

Phase transitions of lipid bilayers have been observed successfully in dissipative particle dynamics simulations [132–134], as well as in coarse-grained and atomistic molecular dynamics simulations [56, 138, 162, 245]. In (MD) simulations, indications for phase transitions are drastic changes in the area per lipid, the bilayer thickness, the lipid chain order, and the lipid diffusion [138]. Besides, the tilt angle of the lipid chains with respect to the membrane normal varies: in the gel L_β and in the ripple $P_{\beta'}$ phase, the lipid chains are tilted, whereas in the pressure-induced, partially interdigitated gel phase $L_{\beta i}$, they are aligned parallel to the bilayer normal. In the liquid crystalline phase L_α, the lipid chains are disordered (see Eisenblätter and Winter [64]).

In our simulations, we did not observe any signature for a phase transition of the pure DMPC bilayer and the bilayer with ethanol at $1000\,bar$. However, large structural changes were observed for the DMPC bilayer with octanol at high external pressure. Especially, the alignment of the lipid chains to the bilayer normal, the enhanced interdigitation, and the strong shrinking of the area per lipid indicate a transition to the partially interdigitated gel phase $L_{\beta i}$. Our previous simulations of DMPC bilayers with decanol and tetradecanol at $1\,bar$ showed a drastic decrease in the area per lipid and an increase in the lipid order parameter. These systems probably underwent phase transitions to the gel state already at normal pressure. Therefore, for these systems, only moderate pressure-induced structural changes were found.

These results are in line with previous experiments: In accordance with the Clausius-Clapeyron relationship, Ichimori et al. [112] measured a linear increase of the gel to liquid-crystalline phase transition temperature with a slope of $21.2\,K/kbar$. At high pressures above $3\,kbar$, a partially interdigitated gel phase was observed. At normal pressure, addition of 1-alkanols up to the chain length of octanol caused a lowering of the main gel to liquid-crystalline phase transition temperature [89, 137], depending linearly on the alkanol concentration (experiments with DPPC vesicle membranes) [252]. Long-chain 1-alkanols from decanol up to tetradecanol exerted a biphasic dose-response effect on DPPC vesicles: at low concentrations they depressed, but at higher concentrations they elevated the phase transition temperature [120]. Additional external pressure increased the phase transition temperatures with all 1-alkanols [252].

Since no phase transition was observed for pure DMPC at $1\,kbar$ in the simulations, we conclude that in simulations, the main phase transition temperature for DMPC at normal pressure is significantly lower than obtained from experiment. Similarly decreased transition temperatures were found before for DPPC and DPPE bilayers applying a similar force field [138].

4.5 Summary and Conclusions

The influence of a large external pressure and of 1-alkanols of different chain-lengths on the lateral pressure profile of a DMPC bilayer has been evaluated. Similar to the effect of a

large external pressure on a pure bilayer, ethanol smoothed out the lateral pressure profile as compared to the profile of the pure bilayer. Long-chain 1-alkanols amplified local maxima and minima in such a way that a tension was created within the bilayer core. Except for the simulation with octanol, the pressure profiles for bilayers containing 1-alkanols were only moderately changed by a pressure of 1000 bar. External pressure slightly decreased both the area per lipid and, except for the simulation with octanol, the bilayer thickness. Lipid diffusion was strongly suppressed and an enhanced interdigitation of the lipid chains – for decanol and tetradecanol also of the 1-alkanol chains – was observed. At normal pressure, addition of long-chain 1-alkanols caused an alignment of the lipid chains in the direction of the bilayer normal. This effect was amplified by the application of an external pressure. For the octanol-DMPC system, external pressure probably caused a phase transition to the pressure-induced, partially interdigitated $L_{\beta i}$ gel phase.

For the bent helix model of membrane proteins [36], changes in the lateral pressure profile caused by 1-alkanols and additional external pressure were found to shift the equilibrium between different protein conformations in opposite directions, consistent with an anesthetic effect of the 1-alkanols and the pressure reversal of anesthesia. Our results lend support to Cantor's model that anesthesia is mediated by local pressure changes. In this context, more complex simulations including various lipid species and in particular membrane proteins would be of interest, focusing on the effect of different anesthetics and external pressure on shifts in the main phase transition temperature and on their influence on embedded proteins.

4.6 Acknowledgment

4.7 Addendum: Simulations at Intermediate Pressures

Within this study, also simulations at intermediate pressures of 50, 100, and $200\,\mathrm{bar}$ have been performed. The results of these simulations are similar to what was presented before and will therefore not be discussed here in detail. However, one notable result should be pointed out: the difference of the first integral moments $\Delta P_1 = \int_0^h z\,(p(z) - p_0(z))\,dz$ (compare to Section 4.4.2) did not increase – as one might have expected – linearly with pressure, but large values of ΔP_1 were already found at pressures of 50 and $200\,\mathrm{bar}$ (Fig. 4.10). Therefore, the necessary change in the first integral moment for pressure reversal of anesthesia can already be observed at lower pressures in the simulations.
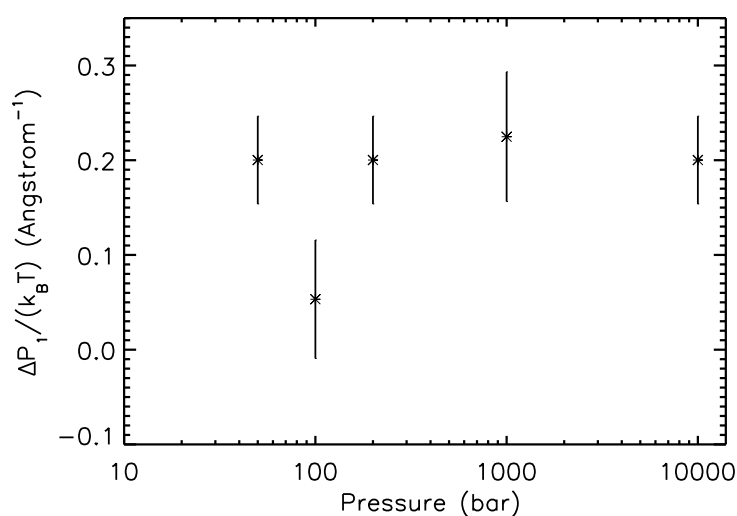

Figure 4.10: Difference of the first integral moments, ΔP_1, for different external pressures with respect to the simulation at normal pressure.

5 Influence of Anesthetics on a Membrane Ion Channel Studied by Molecular Dynamics Simulations

Beate Griepernau [1]   *and Rainer A. Böckmann* [1]

Although anesthesia is widely used in clinical applications, the underlying molecular mechanisms are not yet known. It is generally assumed that anesthetics act by either binding specifically to membrane proteins, or by changing the properties of biological membranes involved in signal transduction, thereby affecting the function of embedded proteins indirectly. Here, the influence of some anesthetics, namely of various 1-alkanols, on a gramicidin–membrane system has been investigated using long-term molecular dynamics simulations. We found a strong decrease of drug adsorption close to the embedded gramicidin. In agreement with lipid-mediated theories, the drug molecules influence both the structure and dynamics of the ion channel by modulating the properties of the surrounding lipid environment. Ethanol decreased the pore radius coupled to an increase in protein fluctuations, whereas decanol increased the pore radius.

[1]Theoretical and Computational Membrane Biology, Center for Bioinformatics Saar, Saarland University, PO Box 15 11 50, 66041 Saarbrücken, Germany

5.1 Introduction

During the last decades there has been a very active discussion concerning the molecular basics underlying anesthesia (see, e.g., [275]). Three classes of theories for anesthesia can be distinguished: the protein-binding models, suggesting the direct binding of anesthetics to protein receptors or ion channels, the models of Miller [167] and Pauling [197], proposing anesthetic-induced clathrate formation in cell fluids, and the lipid(-mediated) theories, assuming an unspecific change of biological membrane properties by anesthetics and probable consequences on membrane proteins. In the latter theories, especially the interplay between membrane lipids and membrane proteins is emphasized. Two recent examples of lipid(-mediated) models for anesthetic action are the theories by Cantor [33–35] and by Heimburg and Jackson [100, 101]. Cantor proposed an influence of the internal lateral membrane pressure on the equilibrium between different protein conformations. Changes of the lateral pressure induced by the integration of anesthetics into biological membranes could then modulate ion currents through membranes. Heimburg and Jackson suggested a completely new model describing nerve pulse propagation by soliton migration along neurons [99], and concluded that a melting point depression of the membrane caused by anesthetics would impede signal transduction and thereby cause anesthesia.

The microscopic action of anesthetics on proteins and lipid bilayers has been investigated in a couple of molecular dynamics (MD) simulation studies: Specific interactions of the volatile anesthetic halothane with four-helix bundles [51, 52], with subunits of the nicotinic acetylcholine receptor [288], and with ketosteroid isomerase [305] were reported. Effects of halothane on the protein dynamics could be inferred from simulations of gramicidin [257] and a potassium channel [287]. Remarkably, the latter study reported different effects of halothane on the global dynamics of the open and closed conformation of the ion channel. Based on these simulations, the authors suggested a preferential binding of anesthetic molecules to the cavity available for the open conformation [287]. The anesthetic molecules halothane or ethanol were preferentially found in the hydrophilic lipid headgroup region of the membrane or at the lipid-water interface [88, 89, 131, 196, 259, 273, 288] and were shown to decrease the number of protein-lipid contacts (halothane [288]). Both of these small anesthetics decreased the lipid order and thereby increased the fluidity of the lipid bilayer.

In order to gain further insight into the microscopic processes causing anesthesia, we have previously investigated the influence of some anesthetic molecules of varying size, namely of various 1-alkanols, on the properties of a phospholipid bilayer (as an approximation for biological membranes) by long-time atomistic MD simulations [88, 89]. The simulations were performed at normal and enlarged external pressure to elucidate also the experimentally demonstrated pressure reversal of anesthesia, i.e., the effect that anesthesia in animals can be reversed by external pressures between 70 and $350\,\mathrm{bar}$ [93, 115, 116, 139, 166]. In the present study, these previous investigations are complemented by introducing a simple ion channel, the gramidicin A, into the membrane. The antibiotic gramicidin A, produced by the soil bacterium *Bacillus brevis*, forms a transmembrane, cation-specific ion channel. This channel is built up by two monomers, each consisting of 15 alternating D- and L-amino acids. Except for four amphiphilic tryptophan residues, the amino acid sequence (HCO - LVal - Gly - LAla - DLeu - LAla - DVal - LVal - DVal - LTrp - DLeu - LTrp - DLeu - LTrp - DLeu - LTrp - NHCH$_2$CH$_2$OH) is hydrophobic. Depending on

the environmental conditions and the solvent history, gramicidin A mainly exists in two different conformations: a single-stranded head-to-head helical dimer (Fig. 5.1), with the C-termini located at the bilayer interface and the N-termini buried in the bilayer interior, and a double-stranded intertwined double helical dimer. Although recent results gave evidence that the energy barrier to potassium passage is decreased for the intertwined double helix with respect to the head-to-head helical dimer [240], here the latter conformation has been chosen for the simulations, as this is widely assumed to be the stable (single channel lifetime of the order of seconds) and channel-forming conformation in lipid bilayers (see reviews [46, 123, 128, 223, 301]). Gramicidin A has been used as a simple model for larger membrane proteins in many studies [46, 123, 128, 223, 301], as it is small (important for the feasibility of simulations), easily accessible, and its structure was resolved very early both by NMR spectroscopy [7, 125, 126] and X-ray measurements [32]. Despite its smallness, simplicity, and the unusual alternating sequence of D- and L-amino acids, which results in a β-sheet like structure of the helices, gramicidin A nevertheless exhibits many important structural features of more complex ion channels [123] and displays also characteristic channel behavior like ion selectivity, subconductance states, blocking, and modulation of channel properties by the lipid environment [301].

During the last years, several experimental and simulation studies trying to identify the molecular targets of anesthetics by investigating the influence of selected anesthetics and nonanesthetics on gramicidin A have been reported by P. Tang and co-workers [145, 253–257, 303]. With the term 'nonanesthetics' the authors referred to molecules, which have a similar structure as some anesthetics and should be anesthetics according to the Meyer-Overton rule (the correlation of anesthetic potency with lipophilicity), but do not have anesthetic potency. The results of these studies emphasized the importance of the interfacial location of anesthetics in contrast to nonanesthetics, that resided mainly in the bilayer core [303]. Though the anesthetics halothane and 1-chloro-1,2,2-trifluorocyclobutane (F3), and the nonanesthetic 1,2-dichlorohexafluorocyclobutane (F6) were found to induce only minor structural changes on gramicidin A [255–257], specific interactions of the anesthetics with the tryptophan residues were repeatedly reported using different measurement techniques [39, 253–256, 303]. Also, the sodium transport in gramicidin A was found to be enhanced by addition of the anesthetic F3, but to be unaffected by the addition of the nonanesthetic F6 [254]. In MD simulations, an influence of the anesthetic halothane, but not of the nonanesthetic hexafluoroethane on the channel dynamics of gramicidin A was observed [145, 257].

Here, we report the effects of changes in the lipid environment, induced by the addition of 1-alkanols of varying chain length and by external pressure, on a gramicidin A dimer embedded in a phospholipid bilayer. We investigated the unbiased partitioning of the 1-alkanols with respect to the ion channel, the thickness adjustment of the bilayer to the peptide dimer, changes in the structure, dynamics, and the pore radius of gramicidin, and the lateral pressure profiles of the peptide-lipid-alkanol systems.

5.2 Methods

5.2.1 Molecular Dynamics Simulations

MD simulations of the gramicidin A (head-to-head helical dimer conformation; protein data bank entry 1MAG [127], see Fig. 5.1) embedded in a lipid bilayer have been performed using the GROMACS [18, 143, 278] software package version 3.3. The bilayer
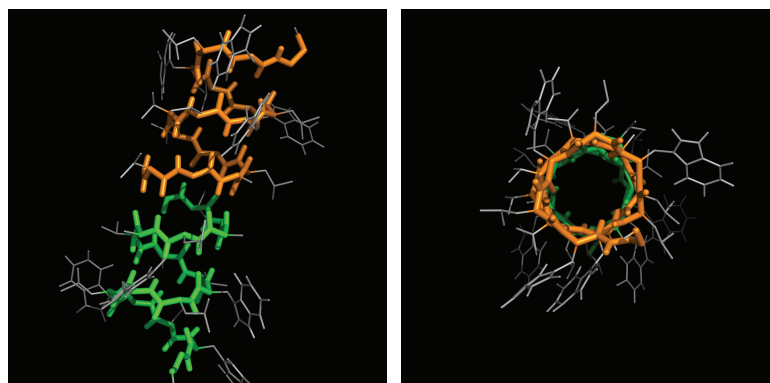

Figure 5.1: Side view and top view of the head-to-head helical dimer conformation of gramicidin A (protein data bank entry 1MAG [127]). The backbones of the two monomers are colored in orange and green, respectively. Side chains are represented by grey lines.

was hydrated by a solution of 1-alkanols and water. A pre-equilibrated peptide-bilayer system was taken from a previous study [240]. Each system consisted of 124 DMPC lipids, one gramicidin A dimer, a minimum of $\approx 5,900$ water molecules (corresponding to > 47 water molecules per lipid), and 72 1-alkanol molecules (ethanol, octanol, or decanol), that had been placed in the water phase at random positions (see Table 5.1 and Fig. 5.2). For all systems, simulations were carried out at external pressures of $1\,\mathrm{bar}$ and $600\,\mathrm{bar}$. Additionally, control simulations without 1-alkanols were performed. Each simulation was run for $100\,\mathrm{ns}$. With regard to its long equilibration time, the simulation with decanol at normal pressure was extended to $140\,\mathrm{ns}$. Equilibrated snapshots of the $1\,\mathrm{bar}$ simulations were taken as starting structures for the simulations at $600\,\mathrm{bar}$.

For all simulations, periodic boundary conditions, a rectangular simulation box, and a constant number of atoms at constant pressure and temperature $T = 310\,\mathrm{K}$ were used (NPT like ensemble). The lipids, the water-alkanol solution, and the peptide were separately coupled to a heat bath [16] with a coupling constant of $0.1\,\mathrm{ps}$. Pressure was kept constant by a weak semi-isotropic coupling to a pressure bath [16] with a time constant of $1\,\mathrm{ps}$ and a compressibility of $4.5 \times 10^{-5}\,\mathrm{bar}^{-1}$.

The force field of Berger et al. [20] and Chiu et al. [45] was applied for the lipids, and combined with the GROMOS96 53A6 force field [193] for the gramicidin (see also Siu and Böckmann [240]). For water, the SPC model [17] was chosen. Bond lengths were constrained by the LINCS [106] and SETTLE [169] algorithms and an integration step size of 2 fs was used.

The long-range electrostatic interactions were treated by the Particle Mesh Ewald (PME) method [50] applying a Fourier grid spacing of $0.12\,\text{nm}$, a 4th order cubic interpolation and a relative accuracy of 1.0×10^{-5}. The short-range van der Waals interactions were truncated at a cutoff radius of $1\,\text{nm}$.
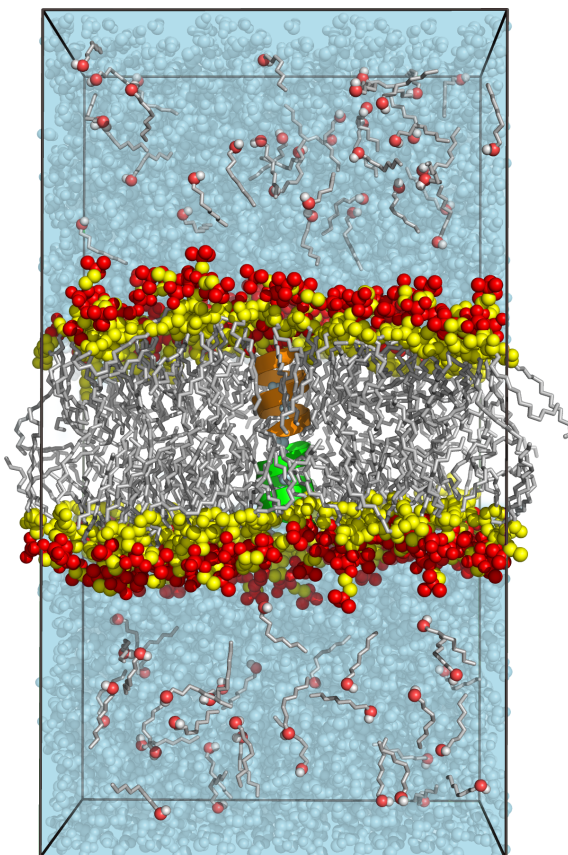
Figure 5.2: Starting structure with gramicidin A embedded in a lipid bilayer and surrounded by an octanol-water solution. The protein is drawn in cartoon-representation with the two helical dimers colored in orange and green. The lipid headgroups are represented by red (atoms of the phosphate and choline groups) and yellow (glycerol moiety) spheres, the lipid and octanol hydrocarbon tails by grey sticks, and the hydroxyl group of octanol by red and white spheres. Water is colored light blue.

system name	number and type of 1-alkanol molecules	number of water molecules	pressure (bar)	equilibration time (ns)
C1	none	6142	1	0
C600	none	6142	600	10
E1	72 ethanol	5892	1	20
E600	72 ethanol	5892	600	25
O	72 octanol	7154	1	25
O600	72 octanol	7154	600	10
D1	72 decanol	7280	1	80
D600	72 decanol	7280	600	15

Table 5.1: All simulated systems containing various 1-alkanols and one head-to-head helical dimer of gramicidin A. All analysis was done with respect to the given equilibration times.

5.2.2 Analysis

The partition coefficient K_p was calculated as the ratio of the mole fraction of 1-alkanols inside the bilayer and the mole fraction of 1-alkanols in the water. The criterion for inside/outside the bilayer was based on the comparison of the z-coordinates of the center of mass of the lipid headgroups (shifted by $0.2\,\mathrm{nm}$ to the bulk water phase) and of the 1-alkanols [88, 89]. The given error is the standard deviation of the partition coefficient obtained by block averaging ($5\,\mathrm{ns}$ windows).

The bilayer's headgroup-to-headgroup thickness was computed by using a grid in the x–y plane (lateral membrane plane) with grid spacing $g \sim 2\,\text{Å}$. Separately for each monolayer, the 'height' at each lattice point was assigned by summing the center of mass coordinates of all lipid headgroups at each time step – weighted by a normalized, distance-dependent Gaussian function with width $\sigma = 0.8g$. The 'height' difference at each grid point between the monolayers was taken as the local membrane thickness.

The pore radius of gramicidin was calculated using the program suite 'Hole' [243]. This package determines the radius of the pore at each position along the channel axis by finding the largest sphere that can be inscribed into the channel without overlapping with any channel atom.

The lateral pressure profile of the system, defined as $p_N - p_L = p_{zz} - (p_{xx} + p_{yy})/2$ (lipid bilayer in the x–y plane, $p_{\alpha,\beta}$ [$\{\alpha, \beta\} \in \{x, y, z\}$] is the microscopic pressure tensor of the system, and p_N and p_L denote the normal and lateral pressure, respectively), was calculated from reruns of the original trajectories using a modified version of GROMACS 3.0.2 provided by Lindahl and Edholm [142]. In these reruns, the constraint algorithm SHAKE [227] and a cutoff of $3.0\,\mathrm{nm}$ for the electrostatic interactions were used. The latter is justified, as reruns truncating electrostatic interactions have been shown to converge to the correct results obtained by Ewald summation, as long as the cutoff is chosen large enough [244] (r_{cutoff} at the order of 1.6 to $2.0\,\mathrm{nm}$). For details of the calculation of the pressure tensor please refer to the article by Lindahl et al. [142] and our previous study [88]. The simulation box was discretized into 100 horizontal slabs of approximately $1\,\text{Å}$ thickness in the direction of the bilayer normal (z-coordinate). For each bin, the difference of the normal and lateral pressure were calculated every 100 ps. The values were then averaged over time and a Gaussian smoothing (width $\sigma \approx 1\,\text{Å}$) over neighboring bins was performed.

5.3 Results

5.3.1 Equilibration Times

The systems were assumed to be in equilibrium for converged partition coefficients and areas of the simulation box. The respective equilibration times are listed in Table 5.1. All further analysis was done with respect to these equilibration times.

5.3.2 Distribution of 1-Alkanols

Due to their amphiphilic nature, the 1-alkanols spontaneously moved into the bilayer and oriented with their polar hydroxyl groups in the hydrophilic headgroup region of the membrane and with their hydrophobic hydrocarbon chains stretched into the hydrophobic membrane core (compare also [88, 89]). For the simulations with ethanol, the 1-alkanol molecules distributed homogeneously between the two leaflets and the partition coefficients at $1\,\mathrm{bar}$ and at $600\,\mathrm{bar}$ were similar with $K_p = 56 \pm 6$ and $K_p = 55 \pm 7$, respectively. In the case of the long-chain 1-alkanols octanol and decanol, all 1-alkanols moved into the lipid bilayer within the equilibration time. In contrast to ethanol, clustering of octanol and decanol inside the water phase prior to insertion resulted in an asymmetrical distribution of these molecules between the upper and lower monolayer (30:42 for octanol and 22:50 for decanol).

As previously reported and discussed [88, 89, 196, 259], the ethanol partition coefficient is too large as compared to experiments [89, 130, 224, 259, 268, 269] and therefore the observed effects are probably amplified with respect to experiments at comparable concentrations. For the long-chain 1-alkanols, the full partitioning of the 1-alkanols into the bilayer agrees well with the large partition coefficients determined in various experimental studies [79, 225, 234].

For all investigated 1-alkanols, the area density of the 1-alkanols in the lipid bilayer varied with the distance to the embedded peptide (Fig. 5.3). Close to the gramicidin, only very few 1-alkanol molecules were found, whereas further apart the number of 1-alkanols per unit area increased. For ethanol this increase was moderate, while it was more pro-
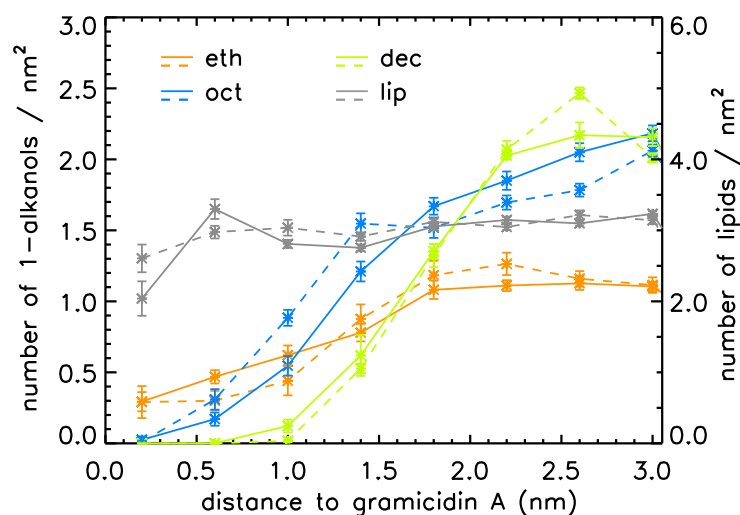
Figure 5.3: Area density of 1-alkanol molecules (blue, green, and orange lines; left ordinate) in the membrane plane as a function of the distance to the center of mass of gramicidin. Results at $1\,\mathrm{bar}$ ($600\,\mathrm{bar}$) are represented by solid (dashed) lines. For comparison, also the lipid area density of the gramicidin-phospholipid system without 1-alkanols is given (grey lines; right ordinate). Please note the differently scaled axes of ordinates for the 1-alkanol and the lipid area densities.

nounced for the long-chain 1-alkanols. The onset of the increase for decanol occurred at larger distances to the peptide than for octanol. Differences in the integrated area densities (from Fig. 5.3, not shown), i. e., the number of molecules solved in the membrane, are due to differences in the partition coefficients for ethanol and the long-chain 1-alkanols. Also the lateral size of the simulation systems varied slightly, as it was free to adjust to its equilibrium value (NPT like ensemble, see *Methods* section). For the simulations with octanol and decanol at $600 \, \mathrm{bar}$, this area was decreased from $44.66 \pm 0.10 \, \mathrm{nm}^2$ (octanol, $1 \, \mathrm{bar}$) to $40.92 \pm 0.13 \, \mathrm{nm}^2$ (octanol, $600 \, \mathrm{bar}$) and from $42.16 \pm 0.15 \, \mathrm{nm}^2$ (decanol, $1 \, \mathrm{bar}$) to $38.58 \pm 0.03 \, \mathrm{nm}^2$ (decanol, $600 \, \mathrm{bar}$).

For all simulations, the bilayer thickness (for the definition see *Methods* section) close to the gramicidin is decreased from the average value, i. e., the lipid bilayer adjusted to the dimensions of the gramicidin A (Fig. 5.4). This is in agreement with previous ob-
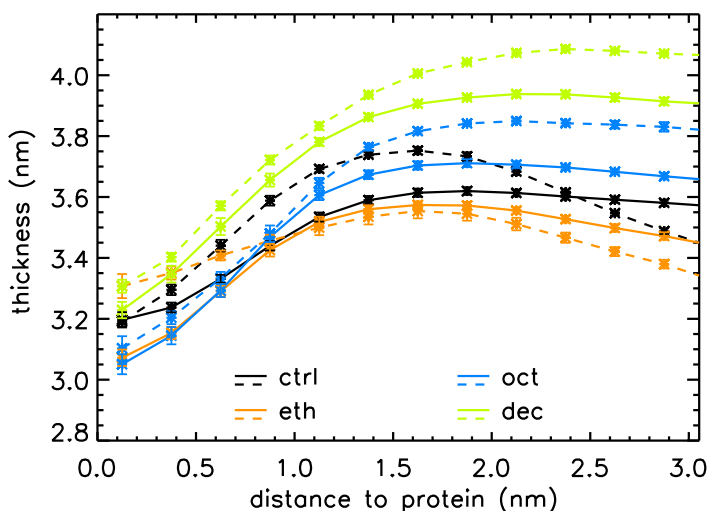

Figure 5.4: Bilayer thickness as a function of the distance (in the bilayer plane) to the center of mass of gramicidin. Results at $1 \, \mathrm{bar}$ ($600 \, \mathrm{bar}$) are represented by solid (dashed) lines. Error bars are included, but are very small and therefore hardly visible.

servations for gramicidin [239] and other proteins and peptides; for a review see, e. g., [114]. Close to the ion channel, the thickness of the bilayer ranged from about $3.0 \, \mathrm{nm}$ to $3.3 \, \mathrm{nm}$. For larger distances from the gramicidin, the membrane thickness increased to $3.4 - 4.1 \, \mathrm{nm}$.

The average bilayer thickness (taken over the whole simulation box) of the pure DMPC bilayer with gramicidin A at normal pressure was increased as compared to values obtained for pure phospholipid systems (see [88, 89]). Nevertheless, the overall trends upon addition of 1-alkanols (see Table 5.2) are in agreement with these previous simulations [88, 89]: at normal pressure, the thickness was increased by addition of long-chain 1-alkanols and decreased by ethanol. Additional external pressure had opposite effects on the different systems: in the simulations of the pure gramicidin-DMPC system and with added ethanol, large pressure led to a decrease of the average bilayer thickness, whereas it increased the average bilayer thickness in the simulations with octanol or decanol.

	Without 1-alkanols (nm)	Ethanol (nm)	Octanol (nm)	Decanol (nm)
1 bar	3.56 ± 0.01	3.44 ± 0.01	3.66 ± 0.01	3.87 ± 0.01
600 bar	3.51 ± 0.02	3.33 ± 0.04	3.81 ± 0.03	4.00 ± 0.01

Table 5.2: Average bilayer thickness.

5.3.3 Influence of 1-Alkanols on the Structure and Dynamics of Gramicidin A

The addition of 1-alkanols had only a minor influence on the overall structure of gramicidin A. The root mean square deviation (RMSD) of the total dimer was below $0.23\,\mathrm{nm}$ for all simulations at normal and enlarged pressures (data not shown). The observed stability of gramicidin is in agreement with studies of Tang et al. [255–257], who investigated the effects of the anesthetics halothane and F3 on gramicidin.

Also the dynamics of the peptide was hardly affected by the addition of 1-alkanols (Fig. 5.5). Only with ethanol, the fluctuations of the channel were significantly enhanced, prob-
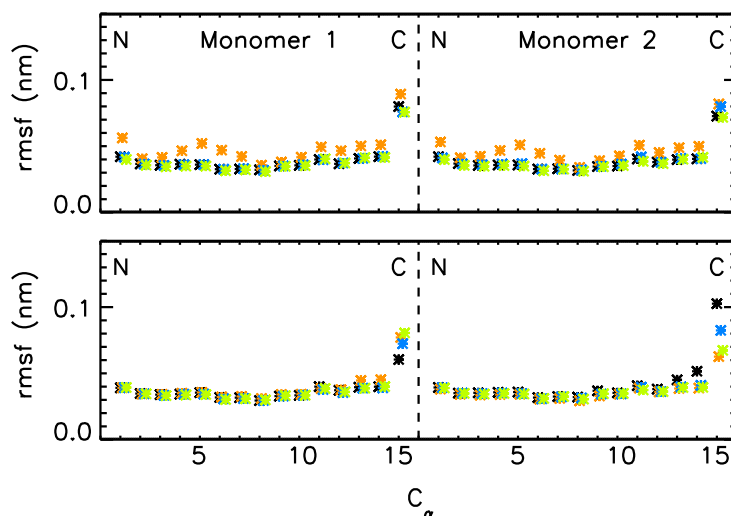
Figure 5.5: Root mean square fluctuations of the C_α-atoms of gramicidin. In the upper panel, the simulations at normal pressure, and in the lower panel, the simulations at enlarged pressure are shown (black: no alcohols, orange: with ethanol, blue: with octanol, and green: with decanol). Errors (computed on blocks of $5\,\mathrm{ns}$) are negligibly small and therefore omitted in the plot.

ably due to the increased fluidity of the lipid bilayer upon addition of ethanol. This effect was also seen in the autocorrelation function of the backbone N-H bond orientation (Fig. 5.6). Especially the initial fast decay ($< 0.1\,\mathrm{ns}$) associated with the local anisotropic diffusion of the N-H bonds [257] was significantly enhanced by ethanol for the amino acids close to the hydrophobic core (residue number ≤ 8). Application of external pres-

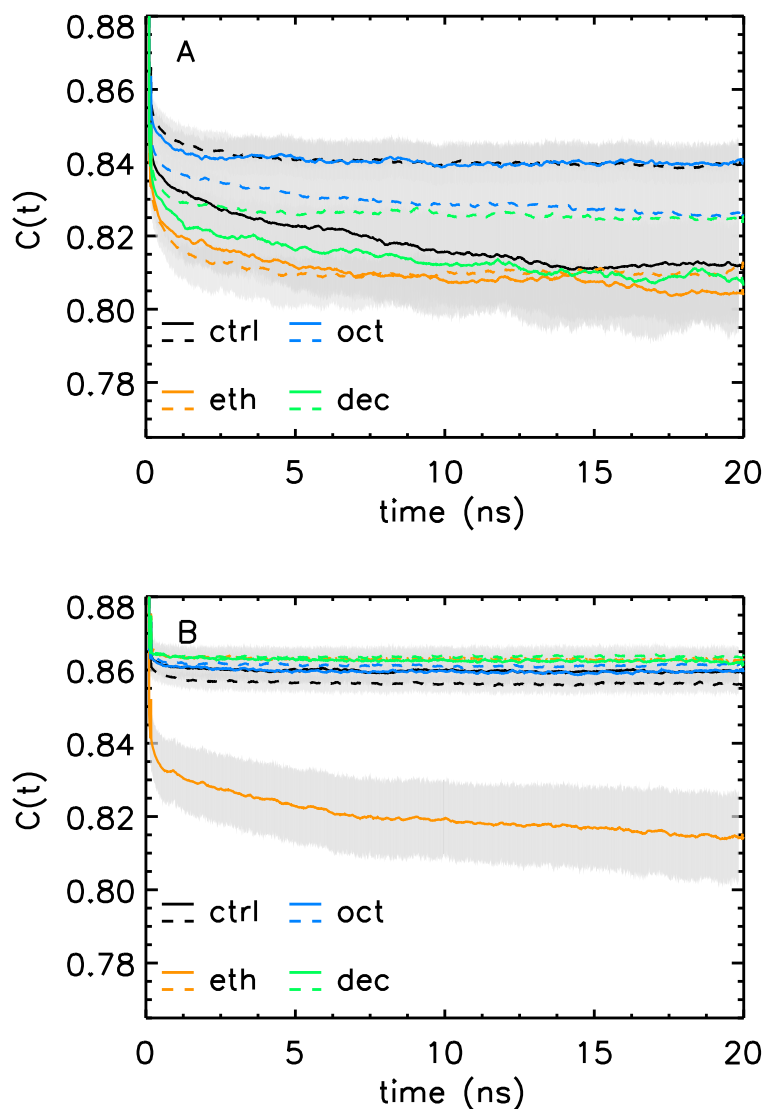Figure 5.6: Autocorrelation function of backbone N-H bond orientations, separately for the membrane-anchoring region of gramicidin (A, residues 9-15) and for the part of gramicidin embedded within the hydrophobic core of the lipid bilayer (B, residues 2-8). Val at position 1 was excluded from the plot due to very large variations. The N-H bond orientation autocorrelation function was computed after fit of the protein backbone to the starting structure, thereby excluding the (slow) anisotropic helical tumbling motion [257] of the gramicidin channel from the results.

sure reversed this effect. The influence of long-chain 1-alkanols on the dynamics of this transmembrane (TM) region was negligibly small. Alkanols and external pressure exerted a small effect on the N-H bond dynamics within the membrane-anchoring region of gramicidin (residue number ≥ 9). The dynamics in this region is most probably influenced by hydrogen bonding to lipid headgroups and alkanols (for octanol, see below), resulting in significantly increased decay times (between 0-2 ns) for the autocorrelation function as compared to the hydrophobic TM region.

The average tilt angle of the ion channel with respect to the membrane normal was $21 \pm 1°$ (1 bar). This value was decreased to $16 \pm 1°$ by application of a pressure of 600 bar. Inclusion of 1-alkanols into the bilayer decreased the gramicidin tilt angle to $10° - 14°$, while additional application of large external pressure reversed this effect for ethanol (see Table 5.3).

	Without 1-alkanols (°)	Ethanol (°)	Octanol (°)	Decanol (°)
1 bar	21 ± 1	14 ± 1	14 ± 1	10 ± 1
600 bar	16 ± 1	24 ± 2	17 ± 1	12 ± 1

Table 5.3: Average tilt angle of the gramicidin dimer versus the z-axis of the simulation box.

The interfacial tryptophan residues have an important role in anchoring the peptide inside the bilayer, and probably also for the overall ion channels' structure and function (see the reviews [46, 123, 128, 301]). In mutation studies, a replacement of tryptophan residues by phenylalanine side chains had a large influence on the ion conductance of gramicidin [12]; also anesthetics (halothane and F3) showed an effect on the tryptophan residues of gramicidin [39, 253–256, 303]. To see whether there is a competitive binding of 1-alkanols, lipids, and interfacial water to the tryptophan residues, we studied the hydrogen bonding of the tryptophan residues. In agreement with the area distribution of the 1-alkanols, hydrogen bonding of 1-alkanols to the tryptophan residues of gramicidin was rarely observed ($< 5\%$ of the simulation time for hydrogen bonding of ethanol to individual tryptophans, $\leq 1\%$ for octanol and decanol). The only exception was the simulation with octanol at large external pressure, where for a total of 22% of the simulation time hydrogen bonding of an octanol molecule to Trp9, and for 10% of the time to the interfacial Trp13 and Trp15 of the lower monomer occurred. Typically, either lipid or solvent molecules were hydrogen bonded to the tryptophan residues of gramicidin, independent of the presence of 1-alkanols.

The pore radius of gramicidin A varied along the central axis of the ion channel (Fig. 5.7). The maximum pore radius was found at the interconnect of the two monomers ($z \approx 0$ nm), and the minimum radii at $z \approx \pm 0.9$ nm, i. e., approximately at the inner potassium binding site of gramicidin [189]. Despite the overall structural stability of gramicidin, the pore radius significantly decreased in the membrane core region upon addition of ethanol, remained almost unmodified after adding octanol, and significantly increased for decanol. External pressure increased the pore radius of gramicidin in the pure phospholipid bilayer for the ethanol and octanol systems. The pore radius at 600 bar was similar for all investigated systems, comparable to the pore radius found after addition of decanol at normal pressure.

5.3.4 Lateral Pressure Profile

A "truly mechanistic" [33] model of anesthesia was suggested by R. Cantor [33–35]: Under the assumption of different conformations of ion channels for the closed and open

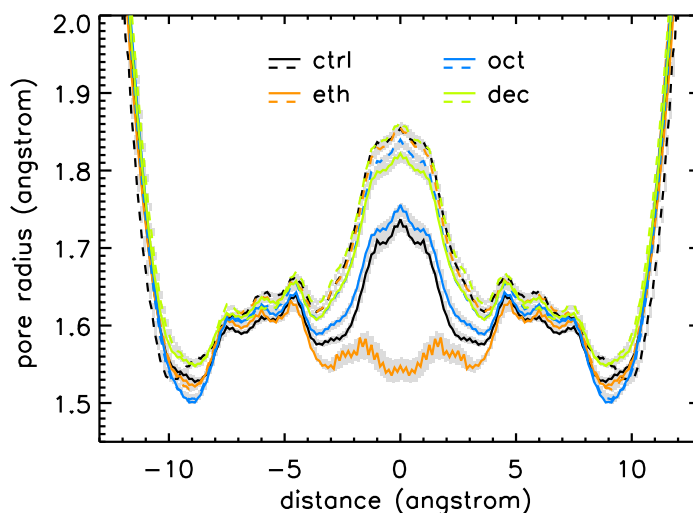Figure 5.7: Pore radius of gramicidin A, computed from one snapshot every $100\,\mathrm{ps}$, measured along the central axis through the peptide (symmetrized). The origin is chosen at the center of the ion channel. Results at $1\,\mathrm{bar}$ ($600\,\mathrm{bar}$) are represented by solid (dashed) lines. Errors are shown as grey-shaded areas.

state with different cross sectional areas, changes in the lateral force distribution inside the bilayer are supposed to shift the conformational equilibria between these states. Such conformational changes between open and closed states could be structural rearrangements of the protein, possibly accompanied by modulations of the channel pore radius. The latter idea of a change in ion channel pore radius would be appealing, as then a direct link to ion conductance might be provided.

Lateral pressure profiles calculated from the different simulations are given in Fig. 5.8. In these profiles, the characteristic properties of lipid bilayers were correctly reproduced: in the bilayer core, a positive lateral pressure resulted from entropic repulsion of the lipid acyl chains. At the hydrocarbon-water interface a large tension is observed due to the hydrophobic effect, striving to minimize the contact area between the apolar lipid chains and the polar solvent. This negative tension peak is interrupted by a small positive peak, resulting from lipid headgroup-headgroup repulsion and solvent-solvent interactions of ordered interfacial water molecules (compare [88, 241]). Further outside, the pressure difference between the normal and the lateral pressure drops to approximately zero in the bulk water region.

Comparison of the pressure profile of the DMPC-gramicidin system studied here to the corresponding profile of a pure DMPC system (not shown) [88] shows only a minor influence of the gramicidin on the membrane lateral pressure profile, in agreement with results of Gullingsrud et al. [90] for the peptide melittin in DMPC lipid bilayers.

Upon addition of ethanol molecules, the peaks of the pressure profile were decreased in magnitude, such that the overall profile appeared smoothed. With octanol, no significant pressure changes in the bilayer interior were found, but – in agreement with the increased area per lipid in these simulations (pure DMPC, $1\,\mathrm{bar}$: $40.12 \pm 0.12\,\mathrm{nm}^2$; DMPC with

octanol, $1\,\mathrm{bar}$: $44.66 \pm 0.10\,\mathrm{nm}^2$) – the lipid headgroup-headgroup and solvent-solvent repulsion of ordered water molecules at the bilayer-water interface was decreased. Decanol enhanced the central maximum of the profile. For the lower monolayer ($z < 0$), containing the larger number of decanol molecules, the profile was broadened, in line with the overall thickness increase of the bilayer with decanol. At $600\,\mathrm{bar}$ pressure, the profile without 1-alkanols was smoothed. With ethanol, the positive contribution inside the bilayer as well as the interfacial tension term were slightly increased with respect to the simulations with ethanol at normal pressure. The profile with octanol was only slightly broadened by the increase in bilayer thickness. For the lower monolayer of decanol, an additional strong tension term inside the bilayer at $z \approx -0.8\,\mathrm{nm}$ occurred, similar to our previous study on pure alkanol-DMPC systems [88].

The insensitivity of the pressure profiles to the addition of octanol suggests a stabilizing effect of gramicidin, as for lipid bilayers without proteins large changes in the pressure profile upon addition of octanol had been found [88]. Interestingly, the comparatively small lateral pressure in the hydrophobic TM region after addition of ethanol at $1\,\mathrm{bar}$ is linked to a decreased gramicidin pore radius, and the largest pressure seen after addition of decanol to an increase in the pore radius. The radius decrease for ethanol at $1\,\mathrm{bar}$ is coupled to a decrease in intramolecular hydrogen bond formation (data not shown).
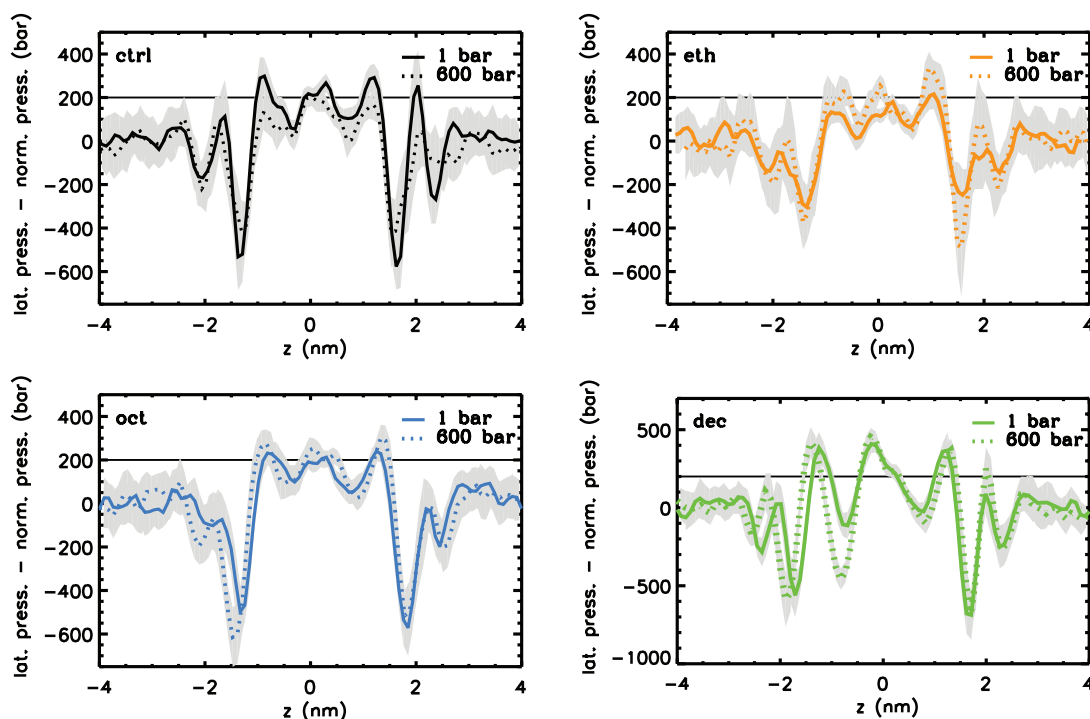
Figure 5.8: Lateral pressure profiles for the simulation systems without any 1-alkanols (upper left panel), with ethanol (upper right panel), with octanol (lower left panel), and with decanol (lower right panel). Results at $1\,\mathrm{bar}$ ($600\,\mathrm{bar}$) are represented by solid (dashed) lines. Please note the scaled ordinate for the simulations with decanol. The horizontal line at $200\,\mathrm{bar}$ is shown as a guide for the eye.

5.4 Discussion

A major drawback of earlier simulation studies of anesthetics acting on gramicidin in a lipid environment was the short simulation time [257]. The obtained distribution of anesthetics was probably biased due to pre-insertion of the anesthetic molecules into the membrane and by the short equilibration time. In contrast, here the 1-alkanols were randomly distributed in the water phase at the beginning of the simulations and then let to freely diffuse into and inside the bilayer. Therefore, an important result of this study is the distribution of 1-alkanols inside the bilayer with respect to the embedded peptide. The region in close proximity of gramicidin was found to be depleted of 1-alkanols, different from the preferred interaction of halothane with a potassium channel reported recently [287]. This observation renders a chemical binding between gramicidin A and the 1-alkanols, necessary for any kind of protein-binding model of anesthesia, unlikely and hints to a lipid-mediated mechanism.

While the influence of octanol on the structure of gramicidin was small, ethanol and decanol had a significant, however opposed effect on the gramicidin pore radius. The overall conformational stability of gramicidin is in agreement with previous studies using halothane and F3 as anesthetics [255–257]. However, our simulations oppose the view [257] that the anesthetic action is induced by the binding of drug molecules to the interfacial tryptophan residues. Rather, our results suggest a modulation of membrane properties which in turn affect the structure and dynamics predominantly of the hydrophobic TM domain.

Even for the small-sized gramicidin channel, a correlation between variations in the ion channel pore radius and the central peak in the lateral pressure profile was observed for ethanol and decanol (pure DMPC and octanol did not show significant changes in the central pressure peak). This finding lends support to the model for anesthesia suggested by Cantor [33–35], where changes in the lateral pressure profile are assumed to shift conformational equilibria of ion channels if the cross sectional area difference of open and closed states varies in the direction of the bilayer normal. The observed relation between the structure and the dynamics of gramicidin A on the one hand, and the addition of different 1-alkanols or the application of external pressure on the other hand, provides evidence for an influence of 1-alkanols and external pressure on the ion conductance of gramicidin. In this respect, potential of mean force calculations, directly evaluating the free energy barrier for ion passage through the channel, could give further insight. This is, however, beyond the scope of this manuscript.

5.5 Summary and Conclusions

In this study, we have shown that 1-alkanols of different hydrocarbon chain length distributed inhomogeneously in the lipid bilayer with respect to an embedded gramicidin A dimer. In close proximity to the peptide, the area density of 1-alkanols was decreased, providing evidence against a protein-binding model for anesthesia. 1-alkanol-induced changes in the structure and dynamics of gramicidin were found. The pore radius of the gramicidin channel was influenced by the 1-alkanols depending on their hydrocarbon

chain length. This effect was probably achieved by the modulation of the lateral pressure in the membrane. We showed here, that alkanols with a short chain may exert an opposite effect on a membrane-embedded ion channel (here the gramicidin) as compared to long-chain 1-alkanols. The exact value for the transition point will probably depend on the membrane composition. Therefore, further studies focusing additionally on the influence of the lipid acyl chain length on the structure, dynamics, and on the conductivity of different ion channels, as well as investigating the effect of the protein concentration in the bilayer appear mandatory.

5.6 Acknowledgment

6 Summary, Conclusions, and Outlook

In the simulations presented here, modifications of lipid bilayer properties by addition of 1-alkanols have been observed. For simplified model proteins of a certain geometric shape, a shifted equilibrium between two states, interpreted as a closed and an open or an active and an inactive state, was found in the presence of 1-alkanols, and an opposite shift was observed upon additional application of pressure. The latter findings can be associated with an anesthetic action on a molecular level according to Cantor [36]. Simulations of the small ion channel gramicidin embedded in a lipid bilayer showed a strongly inhomogeneous distribution of 1-alkanol molecules within the bilayer plane, with almost no drug molecules residing in close vicinity of the peptide. Still, the pore radius of gramicidin was strongly modified in simulation of the peptide-bilayer system with ethanol and decanol.

The alteration of bilayer properties in response to the presence of anesthetics, and the absence of any specific interaction between gramicidin and 1-alkanol molecules support the view of a lipid or lipid-mediated mechanism for anesthesia. Based on the calculations with model membrane proteins, a regulation of ion channel activity by anesthetics via the lateral pressure profile as suggested by Cantor [33] seems feasible.

In future studies it would be desirable to simulate more complete models of biological membranes including larger and more complex proteins, different types of lipids, and also some sterols with their bulky ring structure. Assuming a unitary mechanism for anesthesia as the universality of the Meyer-Overton correlation suggests, simulations of a broad variety of anesthetics will have to be performed to identify mechanisms valid for all anesthetics alike. However, this will require an enormous computational effort and can only be achieved by introducing appropriate simplifications to speed up the simulations. Coarse-grained simulations as introduced in the second part of this thesis will be a valuable tool to address this problem.

A completely different approach to identify mechanisms underlying anesthesia could be based on a possible stereoselectivity of the anesthetic interaction. Stereoisomers are molecules that have the same chemical formula and structure, but differ by their chirality. They are like a molecule and its mirror image and have the same physico-chemical properties. Simulating the effect of the two stereoisomers of a drug – one having anesthetic potency and the other lacking this potency – on a lipid-protein system, should give valuable information about the relevant interactions for anesthesia. However, the literature concerning stereoselectivity of general anesthetics is very controversial: various studies have reported stereoselective interactions of anesthetics [58, 80, 96, 150, 171, 208], while other authors found no stereoselectivity [63, 74, 75, 124, 207, 209]. As most of the experiments have been carried out *in vivo*, it is also not known, whether the actual anesthetic

mechanism, or rather the transport of anesthetics towards their site of action is stereoselective. Nevertheless, if in experiments stereoselectivity could be undoubtedly verified on a single receptor level, simulations of this receptor would be promising.

Part II

Protein Adsorption on Solid Surfaces

7 Protein Adsorption

Protein adsorption on solid–liquid interfaces is a fundamental biological process that is relevant for a broad range of medical and biotechnological applications (see Section 7.1). As proteins are large macromolecules that might undergo surface-induced conformational changes, many different entropic and enthalpic terms are effective during protein adsorption on solids and a complete theoretical description and a control of this process are difficult to obtain.

Here, coarse-grained (CG) molecular dynamics simulations were used to study the adsorption of two different proteins, namely of lysozyme and human serum albumin (HSA), on a negatively charged solid surface. The applicability of the CG model was tested by comparison to experimentally known results, and analyses of the protein orientation on the solid surface, of structural changes of the protein during the course of the simulations, and of enthalpic interactions between the protein, the solvent, and the solid surface are presented.

7.1 Motivation

When an aqueous protein solution is brought into contact with a solid material, in almost all cases proteins adsorb spontaneously at the interface (see, e. g., [48]). This behavior is exploited for diverse technical applications like, e. g., for solid phase immunoassays employed in medical diagnostics, for biosensors and biochips ("lab on a chip") used to analyze solutions containing several different proteins, for bioreactors, where a series of reaction steps is catalyzed by spatially separated enzymes adsorbed on a solid surface, and for tissue engineering (see the reviews [49, 122]). On the other hand, the protein adsorption on surfaces can also be harmful like in the case of the aggregation of lysozyme (present in the tear fluid) on contact lenses leading to infections. Protein adsorption is the first and decisive step in the formation of a biofilm on, e. g., implant material or teeth: as cells and bacteria can in general not attach to the bare solid surface, but adhere to the inital protein layer formed on the surface, the nature of the emerging biofilms, and therefore the integration of implant material into, or its rejection from bodily tissue or the built up of dental plaque on teeth, depend critically on the kind of proteins covering the surface.

In all these examples, a control of the protein adsorption process would be desirable. One method explored today is the design of functional interfaces, as it has been found that, for example, proteins adsorb more easily on hydrophobic surfaces than on hydrophilic surfaces (see [48, 154] and references therein). Also coatings, like the so-called polymer brushs and self-assembled monolayers (see, e. g., [48, 49]), can inhibit protein adsorption on solid surfaces [49]. However, until now most of these approaches are empirically based

and a complete (theoretical) understanding of the adsorption process, allowing for systematic modifications, is lacking. Here, simulation studies can provide important insights and details that are difficult or impossible to obtain in experiments.

8 Methods

8.1 Coarse-Grained Molecular Dynamics Simulations

Coarse-grained molecular dynamics simulations have gained increasing popularity in the last years due to the desire to study processes taking place on the microsecond time scale in large nanoscopic systems. The term coarse-graining refers to the introduction of additional simplifications and approximations in atomistic molecular dynamics simulations. Thereby a speed-up of the simulations can be achieved and larger systems can be simulated for longer time intervals. Many different models and levels of simplification have been suggested, ranging from simulations of simple binary Lennard Jones fluids [85], over models treating proteins and lipids in some detail, but using an implicit representation of the solvent and of solid materials [182, 183], up to simulation schemes, where all interactions are treated explicitly and the chemical nature of macromolecules is mostly retained. Extensive reviews of the different approaches have been given by Nielsen et al. [181], Tozzini [267], Venturoli et al. [290], and Müller et al. [174].

Here, the MARTINI coarse-graining scheme (see Section 8.1.1) suggested by Marrink and co-workers [156, 161, 170] has been used. In this model, a reduction of the number of degrees of freedom – and thereby a speed-up of the simulations – is achieved by combining (functional groups of) several atoms into one larger particle, a so-called coarse-grained bead. Only a few bead types (see Section 8.1.1) are defined and the model provides a systematic parametrization of all possible interactions between all different coarse-grained beads, allowing for a broad range of different applications [170]. In comparison to atomistic simulations, a considerable increase in simulation speed is obtained, but still a relatively high resolution reflecting the structural details and the charge distribution of large molecules is retained and solvent is explicitly taken into account (i. e., water is simulated using explicit particle-particle interactions between coarse-grained water beads and is not approximated as a continuous medium). First applications of this model have given promising results (see Section 8.1.1) and the model is expected to gain further importance in biomolecular modeling.

8.1.1 MARTINI

The MARTINI force field [156, 161, 170] was first released in 2004 as a model for semi-quantitative coarse-grained simulations of lipids in water [156]. The model was shown to reproduce known structural and dynamical properties of lipid bilayers of various composition [156]. Using different lipid species, not only the self-assembly of lipids to a fluid

bilayer, but also the transition to a crystalline state upon cooling, and the formation of an inverted hexagonal phase and of micelles could be observed [156, 160]. In the following, the MARTINI force field was successfully applied to study phospholipid vesicles [159] and to investigate domain formation in mixed phospholipid bilayers [70]. Bond and Samson et al. [25–27] and Shih et al. [235] based coarse-grained simulations of membrane proteins on this force field, though still applying harmonic constraints or additional dihedral potentials to keep the proteins stable. In 2007, an improved version of the MARTINI force field [161] and, in 2008, its extension to peptides [170] were published. The model was since then applied to study, e. g., the oligomerization of rhodopsin [200] and the gating of membrane protein channels [270, 304].

The MARTINI force field was calibrated to reproduce partitioning free energies between polar and apolar phases of various chemical compounds [161, 170]. In this model, all hydrogen atoms are disregarded and (functional) groups of – on average – four atoms are mapped onto coarse-grained beads. Exceptions are ring-like structures as in sterols or in the amino acid tryptophan, where a higher resolution mapping is used. Four main classes of beads are defined: apolar (C), nonpolar (N), polar (P), and charged (Q) beads. A fine-tuning of interactions is achieved by introducing subtypes of these classes: for the polar and apolar beads, the degree of (a)polarity is assigned by numbers 1 to 5, where increasing numbers mark increasing polarity. For the non-polar and charged beads, subtypes are distinguished according to their hydrogen bonding capability: a = acceptor, d = donor, da = donor and acceptor, and 0 = no preference for hydrogen bonding. All beads have the same mass $m = 72\,\mathrm{u}$ of four water molecules, except the beads in ring-like structures with a mass of $45\,\mathrm{u}$.

Like in all-atom force fields (see Section 2.2.1), bonds between nearest neighbors are modeled by a harmonic spring and angles between next nearest neighbors are defined by a harmonic angle potential. For aliphatic carbon chains, the bond length is generally set to $0.47\,\mathrm{nm}$, while for proteins it is adjusted individually based on statistical considerations [170]. Proper dihedral potentials are used to impose the correct secondary structure on peptide backbones. Also the functional form for the non-bonded interactions is chosen equivalent to the all-atom case (Eq. (2.13)):

$$
\begin{aligned}
V_{\mathrm{non-bonded}} &= V_{\mathrm{LJ}} + V_{\mathrm{Coulomb}} \\
&= \sum_{\mathrm{pairs(i,j)}} 4\varepsilon_{ij}\left(\left(\frac{\sigma_{ij}}{r_{ij}}\right)^{12} - \left(\frac{\sigma_{ij}}{r_{ij}}\right)^{6}\right) + \sum_{\mathrm{pairs(i,j)}} \frac{1}{4\pi\varepsilon_0\varepsilon_r}\frac{q_i q_j}{r_{ij}} \quad .
\end{aligned}
$$

The minimum distance between two non-bonded particles i and j is in general set to $\sigma_{ij} = 0.47\,\mathrm{nm}$, except for ring structures ($\sigma_{ij} = 0.43\,\mathrm{nm}$) and for strongly repulsive interactions between charged and apolar beads ($\sigma_{ij} = 0.62\,\mathrm{nm}$). Lennard Jones interactions between bonded next neighbors are excluded in the MARTINI model. For the strength of the interaction ε_{ij} between two beads, ten different levels are defined, ranging from strongly attractive interactions between charged particles to strongly repulsive interactions between apolar and charged particles. In ring-like structures, ε_{ij} is scaled to 75% of its original value. Lennard Jones interactions are shifted to zero in the cutoff region between $0.9\,\mathrm{nm}$ and $1.2\,\mathrm{nm}$. Electrostatic interactions between charges q_i and q_j at the distance r_{ij} are modeled including a dielectric screening by setting $\varepsilon_r = 15$. The Coulomb potential is truncated at the cutoff radius $r_{\mathrm{cutoff}} = 1.2\,\mathrm{nm}$. The interactions are shifted to

zero over the whole interaction range, mimicking a distance-dependent screening.

Compared to atomistic simulations, a speed-up by 3-4 orders of magnitude can be obtained using the MARTINI coarse-grained model [156]. Different factors contribute to this effect: the reduction of the number of degrees of freedom, the truncation of the electrostatic interactions, the use of a large time step of 20 to $50\,\text{fs}$, and a faster intrinsic dynamics [156, 161]. The use of a large time step is made possible by disregarding all hydrogen atoms, by combining groups of atoms into larger and heavier beads, and by – similar to the atomistic simulations (see Section 2.2.4) – constraining the length of covalent bonds. For the same reasons, small variations in the energy landscape are smoothed, leading to a reduced friction and to a faster overall dynamics of the system. By comparison with atomistic simulations and experimental data, the dynamics have been found to be increased by a factor of ≈ 4 [156].

The MARTINI force field was designed for use close to room temperature and at normal pressure [156]. As coarse-grained water, modeled by one polar P4 bead per four real water molecules, was found to freeze already at temperatures of $290\,\text{K}$ [156], Marrink et al. [161] introduced antifreeze particles BP4, with an increased radius compared to particles P4. Replacing 0.1 mole fraction of P4 water beads by these antifreeze particles lowers the freezing temperature, but it also reduces the density and the self-diffusion constant of water by about 10% [161]. However, no effect on structural properties of a hydrated lipid bilayer were found [161].

When applying the MARTINI force field, some deficiencies in the parametrization should be kept in mind. First of all, the calibration of force field parameters according to free energies results in a bias of both entropy and enthalpy, as the loss of entropy, inherent in the coarse-grained model, is compensated by a reduced enthalpy term. Secondly, all parametrization was done in the fluid phase. Therefore, buried residues in large proteins, which can be in an intermediate state between fluid and crystallized, might be described inadequately [170]. Furthermore, a too weak adsorption of positively charged amino acids at membrane-water interfaces was observed [170]. And finally, although the force field was released for use with proteins [170], simulations of lysozyme and barnase in solution revealed anomalously large structural deviations of these proteins from their native structure during the course of the simulations. Similar problems were encountered by Tieleman et al. [261]. Therefore, with the current version of the MARTINI force field, additional constraints have to be used to stabilize the structure of proteins.

Limitations for the applicability of the MARTINI force field result from the cutoff used for non-bonded interactions and from the way how proteins are modeled. By truncating electrostatic interactions, all long-range interactions are abandoned and artifacts will be inevitable (see Section 2.2.2). In principle, also in coarse-grained simulations, lattice summation or reaction field methods could be applied. However, this would make the simulations slower and the force field parameters would probably have to be readjusted. In the modeling of peptides and proteins, secondary structure elements are fixed by angle and dihedral potential terms. Therefore, only movements of different structural elements in relation to each other, but no change in secondary structure can be investigated [170].

Nevertheless, the MARTINI method is certainly one of the most efficient, systematically parameterized coarse-grained models available today, being applicable to diverse systems, and allowing for microsecond long high-resolution simulations of large systems (about 2.5×10^6 atoms).

8.2 Principal Component Analysis

Principal component analysis (PCA) [199], also called covariance analysis, essential dynamics, or proper orthogonal decomposition, is a method to reduce high-dimensional data sets to a lower number of dimensions, but still keeping most of the relevant information. Applications of this technique include image compression and pattern and face recognition. In biomolecular simulations, PCA is used to identify functional motions in proteins [5, 54].

Starting from a data set of $3N \times M$ data points, e. g., a trajectory of N protein atoms and M time steps in MD simulations, first the time average of each degree of freedom is subtracted at each time step to retrieve only the relevant internal motions. In simulations, this is usually done slightly different, namely by fitting the structures at each time step to one reference structure. From this data, arranged in a $3N \times M$ matrix $\mathbf{B}$ with the columns containing the coordinates of all atoms $\mathbf{x}(t)$, the covariance matrix

$$\mathbf{C} \;=\; \frac{1}{M}\,\mathbf{B}\,\mathbf{B}^{\star} \tag{8.1}$$

$$C_{ij} \;=\; \langle\, (x_i - \langle x_i \rangle)\ (x_j - \langle x_j \rangle)\, \rangle \tag{8.2}$$

is built, where $\mathbf{B}^{\star}$ is the conjugate transpose of $\mathbf{B}$ and $\langle \ldots \rangle$ denotes the average over all times. This matrix can be diagonalized by a linear, orthonormal transformation $\mathbf{V}$. The columns of $\mathbf{V}$ are the eigenvectors of $\mathbf{C}$, also called principal or essential modes. For convenience, they are arranged by decreasing order of the corresponding eigenvalues λ_i:

$$\mathbf{V}^{-1}\mathbf{C}\mathbf{V} = diag(\lambda_1, \lambda_2, \ldots, \lambda_{3N}) \quad \text{with } \lambda_1 \geq \lambda_2 \geq \cdots \geq \lambda_{3N}. \tag{8.3}$$

The eigenvectors span a coordinate system, with the special property that the covariance of any two coordinates is zero; i. e., the motions along these coordinates are uncorrelated. The eigenvalues λ_i are a measure for the mean square fluctuations along the respective eigenvector. For systems with a confined geometry, as for example a protein trapped in a local minimum of its energy landscape, many degrees of freedom are restricted by energy barriers and the corresponding eigenvalues will be close to zero. Assuming that important dynamics are connected with large fluctuations, a projection of the data on the first few eigenvectors reveals and separates the fundamental motions:

$$\mathbf{p}(t) = \mathbf{W}^{\star}\,(\mathbf{x}(t) - \langle \mathbf{x} \rangle) \quad . \tag{8.4}$$

The $p_i(t)$ are called the principal components. The matrix $\mathbf{W}$ is a subset of $\mathbf{V}$, keeping only the most important (in terms of large eigenvalues) eigenvectors

$$\begin{aligned} W(p,q) = V(p,q) \quad \text{with} \quad p &= 1, \ldots, 3N \\ q &= 1, \ldots, L \\ 1 &\leq L \leq 3N \quad . \end{aligned} \tag{8.5}$$

For a mass-weighted analysis of Newtonian dynamics, the atom masses have to be included in the Equations 8.2 and 8.4.

In the case of insufficient sampling in the simulations, the results of the PCA can be biased by random diffusion in fluctuation space. It has been shown that the principal components $p_i(t)$ of this random diffusion are cosine-shaped with the number of periods equal to half the principal component index i [104]. Hints to random diffusion are a large cosine content [105]

$$c_i = \frac{2}{T} \left(\int_0^T \cos(i\pi t)\, p_i(t)\, dt \right)^2 \left(\int_0^T p_i^2(t) dt \right)^{-1} \tag{8.6}$$

of the pricipal components ($T =$ sampling time interval) or a small subspace overlap

$$\text{overlap}(\mathbf{W}_n, \mathbf{W}_m) = \frac{1}{L_n} \sum_{s=1}^{L_n} \sum_{t=1}^{L_m} (\mathbf{w}_{n,s} \cdot \mathbf{w}_{m,t})^2 \tag{8.7}$$

of the subspaces $\mathbf{W}_n$, $\mathbf{W}_m$ of different time intervals n, m of the trajectory ($\mathbf{w}_{n,s}$, $\mathbf{w}_{m,t}$ are the eigenvectors spanning the subspace $\mathbf{W}_n$, $\mathbf{W}_m$) [105]. However, a small overlap of parts of the trajectory can equally well indicate a structural change of the protein. In the case of microsecond long coarse-grained simulations of proteins, a sufficient sampling of the protein mobility can be safely assumed and a small subspace overlap for different time intervals of the trajectory can therefore be assigned to conformational transitions of the simulated proteins.

9 Coarse-Grained Simulations of Protein Adsorption on Solid Surfaces

Beate Griepernau [1] *, Christian Hanke* [1] *, and Rainer A. Böckmann* [1]

The adsorption of proteins on solids and soft materials plays a vital role in biotechnological and biomedical applications, for example for the biocompatibility of implant material or in dental health care. Not only the properties of the sorbent surface can be changed, but also the proteins might undergo conformational changes during adsorption. To investigate such processes in molecular detail, but still reaching appropriate time scales (microseconds), coarse-grained molecular dynamics simulations were applied here. As a model system, the adsorption of lysozyme and human serum albumin to a simple, slightly negatively charged, single-layer solid surface were studied at various ion concentrations. Protein diffusion before and after attachment to the surface, the orientation of the proteins on the surface, energetic interactions driving adhesion, and conformational changes of the proteins in the course of the simulations have been analyzed.

[1]Theoretical and Computational Membrane Biology, Center for Bioinformatics Saar, Saarland University, PO Box 15 11 50, 66041 Saarbrücken, Germany

9.1 Introduction

Protein adsorption on solid–liquid interfaces plays an increasingly important role in many biotechnological and biomedical applications. Examples are solid-phase immunoassays for medical diagnostics, biosensors ("lab on a chip"), and the use of implants, where protein adsorption is the first step in the formation of a biofilm that is critical for the integration of the material into, or its rejection from, bodily tissue. As protein adsorption can be both harmful, i. e., the accumulation of lysozyme (present in the tear fluid) on contact lenses, but also desirable, as in the case of albumin adsorption on implant material preventing the adhesion of platelets and thrombus formation, the ultimate goal is an understanding and a control of the adsorption process. The latter could be achieved for example by a design of functional surfaces favoring or inhibiting adsorption of selected proteins.

Experimentally accessible quantities include the adsorbed layer thickness, the adsorbed protein mass and concentration, and rate constants for adsorption processes. Single molecule interactions and changes in the conformation and orientation of single proteins can partially be investigated using attenuated total reflectance Fourier transform infrared spectroscopy (ATR-FT-IR), total internal reflection fluorescence spectroscopy (TIRF), and atomic force microscopy (AFM), but are in general difficult to determine. In this respect, simulations are a valuable tool providing the desired detailed information.

As proteins adsorption takes places on time scales of microseconds up to milliseconds [86], atomistic simulations, limited to nanosecond long timescales, cannot be used. Up to now, mainly colloidal models (e. g., [13, 87, 187, 188, 210, 215, 219–221]), where the whole protein is represented by a single sphere that moves in a potential mimicking a solvent, have been applied to investigate this process by Brownian Dynamics, Monte Carlo (MC), or Random Sequential Adsorption [251] techniques. Enhanced levels of sophistication have been achieved using an inhomogeneous charge distribution for the protein or including conformational changes by introducing additional degrees of freedom (e. g., [13, 210]). Two more detailed approaches retaining structural characteristics of the protein, were given by the united residue MC simulations of Zhou et al. [306], where each amino acid was represented by a sphere, and by the rigid-body MC simulations of Ravichandran et al. [214], where lysozyme was simulated in full atomistic detail, but without any structural flexibility.

Here, the recently developed MARTINI force field [156, 161, 170] was used to investigate the adsorption of two proteins, lysozyme and human serum albumin (HSA), on a negatively charged solid surface by microsecond long, coarse-grained molecular dynamics (MD) simulations. Within this framework, we were able to study the time evolution of the system and to simulate the solvent explicitly. Lysozyme can be found in human saliva and tear fluid, playing an important role in the defense of the organism against bacteria, and HSA is abundant in the human blood plasm, being responsible for diverse transport processes and for maintaining the osmotic pressure. Both proteins have been intensively studied in experiments, allowing for a direct comparison and a validation of results obtained from the simulations.

The focus of this study was put on the applicability and the possibilities of coarse-grained molecular dynamics simulations for investigating protein adsorption processes on solids, on the determination of the orientation of the proteins on the surface, and on the calcu-

lation of energetic interactions that are important for the adhesion of the proteins on the solid surface.

9.2 Methods

For the coarse-grained MD simulations performed in this study, the GROMACS software package [18, 143, 278] together with the MARTINI force field [156, 161, 170] has been used. At the start of each simulation, a protein – either lysozyme or HSA – was placed in a water-ion-solution above a solid surface that was oriented along the x–y plane (Fig. 9.1). A vacuum layer of $\sim 70\,\mathrm{nm}$ thickness in z-direction finished the set-up.
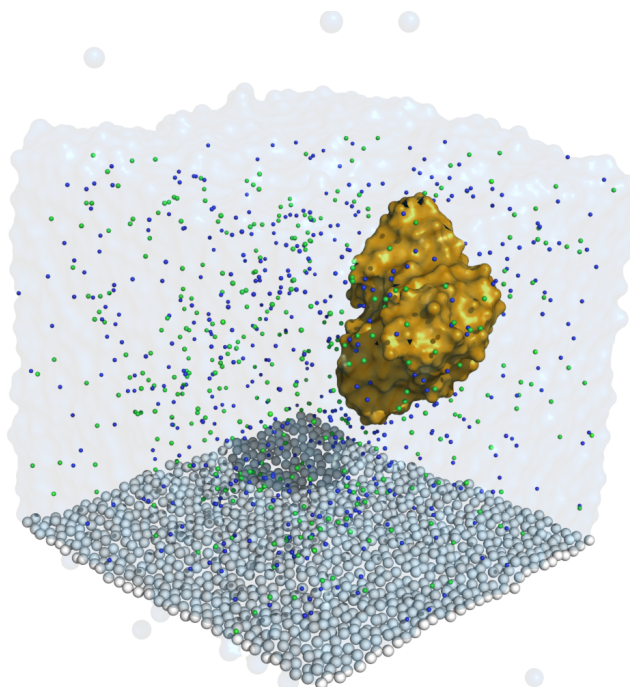

Figure 9.1: Simulation system for the adsorption study of human serum albumin (HSA, orange) on a solid surface (grey spheres) in explicit ionic solution ($0.2\,\mathrm{M}$ NaCl, green and blue spheres). Initially, HSA is randomly placed in the water box.

The solid surface was built up by a monolayer of non-polar coarse-grained beads arranged in a quadratic lattice. In order to mimic a mica surface, some randomly chosen, non-polar beads were replaced by negatively charged beads, such that a charge density of $-0.5\,e/\mathrm{nm}^2$ (electron charge $e = 1.602 \times 10^{-19}\,\mathrm{C}$) was obtained. The spacing between neighboring beads, which were connected by covalent bonds, was set to $0.47\,\mathrm{nm}$. To prevent any drift of the system, the position of three or four (simulations with lysozyme or HSA, respectively) solid atoms were constrained by a harmonic potential.

The all-atom protein structures of lysozyme (1LYD [218]) and of HSA (1BM0 [246]) were taken from the protein data bank [21]. For HSA, residues that had not been resolved

experimently were remodeled using the package WHATIF [292]. Lysozyme was simulated carrying a positive charge of $+8\,e$ (isoelectric point (pI) of lysozyme pI $\sim$ 11), while HSA was taken as uncharged (pI $\sim$ 5). The coarse-grained coordinates and topologies were produced according the procedure described by Monticelli et al. [170]. As lysozyme in solution was found to be unstable in simulations, the secondary structure of lysozyme and HSA was preserved by applying harmonic constraints (force constant of $1000\,\mathrm{kJ/(mol\,nm)}$) between all non-bonded protein beads with a distance of less than $0.65\,\mathrm{nm}$ (compare also [25, 26]). The proteins were placed with various orientations and a minimum distance of at least $2.6\,\mathrm{nm}$ (lysozyme) or $3.1\,\mathrm{nm}$ (HSA) to the substrate in a solution of water and NaCl. Like previously reported for the MARTINI force field (see [156, 161]), every tenth coarse-grained water bead had to be replaced by an enlarged, antifreeze bead to keep the water from freezing. Although this procedure lowers the self-diffusion constant of water by about 10%, no effects on the structural properties of hydrated lipid bilayers were found in simulations using the MARTINI force field [161]. The total size of the simulation box was fixed at $11\,\mathrm{nm}\,\times\,11\,\mathrm{nm}\,\times\,82\,\mathrm{nm}$ and $15\,\mathrm{nm}\,\times\,15\,\mathrm{nm}\,\times\,86\,\mathrm{nm}$ for the simulations with lysozyme and HSA, respectively. The systems were simulated using periodic boundary conditions, and a large vacuum layer was introduced to prevent interactions between copies of the system in z direction. A constant temperature of $300\,\mathrm{K}$ was maintained using the Berendsen weak coupling algorithm [16] with a coupling time constant of $1\,\mathrm{ps}$. An integration time step of $20\,\mathrm{fs}$ was used and the neighbor list was updated every $10\,\mathrm{th}$ integration step. Lennard Jones and electrostatic interactions were truncated using a shift cutoff between $0.9\,\mathrm{nm}$ and $1.2\,\mathrm{nm}$ and between $0.0\,\mathrm{nm}$ and $1.2\,\mathrm{nm}$, respectively. The dielectric constant for the Coulomb interactions was set to $\varepsilon_r = 15$.

In order to obtain statistically relevant data, a large number of microsecond long simulations has been accomplished. For lysozyme, simulations at six different salt concentrations, ranging from 0.0 to 1.0 molar, have been performed. At each concentration, eight simulations, differing in the initial orientation of the protein, have been carried out for 1 up to $4\,\mu s$ (depending on the adsorption time of the protein). In the case of HSA, eight systems at two concentrations, 0.2 and 0.6 molar, have been simulated for $7\,\mu s$ each. Accounting for the accelerated dynamics in coarse-grained simulations of a factor of ≈ 4 [156, 161], the times of the individual simulations are up to $28\,\mu s$ long. In the following, always the real simulation times (not multiplied by the factor of four) will be given.

9.3 Results and Discussion

9.3.1 Adsorption Times and Protein Diffusion

In all simulations, the proteins adsorbed and finally remained on the solid surface. Here, adsorption was said to occur when the minimal distance between the surface and the protein was less than $0.5\,\mathrm{nm}$. Ultimate or final adsorption refers to the protein staying on the surface for the remainder of the simulation time, at least $300\,\mathrm{ns}$ for lysozyme and $3\,\mu s$ for HSA. Already before the final adsorption, temporary adsorption events occurred for

both proteins. For lysozyme, the mean final adsorption times (i. e., the time at which the ultimate adsorption occurred) ranged from $0.5\,\mu\mathrm{s}$ to $1.3\,\mu\mathrm{s}$ at the different concentrations, whereas for HSA this time was slightly longer (see Fig. 9.2). This effect was at least partially due to a slower diffusion of the larger HSA molecules compared to the smaller lysozyme. Neither for lysozyme nor for HSA, a significant dependency of the mean final adsorption time on the ion concentration in solution was found. However, the time of the first contact between lysozyme and the solid surface was slightly increased with increasing ion concentration, reflecting the decreased diffusion coefficient of lysozyme with increasing ion concentration in solution (see below).
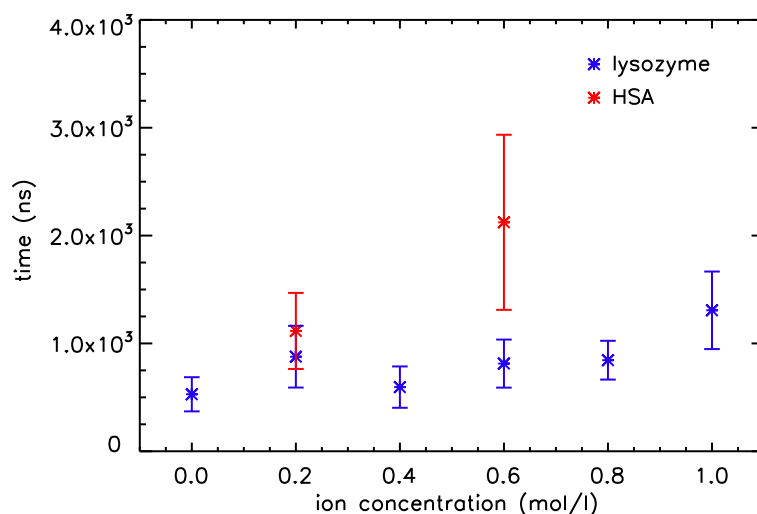

Figure 9.2: Mean final adsorption times for lysozyme and HSA on the solid surface.

The lateral (x–y plane) diffusion coefficient of lysozyme and HSA in solution decreased with increasing ion concentration (Fig. 9.3). At an ion concentration of $0.2\,\mathrm{M}$ NaCl, values of $D = (8.4 \pm 0.6) \times 10^{-7}\,\mathrm{cm^2\,s^{-1}}$ (lysozyme) and $D = (4.0 \pm 0.1) \times 10^{-7}\,\mathrm{cm^2\,s^{-1}}$ (HSA) were obtained from the simulations. Correcting these values by about 10% to account for the decreased water diffusion upon addition of antifreeze particles [161], these values are in good agreement with experimentally determined diffusion coefficients of $D = (10.6 \pm 0.1) \times 10^{-7}\,\mathrm{cm^2\,s^{-1}}$ for lysozyme in a physiological buffer [61] and of $D \approx 5.8 \times 10^{-7}\,\mathrm{cm^2\,s^{-1}}$ for bovine serum albumin (BSA, similar to HSA) in a solution with $\mathrm{pH} = 5.0$ and at ion concentrations ranging from 0.0 to $0.5\,\mathrm{M}$ [213].

After the final adsorption on the solid surface, the lateral diffusion of the proteins was strongly decreased. It became equal for both proteins and it was independent of the ion concentration in solution. Concerning surface diffusion of proteins adsorbed on the solid-liquid interface, only few experimental studies have been performed. For BSA adsorbed on poly(methylmethacrylate) and poly(dimethylsiloxane) surfaces, diffusion coefficients of the order of $D \sim 10^{-9}\,\mathrm{cm^2\,s^{-1}}$ [265] have been reported. For lysozyme adsorbed on mica, Mulheran et al. [173] deduced a diffusion coefficient of $D = 9 \times 10^{-16}\,\mathrm{cm^2\,s^{-1}}$ by comparing adsorption patterns of AFM experiments and Monte Carlo (MC) simula-

tions. However, compared to values reported from studies with other proteins and other substrates [186, 265], this value appears too low, maybe resulting from inaccuracies in the MC model. Nevertheless, the coarse-grained simulations presented here seem to overestimate the surface diffusion of lysozyme and HSA. This is probably due to the truncation of electrostatic and van der Waals interactions, and to the properties chosen for the model surface: simulating multiple solid layers, increasing the roughness, and changing the hydrophobicity of the surface are all expected to influence the protein diffusion on the surface. Also the lattice spacing (taken here as the typical distance between covalently bound particles in the MARTINI model) has an influence on the interaction energies between the protein and the surface [185] and therefore on the protein diffusion coefficient.
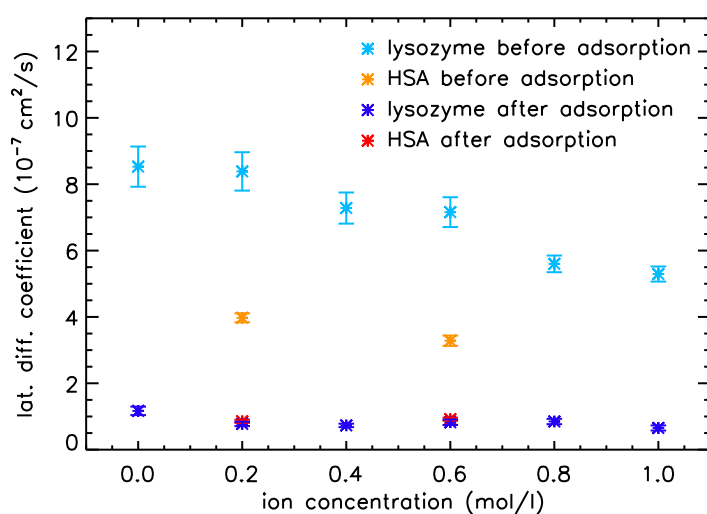

Figure 9.3: Lateral diffusion coefficient of the proteins before the first and after the final adsorption on the solid surface.

9.3.2 Protein Orientation

As lysozyme has an approximately ellipsoidal shape with one well-defined long axis (see Fig. 9.5), its orientation on the solid surface can be described in terms of a single angle γ between the unit vector along this axis (defined by the center of mass of the protein residues 13-59 and 81-155) and the solid surface normal (0,0,1). Values obtained for γ for the different ion concentrations in solution range from $(95 \pm 1)°$ up to $(112 \pm 1)°$, indicating an orientation of lysozyme almost parallel to the solid surface.

For HSA with its heart-shaped conformation (Fig. 9.6), the orientation has been characterized by two angles γ and δ (see Fig. 9.4). The centers of mass of the three main domains of HSA (protein residues 1-197, 198-388, and 389-585 according to the SCOP protein classification [176]) define the three points A, B, and C. γ is defined as the angle between the vector $\vec{bac} = -\vec{AB} + 0.5\vec{AC}$ and the solid surface normal (0,0,1), determining the tilt of the protein with respect to the surface. δ is the angle between the normal vectors of the solid and of the protein. As the values for γ are very different in the individual
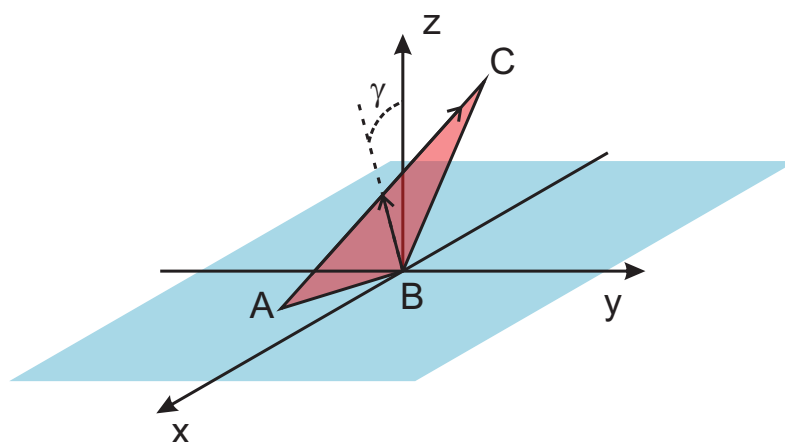
Figure 9.4: Angles and planes characterizing the orientation of HSA (represented by the orange triangle) on the solid surface (blue). The points A, B, and C are defined as the center of masses of the three main domains of the protein. γ is the angle between the vector $\vec{bac} = -\vec{AB} + 0.5\vec{AC}$ and the solid surface normal (0,0,1), determining the tilt of the protein with respect to the surface. δ (not shown) is the angle between the normal vectors of the solid and of the protein, indicating whether the protein faces the surface with the "front" side ($\delta < 90°$) or with the "back" side ($\delta > 90°$).

simulations, they were not averaged, but are listed separately in Table 9.1. Like in the

Conc. (molar)	Name	γ	δ
0.2	2A	74 ± 1	20 ± 1
0.2	2B	97 ± 1	125 ± 1
0.2	2C	44 ± 1	51 ± 1
0.2	2D	104 ± 1	140 ± 1
0.6	6A	117 ± 1	46 ± 1
0.6	6B	36 ± 1	59 ± 1
0.6	6C	81 ± 1	146 ± 1
0.6	6D	96 ± 1	152 ± 1

Table 9.1: Values of the angles characterizing the orientation of HSA on the solid surface for the different simulations.

case of lysozyme, HSA is tilted towards the surface (γ close to $90°$), except for the simulations 2C and 6B. However, in some cases, the protein faces the solid surface with its "front" side ($\delta < 90°$), while in other cases the "back" side is turned towards the surfaces ($\delta > 90°$). Altogether, HSA seems to adsorb with different metastable (on the microsecond timescale) orientations on the solid surface.

To further characterize the adsorbed state of the proteins on the surface, for each amino acid the number of time steps where the minimum distance between the residue and the solid surface was lower than $0.5\,\text{nm}$ has been counted, starting from the time of the final protein adsorption. For both proteins, lysozyme and HSA, residues could be identified that preferentially adsorbed on the surface (see Figs. 9.5 and 9.6). As the solid surface is

negatively charged, these preferentially adsorbing residues are mostly positively charged themselves or in close vicinity to other positively charged residues. However, not all positive charged residues adsorbed frequently, stressing the importance of the protein geometry, as some residues are buried and cannot come close to the solid surface.
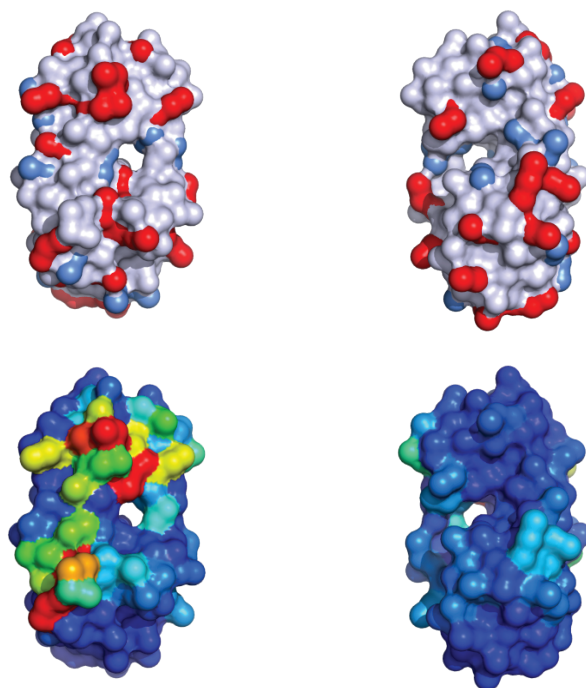

Figure 9.5: Charge distribution (top) and preferentially adsorbing residues (bottom) of lysozyme. The two views on the right and left hand side show the protein from the front and from the back. In the upper panel, positive charged residues are colored red and negative charges are colored blue. In the lower panel, the number of contacts between the protein residues and the solid surface after the final adsorption is color-coded. Blue denotes a small, red a large number of contacts.

9.3.3 Interaction Energies

To control the protein adsorption on solids, it is essential to know the forces driving this process. Therefore, the differences in electrostatic and Lennard Jones energies before the first contact of the protein with the solid surface and after its ultimate adsorption have been calculated for the mutual interactions of the protein, the solvent, and the solid (Table 9.2). Upon adsorption of the proteins on the solid, the electrostatic and Lennard Jones interactions between the protein and the solid increased (negative energy difference), favoring adhesion of the protein on the solid. At the same time, solvent molecules were displaced from the protein and from the solid surface, resulting in decreased interactions (positive energy difference) between the solvent and the solid and the solvent and the protein, counteracting the protein adsorption. But as the solvent molecules released from the solid became now (fully) available for solvent-solvent interactions, these interactions
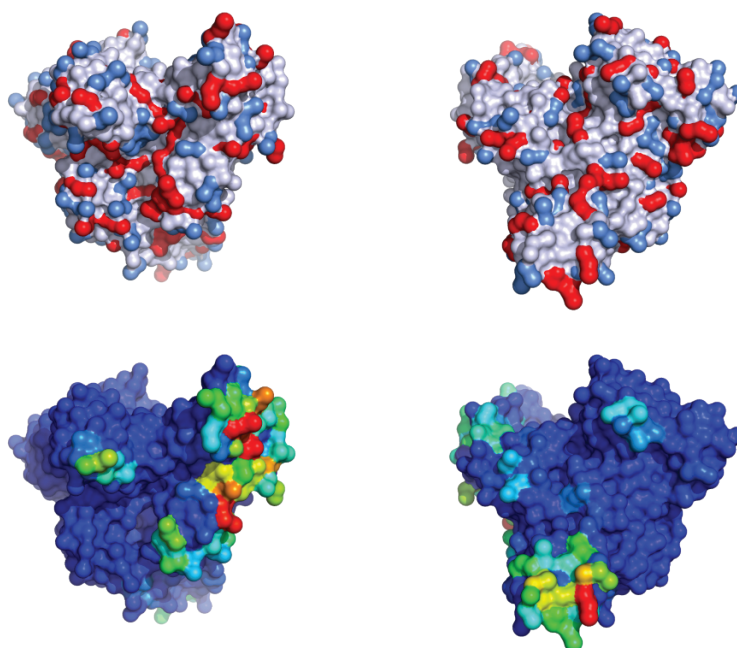
Figure 9.6: Charge distribution (top) and preferentially adsorbing residues (bottom) of HSA. The two views on the right and left hand side show the protein from the front and from the back. In the upper panel, positive charged residues are colored red and negative charges are colored blue. In the lower panel, the number of contacts between the protein residues and the solid surface after the final adsorption is color-coded. Blue denotes a small, red a large number of contacts.

were in turn increased. Electrostatic interactions were always small compared to Lennard Jones contributions. In all simulations, a negative energy difference for the protein-protein interactions was found, indicating some intramolecular rearrangement of protein residues. The sum of all energy contributions is always negative, yielding an enthalpic driving force for the adsorption.

9.3.4 Conformational Changes

Possible surface-induced changes in protein conformation and in internal mobility upon adsorption are an important issue in biotechnological applications as they might be accompanied by a modification or even a loss of protein function. From the observed slight increase in the root mean square deviations (RMSD) of the proteins from their initial structure after the final adsorption on the surface (Table 9.3) and from the increased intramolecular Lennard Jones and electrostatic interactions (Table 9.2), it can be deduced that the proteins slightly change their conformation after adsorption. Please note, that here only small structural rearrangements can be observed, as an unfolding and denaturation of the protein is prevented by the applied harmonic constraints (compare Section 9.2). In order to relate these structural changes to functional motions of the proteins, a principal component analysis (PCA) has been performed and is shown exemplarily for the different

simulations of HSA (Fig. 9.7). The underlying assumption of this technique is that important dynamics within the protein is related to the largest observed fluctuations. Then the directions of the dominant collective motions in, e. g., proteins can be identified by determining the largest eigenvalues and the corresponding eigenvectors of the covariance matrix (after fitting all simulation structures to a reference structure) for the protein (see, e. g., [5]). Here, the overlap

$$\text{overlap}(\mathbf{W}_n, \mathbf{W}_m) = \frac{1}{2} \sum_{s=1}^{2} \sum_{t=1}^{2} (\mathbf{w}_{n,s} \cdot \mathbf{w}_{m,t})^2 \tag{9.1}$$

between the eigenspaces $\mathbf{W}_n$ and $\mathbf{W}_m$ that are spanned by the first two eigenvectors $\mathbf{w}_{n,s}$, $\mathbf{w}_{m,t}$, $\{s,t\} \in \{1,2\}$ (chosen for their distinctly larger eigenvalues compared to the other eigenvectors) of all different $100\,\text{ns}$ time intervals n, m of each individual simulation has been calculated (Fig. 9.7). For all simulations, at least two conformations[2] with differing dominant motions have been found, discernable by the block structure in the plots (Fig. 9.7). Especially well differentiated are the transitions for the simulations C and D at $0.6\,\text{M}$ ion concentration, while the situation is less clear for the simulation A at the same ion concentration. Most conformational changes were observed after the final adsorption of the protein on the surface. Unexpectedly, the changes in the protein dynamics identified by the PCA could not be clearly correlated with simultaneous changes in the protein RMSD or the protein orientation on the solid surface, suggesting that already very subtle structural changes, hardly visible in the RMSD data, can affect the internal dynamics of HSA. Also for lysozyme, changes in the global motions of the protein could be observed, but the transitions between the different states are less clear.

9.4 Summary and Conclusions

In this study, coarse-grained simulations using the MARTINI model [156, 161, 170] have been performed to study the adsorption and adhesion of two proteins, lysozyme and HSA, on a negatively charged solid surface. The experimentally known diffusion coefficient of the proteins in solution has been well reproduced, whereas the lateral diffusion of the proteins adsorbed on the surface was overestimated in the simulations. The deviations of the latter might be due to different properties of the solid (surface) in experiments and simulations, as changes in the surface hydrophobicity and roughness as well as inclusion of multiple solid layers in the simulations are expected to change the diffusion coefficient of the adsorbed proteins. The adhesion of the proteins on the surface was found to be driven by Lennard Jones interactions. For lysozyme, an almost parallel orientation of the protein on the surface has been found, while for HSA several – on the timescales of the simulation – stable orientations were observed. For both proteins, residues adsorbing preferentially on the surface could be identified. Increased RMSD values for the proteins after adsorption pointed to surface-induced conformational changes of the proteins and also internal protein motions were effected by surface-protein interactions.

---

[2]In the notation used here, the conformation of a protein is not only determined by its structure, but also by its internal dynamics.

However, also some limitations of this study should be kept in mind. The solid was modeled by only a monolayer of coarse-grained beads, such that interactions between the bulk solid and the solvent molecules or the proteins have not been taken into account. Besides, the necessary harmonic distance restraints ensuring the stability of the simulated proteins restrict the conformational mobility of the proteins. In this regard, a refinement of the MARTINI model [156, 161, 170], allowing for more flexibility while maintaining the structure of the protein in solution, is certainly needed.

Nevertheless, the application of the MARTINI model [156, 161, 170] allowed for the first time microsecond long simulations to study protein adsorption on solids on a very detailed level and including explicit solvent molecules. In future studies, the properties of the solid surface can be varied to analyze the influence of enthalpic effects on the adsorption process. Simulations at different temperatures or application of forces pulling the proteins away from the surface can be used to estimate entropic contributions. By the accessible timescales within this model, even simulations of multiprotein adsorption become possible, allowing to identify adsorption patterns and to assess the effect of already adsorbed proteins on the adsorption behavior of proteins in solution.

9.5 Acknowledgment

Author Contributions:
Rainer A. Böckmann designed research. The simulations were set up by Beate Griepernau. The analysis was done by Beate Griepernau and in parts by Christian Hanke within the scope of his Bachelor thesis, advised by Beate Griepernau. The article was written by Beate Griepernau and Rainer A. Böckmann.

Conc. (molar)	solid-protein		solid-solvent		protein-protein		protein-solvent		solvent-solvent		total
	C $\left(\frac{kJ}{mol}\right)$	LJ $\left(\frac{kJ}{mol}\right)$	C $\left(\frac{kJ}{mol}\right)$	LJ $\left(\frac{kJ}{mol}\right)$	C $\left(\frac{kJ}{mol}\right)$	LJ $\left(\frac{kJ}{mol}\right)$	C $\left(\frac{kJ}{mol}\right)$	LJ $\left(\frac{kJ}{mol}\right)$	C $\left(\frac{kJ}{mol}\right)$	LJ $\left(\frac{kJ}{mol}\right)$	$\left(\frac{kJ}{mol}\right)$
Lysozyme											
0.0	-20 ± 1	-406 ± 3	1 ± 1	245 ± 4	-6 ± 1	-52 ± 6	3 ± 1	485 ± 7	0 ± 1	-408 ± 10	-160 ± 24
0.2	-17 ± 1	-407 ± 3	2 ± 1	240 ± 4	0 ± 1	-27 ± 5	11 ± 1	468 ± 7	-3 ± 1	-427 ± 9	-159 ± 23
0.4	-20 ± 1	-414 ± 2	5 ± 1	251 ± 4	-6 ± 1	-58 ± 3	22 ± 1	497 ± 5	-10 ± 1	-469 ± 8	-203 ± 35
0.6	-18 ± 1	-345 ± 3	4 ± 1	209 ± 3	-3 ± 1	-41 ± 4	21 ± 1	431 ± 6	-10 ± 1	-431 ± 10	-184 ± 23
0.8	-17 ± 1	-363 ± 3	6 ± 1	223 ± 3	-4 ± 1	-60 ± 3	26 ± 1	477 ± 5	-12 ± 1	-436 ± 8	-160 ± 24
1.0	-18 ± 1	-406 ± 3	9 ± 1	258 ± 3	-13 ± 1	-26 ± 3	39 ± 1	485 ± 6	-23 ± 1	-468 ± 9	-161 ± 21
HSA											
0.2	-16 ± 1	-544 ± 2	0 ± 1	318 ± 4	-21 ± 1	-272 ± 9	24 ± 1	872 ± 10	-7 ± 1	-690 ± 13	-336 ± 61
0.6	-16 ± 1	-600 ± 3	4 ± 1	366 ± 4	-26 ± 1	-157 ± 9	29 ± 2	797 ± 11	-8 ± 1	-789 ± 18	-401 ± 49

Table 9.2.: Differences of Coulomb (C) and Lennard Jones (LJ) energies before the first contact of the protein with the solid surface and after its final adsorption, resolved for the mutual interactions between the protein, the solid, and the solvent (water molecules and ions).

Conc. (molar)	RMSD before the first contact (nm)	RMSD after the final adsorption (nm)
Lysozyme		
0.0	0.43 ± 0.01	0.48 ± 0.01
0.2	0.46 ± 0.01	0.50 ± 0.01
0.4	0.46 ± 0.01	0.48 ± 0.01
0.6	0.44 ± 0.01	0.51 ± 0.01
0.8	0.44 ± 0.01	0.45 ± 0.01
1.0	0.46 ± 0.01	0.48 ± 0.01
HSA		
0.2	0.46 ± 0.01	0.49 ± 0.01
0.6	0.48 ± 0.01	0.48 ± 0.01

Table 9.3: Mean root mean square deviation of the proteins from their initial structure before the first contact of the protein with the solid surface and after their ultimate adsorption.
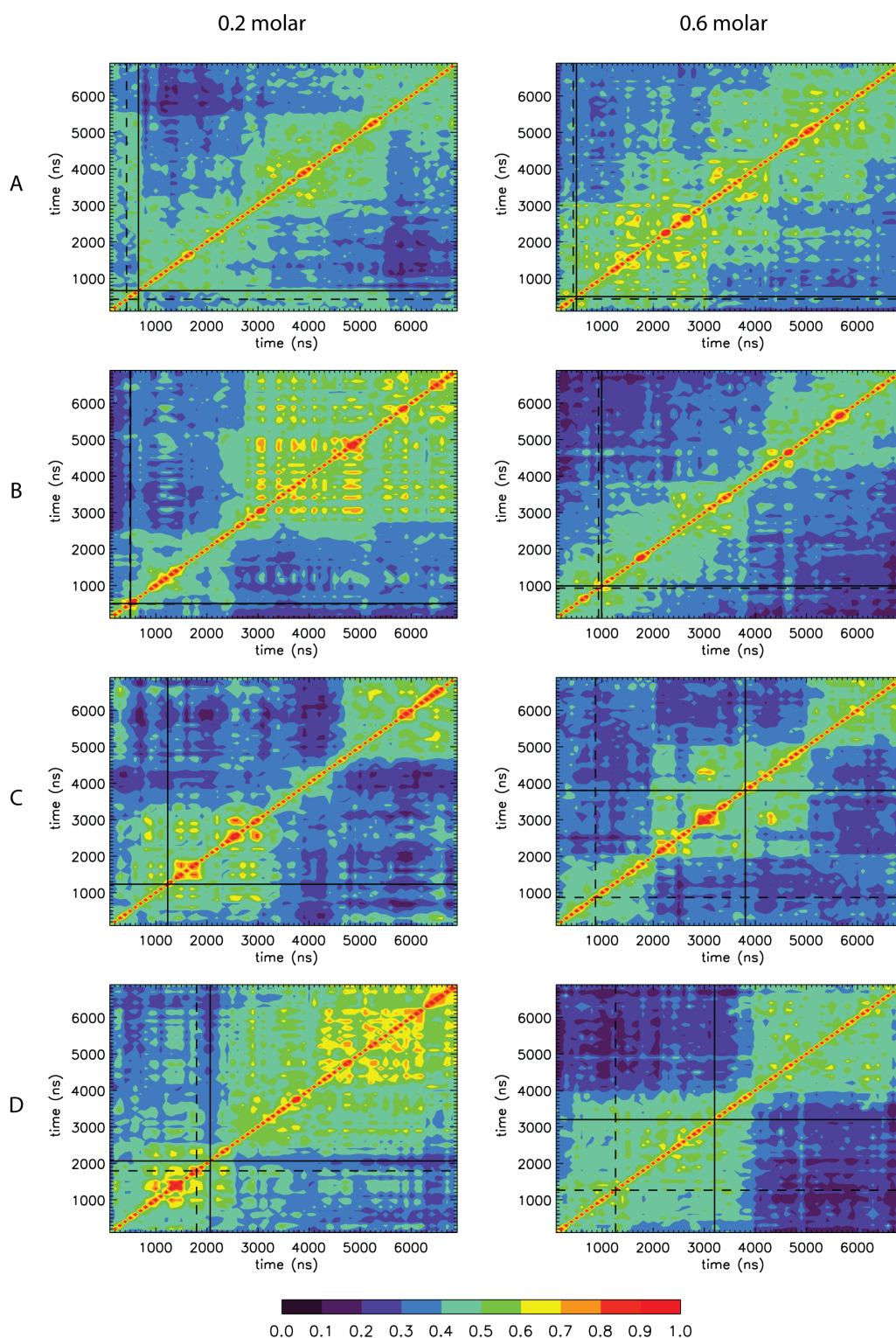
Figure 9.7: Overlap (color-coded) of the eigenspaces, spanned by the two eigenvectors with maximum eigenvalues, between all different 100 ns time intervals for the various HSA simulations. A large overlap of 1.0 (red) indicates that the protein exhibits similar dominant motions in both time intervals, whereas a small overlap of 0.0 (black) points to changed internal dynamics of the protein.

10 Outlook

Within this study, coarse-grained molecular dynamics simulations have been successfully applied to study the adsorption of single proteins on solid surfaces. As discussed in Section 9.4, the model can now be extended to systematically vary the properties of the solid surface, to estimate entropic effects contributing in the adsorption process, and to investigate even multiprotein adsorption. Especially the setup of a multiscale model that allows for a switching between coarse-grained and atomistic simulation would be interesting, as then a fast time evolution of the system in the coarse-grained simulation steps and a high, atomistic resolution of time steps with important dynamics could be achieved at the same time.

On the other hand, also some further development of the model will be necessary. In future studies, not only the solid surface, but multiple solid layers should be included in the simulations in order to take also the interactions of the bulk solid with the adsorbing proteins into account. For the description of these interactions, a larger cutoff radius for Lennard Jones (and electrostatic interactions) should be considered, as an influence of long-range van der Waals forces on the protein adsorption kinetics has been reported [210]. However, care has to be taken to retain the internal consistency of the MARTINI force field. Finally, a refinement of the model permitting full conformational flexibility of the protein, but reproducing its known stability in solution would be desirable. This could maybe be achieved by a selective release of the applied elastic constraints or by a reparametrization of some interactions in the MARTINI force field.

In summary, it can be concluded that coarse-grained molecular dynamics offer new and exciting insights into the complex process of protein adsorption on solid-liquid interfaces and that future studies and refinements of the model can be based on the work presented here.

Bibliography

[1] T. H. Aagaard, M. N. Kristensen, and P. Westh. Packing properties of 1-alkanols and alkanes in a phospholipid membrane. *Biophys. Chem.*, 119:61–68, 2006.

[2] B. J. Alder and T. E. Wainwright. Phase transition for a hard sphere system. *J. Chem. Phys.*, 27:1208–1209, 1957.

[3] B. J. Alder and T. E. Wainwright. Studies in molecular dynamics. I. General method. *J. Chem. Phys.*, 31:459–466, 1959.

[4] M. P. Allen and D. J. Tildesley. *Computer Simulation of Liquids*. Clarendon Press, Oxford, 1987.

[5] A. Amadei, A. B. M. Linssen, and H. J. C. Berendsen. Essential dynamics of proteins. *Proteins: Structure, Function, and Genetics*, 17:412–425, 1993.

[6] S. Andega, N. Kanikkannan, and M. Singh. Comparison of the effect of fatty alcohols on the permeation of melatonin between porcine and human skin. *J. of Contr. Release*, 77:17–25, 2001.

[7] A. S. Arseniev, I. L. Barsukov, V. F. Bystrov, A. L. Lomize, and Y. A. Ovchinnikov. ^{1}H-NMR study of gramicidin A transmembrane ion channel. *FEBS Lett.*, 186:168–174, 1985.

[8] P. W. Atkins and J. de Paula. *Physikalische Chemie*. Wiley-VCH, Weinheim, 4th edition, 2006.

[9] P. Balgavy, M. Dubnickova, N. Kucerka, M. A. Kiselev, S. P. Yaradaikin, and D. Uhrikova. Bilayer thickness and lipid interface area in unilamellar extruded 1,2-diacylphosphatidylcholine liposomes: A small-angle neutron scattering study. *Biochim. Biophys. Acta*, 1512:40–52, 2001.

[10] J. A. Barker and R. O. Watts. Monte Carlo studies of the dielectric properties of water-like models. *Molec. Phys.*, 26:789–792, 1973.

[11] A. J. Barry and K. Gawrisch. Direct NMR evidence for ethanol binding to the lipid–water interface of phospholipid bilayers. *Biochemistry*, 33:8082–8088, 1994.

[12] M. D. Becker, D. V. Greathouse, R. E. Koeppe, and O. S. Andersen. Amino acid sequence modulation of gramicidin channel function: Effects of tryptophan-to-phenylalanine substitutions on the single-channel conductance and duration. *Biochemistry*, 30:8830–8839, 1991.

[13] M. Bellion, L. Santen, H. Mantz, H. Hähl, A. Quinn, A. Nagel, C. Gilow, C. Weitenberg, Y. Schmitt, and K. Jacobs. Protein adsorption on tailored substrates: Long-range forces and conformational changes. *J. Phys.: Condens. Matter*, 20:404226, 2008.

[14] H. J. C. Berendsen. *Simulating the Physical World*. Cambridge University Press, Cambridge, 2007.

[15] H. J. C. Berendsen, J. R. Grigera, and T. P. Straatsma. The missing term in effective pair potentials. *J. Phys. Chem.*, 91:6269–6271, 1987.

[16] H. J. C. Berendsen, J. P. M. Postma, W. F. van Gunsteren, A. DiNola, and J. R. Haak. Molecular dynamics with coupling to an external bath. *J. Chem. Phys.*, 81:3684–3690, 1984.

[17] H. J. C. Berendsen, J. P. M. Postma, W. F. van Gunsteren, and J. Hermans. Interaction model for water in relation to protein hydration. In B. Pullman, editor, *Intermolecular Forces*, pages 331–342, Dordrecht, The Netherlands, 1981. D. Reidel Publishing Company.

[18] H. J. C. Berendsen, D. van der Spoel, and R. van Drunen. GROMACS: A message-passing parallel molecular dynamics implementation. *Comp. Phys. Comm.*, 91:43–56, 1995.

[19] J. M. Berg, J. L. Tymoczko, and L. Stryer. *Biochemie*. Spektrum Akademischer Verlag, Heidelberg/Berlin, 5th edition, 2003.

[20] O. Berger, O. Edholm, and F. Jähnig. Molecular dynamics simulations of a fluid bilayer of dipalmitoylphosphatidylcholine at full hydration, constant pressure, and constant temperature. *Biophys. J.*, 72:2002–2013, 1997.

[21] H. M. Berman, K. Henrick, and H. Nakamura. Announcing the worldwide protein data bank. *Nat. Struct. Biol.*, 10:980–980, 2003.

[22] D. Boal. *Mechanics of the Cell*. Cambridge University Press, Cambridge, 2002.

[23] R. A. Böckmann and H. Grubmüller. Nanoseconds molecular dynamics simulation of primary mechanical energy transfer steps in F_1-ATP synthase. *Nat. Struct. Biol.*, 9:198–202, 2002.

[24] R. A. Böckmann, A. Hac, T. Heimburg, and H. Grubmüller. Effect of sodium chloride on a lipid bilayer. *Biophys. J.*, 85:1647–1655, 2003.

[25] P. J. Bond, J. Holyoake, A. Ivetac, S. Khalid, and M. S. P. Sansom. Coarse-grained molecular dynamics simulations of membrane proteins and peptides. *J. Struct. Biol.*, 157:593–605, 2007.

[26] P. J. Bond and M. S. P. Sansom. Insertion and assembly of membrane proteins via simulation. *J. Am. Chem. Soc.*, 128:2697–2704, 2006.

[27] P. J. Bond and M. S. P. Sansom. Bilayer deformation by the Kv channel voltage sensor domain revealed by self-assembly simulations. *Proc. Natl. Acad. Sci. USA*, 104:2631–2636, 2007.

[28] M. Born and R. Oppenheimer. Zur Quantentheorie der Molekeln. *Ann. Phys.*, 84:457–484, 1927.

[29] B. R. Brooks, R. E. Bruccoleri, B. D. Olafson, D. J. States, S. Swaminathan, and M. Karplus. CHARMM: A program for macromolecular energy, minimization, and dynamics calculations. *J. Comp. Chem.*, 4:187–217, 1983.

[30] G. Büldt, H. U. Gally, A. Seelig, and J. Seelig. Neutron diffraction studies on selectively deuterated phospholipid bilayers. *Nature*, 271:182–184, 1978.

[31] G. Büldt, H. U. Gally, and J. Seelig. Neutron diffraction studies on phosphatidylcholine model membranes: I. Head group conformation. *J. Molec. Biol.*, 134:673–691, 1979.

[32] B. M. Burkhart, N. Li, D. A. Langs, W. A. Pangborn, and W. L. Duax. The conducting form of gramicidin A is a right-handed double-stranded double helix. *Proc. Natl. Acad. Sci. USA*, 95:12950–12955, 1998.

[33] R. S. Cantor. The lateral pressure profile in membranes: A physical mechanism of general anesthesia. *Biochemistry*, 36:2339–2344, 1997.

[34] R. S. Cantor. Lateral pressures in cell membranes: A mechanism for modulation of protein function. *J. Phys. Chem. B*, 101:1723–1725, 1997.

[35] R. S. Cantor. The lateral pressure profile in membranes: A physical mechanism of general anesthesia. *Toxicology Letters*, 100-101:451–458, 1998.

[36] R. S. Cantor. The influence of membrane lateral pressures on simple geometric models of protein conformational equilibria. *Chem. Phys. Lipids*, 101:45–56, 1999.

[37] R. S. Cantor. Lipid composition and the lateral pressure profile in bilayers. *Biophys. J.*, 76:2625–2639, 1999.

[38] R. S. Cantor. Size distribution of barrel-stave aggregates of membrane peptides: Influence of the bilayer lateral pressure profile. *Biophys. J.*, 82:2520–2525, 2002.

[39] A. Carnini, T. T. Nguyen, and D. T. Cramb. Fluorescence quenching of gramicidin D in model membranes by halothane. *Can. J. Chem.*, 85:513–519, 2007.

[40] M. Carrillo-Tripp and S. E. Feller. Evidence for a mechanism by which $\omega - 3$ polyunsaturated lipids may affect membrane protein function. *Biochemistry*, 44:10164–10169, 2005.

[41] J. Chanda and S. Bandyopadhyay. Distribution of ethanol in a model membrane: a computer simulation study. *Chem. Phys. Lett.*, 392:249–254, 2004.

[42] J. Chanda and S. Bandyopadhyay. Perturbation of phospholipid bilayer properties by ethanol at a high concentration. *Langmuir*, 22:3775–3781, 2006.

[43] S.-Y. Chen, B. Yang, K. Jacobson, and K. K. Sulik. The membrane disordering effect of ethanol on neural crest cells in vitro and the protective role of GM1 ganglioside. *Alcohol*, 13:589–595, 1996.

[44] J. H. Chin and D. B. Goldstein. Effects of low concentrations of ethanol on the fluidity of spin-labeled erythrocyte and brain membranes. *Mol. Pharmacol.*, 13:435–441, 1977.

[45] S. W. Chiu, M. Clark, V. Balaji, S. Subramaniam, H. L. Scott, and E. Jakobsson. Incorporation of surface tension into molecular dynamics simulation of an interface: A fluid phase lipid bilayer membrane. *Biophys. J.*, 69:1230–1245, 1995.

[46] B. Cornell. Gramicidin A–phospholipid model systems. *J. Bioener. Biomem.*, 19:655–676, 1987.

[47] W. D. Cornell, P. Cieplak, C. I. Bayly, I. R. Gould, K. M. Merz, D. M. Ferguson, D. C. Spellmeyer, T. Fox, J. W. Caldwell, and P. A. Kollman. A second generation force field for the simulation of proteins, nucleic acids, and organic molecules. *J. Am. Chem. Soc.*, 117:5179–5197, 1995.

[48] C. Czeslik. Factors ruling protein adsorption. *Z. Phys. Chem.*, 218:771–801, 2004.

[49] C. Czeslik. Proteinadsorption an festen Grenzflächen. *Chem. Unserer Zeit*, 40:238–245, 2006.

[50] T. Darden, D. York, and L. Pedersen. Particle mesh Ewald — An $N \log(N)$ method for Ewald sums in large systems. *J. Chem. Phys.*, 98:10089–10092, 1993.

[51] L. A. Davies, M. L. Klein, and D. Scharf. Molecular dynamics simulation of a synthetic four-α-helix bundle that binds the anesthetic halothane. *FEBS Lett.*, 455:332–338, 1999.

[52] L. A. Davies, Q. Zhong, M. L. Klein, and D. Scharf. Molecular dynamics simulation of four-α-helix bundles that bind the anesthetic halothane. *FEBS Lett.*, 478:61–66, 2000.

[53] B. L. de Groot and H. Grubmüller. Water permeation across biological membranes: Mechanism and dynamics of Aquaporin-1 and GlpF. *Science*, 294:2353–2357, 2001.

[54] B. L. de Groot, S. Hayward, D. M. F. van Aalten, A. Amadei, and H. J. C. Berendsen. Domain motions in bacteriophage T4 lysozyme: A comparison between molecular dynamics and crystallographic data. *Proteins: Structure, Function, and Genetics*, 31:116–127, 1998.

[55] P. S. de Laplace. *A Philosophical Essay on Probabilities*. Dover, New York, 1951.

[56] A. H. de Vries, S. Yefimov, A. E. Mark, and S. J. Marrink. Molecular structure of the lecithin ripple phase. *Proc. Natl. Acad. Sci. USA*, 102:5392–5396, 2005.

[57] W. K. den Otter and W. J. Briels. The bending rigidity of an amphiphilic bilayer from equilibrium and nonequilibrium molecular dynamics. *J. Chem. Phys.*, 118:4712–4720, 2003.

[58] R. Dickinson, I. White, W. R. Lieb, and N. P. Franks. Stereoselective loss of righting reflex in rats by isoflurane. *Anesthesiology*, 93:837–843, 2000.

[59] C. Dietrich and R. Tampe. Charge determination of membrane molecules in polymer-supported lipid layers. *Biochim. Biophys. Acta*, 1238:183–191, 1995.

[60] Y. Duan and P. A. Kollman. Pathways to a protein folding intermediate observed in a 1-microsecond simulation in aqueous solution. *Science*, 282:740–744, 1998.

[61] S. B. Dubin, N. A. Clark, and G. B. Benedek. Measurement of the rotational diffusion coefficient of lysozyme by depolarized light scattering: Configuration of lysozyme in solution. *J. Chem. Phys.*, 54:5158–5164, 1971.

[62] O. Edholm and J. F. Nagle. Areas of molecules in membranes consisting of mixtures. *Biophys. J.*, 89:1827–1832, 2005.

[63] E. I. Eger, D. D. Koblin, M. J. Laster, V. Schurig, M. Juza, P. Ionescu, and D. Gong. Minimum alveolar anesthetic concentration values for the enantiomers of isoflurane differ minimally. *Anesth. Analg.*, 85:188–192, 1997.

[64] J. Eisenblätter and R. Winter. Pressure effects on the structure and phase behaviour of DMPC-gramicidin lipid bilayers: A synchrotron SAXS and ^{2}H-NMR spectroscopy study. *Biophys. J.*, 90:956–966, 2006.

[65] E. Evans and W. Rawicz. Entropy-driven tension and bending elasticity in condensed-fluid membranes. *Phys. Rev. Lett.*, 64:2094–2097, 1990.

[66] E. A. Evans. Bending resistance and chemically induced moments in membrane bilayers. *Biophys. J.*, 14:923–931, 1974.

[67] W. H. Evans and J. M. Graham. *Struktur und Funktion biologischer Membranen*. Georg Thieme Verlag, Stuttgart, 1991.

[68] P. P. Ewald. Die Berechnug optischer und elektrostatischer Gitterpotentiale. *Ann. Phys.*, 369:253–287, 1921.

[69] M. T. Facciotti, S. Rouhani, F. T. Burkard, F. M. Betancourt, K. H. Downing, R. B. Rose, G. McDermott, and R. M. Glaeser. Structure of an early intermediate in the M-state phase of the bacteriorhodopsin photocycle. *Biophys. J.*, 81:3442–3455, 2001.

[70] R. Faller and S. J. Marrink. Simulation of domain formation in DLPC-DSPC mixed bilayers. *Langmuir*, 20:7686–7693, 2004.

[71] S. E. Feller, C. A. Brown, D. T. Nizza, and K. Gawrisch. Nuclear Overhauser enhancement spectroscopy cross-relaxation rates and ethanol distribution across membranes. *Biophys. J.*, 82:1396–1404, 2002.

[72] S. E. Feller and R. W. Pastor. Constant surface tension simulations of lipid bilayers: The sensitivity of surface areas and compressibilities. *J. Chem. Phys.*, 111:1281–1287, 1999.

[73] A. Filippov, G. Orädd, and G. Lindblom. The effect of cholesterol on the lateral diffusion of phospholipids in oriented bilayers. *Biophys. J.*, 84:3079–3086, 2003.

[74] L. L. Firestone, J. K. Alifimoff, T. Humphreys, and K. W. Miller. Anesthetic optical isomers are equipotent in desensitizing acetylcholine receptors. *Anesthesiology*, 69:A638, 1988.

[75] S. Firestone, C. Ferguson, and L. Firestone. Isoflurane's optical isomers are equipotent in rana pipiens tadpole. *Anesthesiology*, 77:A758, 1992.

[76] D. Forst, W. Welte, T. Wacker, and K. Diederichs. Structure of the sucrose-specific porin ScrY from salmonella typhimurium and its complex with sucrose. *Nat. Struct. Biol.*, 5:37–46, 1998.

[77] N. P. Franks. General anaesthesia: From molecular targets to neuronal pathways of sleep and arousal. *Nat. Rev. Neuroscience*, 9:370–386, 2008.

[78] N. P. Franks and W. R. Lieb. Do general anaesthetics act by competitive binding to specific receptors? *Nature*, 310:599–601, 1984.

[79] N. P. Franks and W. R. Lieb. Partitioning of long-chain alcohols into lipid bilayers: Implications for mechanisms of general anesthesia. *Proc. Natl. Acad. Sci. USA*, 83:5116–5120, 1986.

[80] N. P. Franks and W. R. Lieb. Stereospecific effects of inhalational general anesthetic optical isomers on nerve ion channels. *Science*, 254:427–430, 1991.

[81] N. P. Franks and W. R. Lieb. Molecular and cellular mechanisms of general anaesthesia. *Nature*, 367:607–614, 1994.

[82] P. L. Freddolino, A. S. Arkhipov, S. B. Larson, A. McPherson, and K. Schulten. Molecular dynamics simulations of the complete satellite tobacco mosaic virus. *Structure*, 14:437–449, 2006.

[83] A. L. Frischknecht and L. J. Douglas Frink. Alcohols reduce lateral membrane pressures: Predictions from molecular theory. *Biophys. J.*, 91:4081–4090, 2006.

[84] R. Goetz, G. Gompper, and R. Lipowsky. Mobility and elasticity of self-assembled membranes. *Phys. Rev. Lett.*, 82:221–224, 1999.

[85] R. Goetz and R. Lipowsky. Computer simulations of bilayer membranes: Self-assembly and interfacial tension. *J. Chem. Phys.*, 108:7397–7409, 1998.

[86] J. J. Gray. The interaction of proteins with solid surfaces. *Curr. Opin. Struct. Biol.*, 14:110–115, 2004.

[87] J. J. Gray and R. T. Bonnecaze. Adsorption of colloidal particles by Brownian dynamics simulation: Kinetics and surface structures. *J. Chem. Phys.*, 114:1366–1381, 2001.

[88] B. Griepernau and R. A. Böckmann. The influence of 1-alkanols and external pressure on the lateral pressure profiles of lipid bilayers. *Biophys. J.*, 95:5766–5778, 2008.

[89] B. Griepernau, S. Leis, M. F. Schneider, M. Sikor, D. Steppich, and R. A. Böckmann. 1-alkanols and membranes: A story of attraction. *Biochim. Biophys. Acta*, 1768:2899–2913, 2007.

[90] J. Gullingsrud, A. Babakhani, and J. A. McCammon. Computational investigation of pressure profiles in lipid bilayers with embedded proteins. *Molec. Sim.*, 32:831–838, 2006.

[91] J. Gullingsrud and K. Schulten. Lipid bilayer pressure profiles and mechanosensitive channel gating. *Biophys. J.*, 86:3496–3509, 2004.

[92] A. A. Gurtovenko, M. Patra, M. Karttunen, and I. Vattulainen. Cationic DMPC/DMTAP lipid bilayers: Molecular dynamics study. *Biophys. J.*, 86:3461–3472, 2004.

[93] M. J. Halsey and B. Wardley-Smith. Pressure reversal of narcosis produced by anaesthetics, narcotics and tranquillisers. *Nature*, 257:811–813, 1975.

[94] A. Harasima. Molecular theory of surface tension. *Adv. Chem. Phys.*, 1:203–237, 1958.

[95] D. Harries and A. Ben-Shaul. Conformational chain statistics in a model lipid bilayer: Comparison between mean field and Monte Carlo calculations. *J. Chem. Phys.*, 106:1609–1619, 1997.

[96] B. Harris, E. Moody, and P. Skolnick. Isoflurane anesthesia is stereoselective. *Europ. J. of Pharmacology*, 217:215–216, 1992.

[97] H. Heerklotz and J. Seelig. Application of pressure perturbation calorimetry to lipid bilayers. *Biophys. J.*, 82:1445–1452, 2002.

[98] T. Heimburg. *Thermal Biophysics of Membranes*. Wiley-VCH, Weinheim, 2007.

[99] T. Heimburg and A. D. Jackson. On soliton propagation in biomembranes and nerves. *Proc. Natl. Acad. Sci. USA*, 102:9790–9795, 2005.

[100] T. Heimburg and A. D. Jackson. On the action potential as a propagating density pulse and the role of anesthetics. *Biophys. Rev. Lett.*, 2:57–78, 2007.

[101] T. Heimburg and A. D. Jackson. The thermodynamics of general anesthesia. *Biophys. J.*, 92:3159–3165, 2007.

[102] H. Heinz, W. Paul, and K. Binder. Calculation of local pressure tensors in systems with many-body interactions. *Phys. Rev. E*, 72:066704, 2005.

[103] W. Helfrich. Elastic properties of lipid bilayers: Theory and possible experiments. *Z. Naturforsch.*, 28c:693–703, 1973.

[104] B. Hess. Similarities between principal components of protein dynamics and random diffusion. *Phys. Rev. E*, 62:8438–8448, 2000.

[105] B. Hess. Convergence of sampling in protein simulations. *Phys. Rev. E*, 65:031910, 2002.

[106] B. Hess, H. Bekker, H. J. C. Berendsen, and J. G. E. M. Fraaije. LINCS: A linear constraint solver for molecular simulations. *J. Comp. Chem.*, 18:1463–1472, 1997.

[107] R. W. Hockney. The potential calculation and some applications. *Meth. Comput. Phys.*, 9:136–211, 1970.

[108] A. L. Hodgkin and A. F. Huxley. A quantitative description of membrane current and its application to conduction and excitation in nerve. *J. of Physiol.*, 117:500–544, 1952.

[109] C.-J. Högberg and A. P. Lyubartsev. A molecular dynamics investigation of the influence of hydration and temperature on structural and dynamical properties of a dimyristoylphosphatidylcholine bilayer. *J. Phys. Chem. B*, 110:14326–14336, 2006.

[110] L. L. Holte and K. Gawrisch. Determining ethanol distribution in phospholipid multilayers with MAS–NOESY spectra. *Biochemistry*, 36:4669–4674, 1997.

[111] T. Huber, A. E. Torda, and W. F. van Gunsteren. Structure optimization combining soft-core interaction functions, the diffusion equation method, and molecular dynamics. *J. Phys. Chem. A*, 101:5926–5930, 1997.

[112] H. Ichimori, T. Hata, H. Matsuki, and S. Kaneshina. Barotropic phase transitions and pressure-induced interdigitation on bilayer membranes of phospholipids with varying acyl chain lengths. *Biochim. Biophys. Acta*, 1414:165–174, 1998.

[113] H. Ichimori, T. Hata, T. Yoshioka, H. Matsuki, and S. Kaneshina. Thermotropic and barotropic phase transition on bilayer membranes of phospholipids with varying acyl chain-lengths. *Chem. Phys. Lipids*, 89:97–105, 1997.

[114] M. O. Jensen and O. G. Mouritsen. Lipids do influence protein function — the hydrophobic matching hypothesis revisited. *Biochim. Biophys. Acta*, 1666:205–226, 2004.

[115] F. H. Johnson, D. Brown, and D. Marsland. A basic mechanism in the biological effects of temperature, pressure and narcotics. *Science*, 95:200–203, 1942.

[116] F. H. Johnson and E. A. Flagler. Hydrostatic pressure reversal of narcosis in tadpoles. *Science*, 112:91–92, 1950.

[117] W. L. Jorgensen, J. Chandrasekhar, and J. D. Madura. Comparison of simple potential functions for simulating liquid water. *J. Chem. Phys.*, 79:926–935, 1983.

[118] W. L. Jorgensen, D. S. Maxwell, and J. Tirado-Rives. Development and testing of the OPLS all-atom force field on conformational energetics and properties of organic liquids. *J. Am. Chem. Soc.*, 118:11225–11236, 1996.

[119] W. L. Jorgensen and J. Tirado-Rives. The OPLS [optimized potentials for liquid simulations] potential functions for proteins, energy minimizations for crystals of cyclic peptides and crambin. *J. Am. Chem. Soc.*, 110:1657–1666, 1988.

[120] H. Kamaya, N. Matubayasi, and I. Ueda. Biphasic effect of long-chain n-alkanols on the main phase transition of phospholipid vesicle membranes. *J. Phys. Chem.*, 88:797–800, 1984.

[121] T. Kamo, M. Nakano, Y. Kuroda, and T. Handa. Effects of an amphipathic α-helical peptide on lateral pressure and water penetration in phosphatidylcholine and monoolein mixed membranes. *J. Phys. Chem. B*, 110:24987–24992, 2006.

[122] B. Kasemo. Biological surface science. *Surface Science*, 500:656–677, 2002.

[123] D. A. Kelkar and A. Chattopadhyay. The gramicidin ion channel: A model membrane protein. *Biochim. Biophys. Acta*, 1768:2011–2025, 2007.

[124] J. J. Kendig, J. R. Trudell, and E. N. Cohen. Halothane stereoisomers: Lack of stereospecificity in two model systems. *Anesthesiology*, 39:518–524, 1973.

[125] R. R. Ketchem, W. Hu, and T. A. Cross. High-resolution conformation of gramicidin A in a lipid bilayer by solid-state NMR. *Science*, 261:1457–1460, 1993.

[126] R. R. Ketchem, K.-C. Lee, S. Huo, and T. A. Cross. Macromolecular structural elucidation with solid-state NMR-derived orientational constraints. *J. Biomol. NMR*, 8:1–14, 1996.

[127] R. R. Ketchem, K. C. Lee, S. Huo, and T. A. Cross. Macromolecular structural elucidation with solid-state NMR-derived orientational constraints. *J. Biomol. NMR*, 8:1–14, 1996.

[128] J. A. Killian. Gramicidin and gramicidin-lipid interactions. *Biochim. Biophys. Acta*, 1113:391–425, 1992.

[129] S. Kirkpatrick, C. D. Gelatt, and M. P. Vecchi. Optimization by simulated annealing. *Science*, 220:671–680, 1983.

[130] B. W. Koenig and K. Gawrisch. Lipid-ethanol interaction studied by NMR on bicelles. *J. Phys. Chem. B*, 109:7540–7547, 2005.

[131] L. Koubi, M. Tarek, M. L. Klein, and D. Scharf. Distribution of halothane in a dipalmitoylphosphatidylcholine bilayer from molecular dynamics calculations. *Biophys. J.*, 78:800–811, 2000.

[132] M. Kranenburg, C. Laforge, and B. Smit. Mesoscopic simulations of phase transitions in lipid bilayers. *Phys. Chem. Chem. Phys.*, 6:4531–4534, 2004.

[133] M. Kranenburg and B. Smit. Simulating the effect of alcohol on the structure of a membrane. *FEBS Lett.*, 568:15–18, 2004.

[134] M. Kranenburg, M. Vlaar, and B. Smit. Simulating induced interdigitation in membranes. *Biophys. J.*, 87:1596–1605, 2004.

[135] G. Kreienbühl. Charles Ernest Overton: Studien über die Narkose (1901). Ein beinahe vergessener Pionier der Narkosetheorie. In T. Pasch, E. R. Schmid, and A. Zollinger, editors, *Anästhesie in Zürich: 100 Jahre Entwicklung 1901-2001*, pages 10–14, 2001.

[136] N. Kucerka, Y. Liu, N. Chu, H. I. Petrache, S. Tristram-Nagle, and J. F. Nagle. Structure of fully hydrated fluid phase DMPC and DLPC lipid bilayers using X-ray scattering from oriented multilamellar arrays and from unilamellar vesicles. *Biophys. J.*, 88:2626–2637, 2005.

[137] A. G. Lee. Interactions between anesthetics and lipid mixtures. Normal alcohols. *Biochemistry*, 15:2448–2454, 1976.

[138] S. Leekumjorn and A. K. Sum. Molecular studies of the gel to liquid-crystalline phase transition for fully hydrated DPPC and DPPE bilayers. *Biochim. Biophys. Acta*, 1768:354–365, 2007.

[139] M. J. Lever, K. W. Miller, W. D. M. Paton, and E. B. Smith. Pressure reversal of anaesthesia. *Nature*, 231:368–371, 1971.

[140] B. A. Lewis and D. M. Engelman. Lipid bilayer thickness varies linearly with acyl chain length in fluid phophatidylcholine vesicles. *J. Molec. Biol.*, 166:211–217, 1983.

[141] E. Lindahl and O. Edholm. Mesoscopic undulations and thickness fluctuations in lipid bilayers from molecular dynamics simulations. *Biophys. J.*, 79:426–433, 2000.

[142] E. Lindahl and O. Edholm. Spatial and energetic-entropic decomposition of surface tension in lipid bilayers from molecular dynamics simulations. *J. Chem. Phys.*, 113:3882–3893, 2000.

[143] E. Lindahl, B. Hess, and D. van der Spoel. GROMACS 3.0: A package for molecular simulation and trajectory analysis. *J. Mol. Model.*, 7:306–317, 2001.

[144] R. Lipowsky and E. Sackmann, editors. *Handbook of Biological Physics*. Elsevier Science B.V., 1995.

[145] Z. Liu, Y. Xu, and P. Tang. Molecular dynamics simulations of C_2F_6 effects on gramicidin A: Implications of the mechanisms of general anesthesia. *Biophys. J.*, 88:3784–3791, 2005.

[146] Z. Liu, Y. Xu, and P. Tang. Steered molecular dynamics simulations of Na^+ permeation across the gramicidin A channel. *J. Phys. Chem. B*, 110:12789–12795, 2006.

[147] J. A. Lundbaek. Regulation of membrane protein function by lipid bilayer elasticity – a single molecule technology to measure the bilayer properties experienced by an embedded protein. *J. Phys.: Condens. Matter*, 18:S1305–S1344, 2006.

[148] H. V. Ly, D. E. Block, and M. L. Longo. Interfacial tension effect of ethanol on lipid bilayer rigidity, stability and area/molecule: A micropipet aspiration approach. *Langmuir*, 18:8988–8995, 2002.

[149] H. V. Ly and M. L. Longo. The influence of short-chain alcohols on interfacial tension, mechanical properties, area/molecule, and permeability of fluid lipid bilayers. *Biophys. J.*, 87:1013–1033, 2004.

[150] G. S. Lysko, J. L. Robinson, R. Casto, and R. A. Ferrone. The stereospecific effects of isoflurane isomers in vivo. *Europ. J. of Pharmacology*, 263:25–29, 1994.

[151] J. L. MacCallum and D. P. Tieleman. Structures of neat and hydrated 1-octanol from computer simulations. *J. Am. Chem. Soc.*, 124:15085–15093, 2002.

[152] A. D. MacKerell, D. Bashford, M. Bellott, R. L. Dunbrack, J. D. Evanseck, M. J. Field, S. Fischer, J. Gao, H. Guo, S. Ha, D. Joseph-McCarthy, L. Kuchnir, K. Kuczera, F. T. K. Lau, C. Mattos, S. Michnick, T. Ngo, D. T. Nguyen, B. Prodhom, W. E. Reiher, B. Roux, M. Schlenkrich, J. C. Smith, R. Stote, J. Straub, M. Watanabe, J. Wiorkiewicz-Kuczera, D. Yin, and M. Karplus. All-atom empirical potential for molecular modeling and dynamics studies of proteins. *J. Phys. Chem. B*, 102:3586–3616, 1998.

[153] A. D. MacKerell, J. Wiorkiewicz-Kuczera, and M. Karplus. An all-atom empirical energy function for the simulation of nucleic acids. *J. Am. Chem. Soc.*, 117:11946 – 11975, 1995.

[154] M. Malmsten. Formation of adsorbed protein layers. *J. of Colloid and Interface Science*, 207:186–199, 1998.

[155] B. Mao and A. R. Friedman. Molecular dynamics simulation by atomic mass weighting. *Biophys. J.*, 58:803–805, 1990.

[156] S. J. Marrink, A. H. de Vries, and A. E. Mark. Coarse grained model for semiquantitative lipid simulations. *J. Phys. Chem. B*, 108:750–760, 2004.

[157] S. J. Marrink, E. Lindahl, O. Edholm, and A. E. Mark. Simulation of spontaneous aggregation of phospholipids into bilayers. *J. Am. Chem. Soc.*, 123:8638–8639, 2001.

[158] S. J. Marrink and A. E. Mark. Effect of undulations on surface tension in simulated bilayers. *J. Phys. Chem. B*, 105:6122–6127, 2001.

[159] S. J. Marrink and A. E. Mark. Molecular dynamics simulation of the formation, structure and dynamics of small phospholipid vesicles. *J. Am. Chem. Soc.*, 125:15233–15242, 2003.

[160] S. J. Marrink and A. E. Mark. Molecular view of hexagonal phase formation in phospholipid membranes. *Biophys. J.*, 87:3894–3900, 2004.

[161] S. J. Marrink, H. J. Risselada, S. Yefimov, D. P. Tieleman, and A. H. de Vries. The MARTINI force field: Coarse grained model for biomolecular simulations. *J. Phys. Chem. B*, 111:7812–7824, 2007.

[162] S. J. Marrink, J. Risselada, and A. E. Mark. Simulation of gel phase formation and melting in lipid bilayers using a coarse grained model. *Chem. Phys. Lipids*, 135:223–244, 2005.

[163] D. Marsh. Lateral pressure in membranes. *Biochim. Biophys. Acta*, 1286:183–223, 1996.

[164] J. A. McCammon, B. R. Gelin, and M. Karplus. Dynamics of folded proteins. *Nature*, 267:585–590, 1977.

[165] H. Meyer. Zur Theorie der Alkoholnarkose. *Arch. Exp. Path. Pharmakol. (Naunyn-Schmiedeberg)*, 42:109–118, 1899.

[166] K. W. Miller, W. D. M. Paton, R. A. Smith, and E. B. Smith. The pressure reversal of general anesthesia and the critical volume hypothesis. *Mol. Pharmacol.*, 9:131–143, 1973.

[167] S. L. Miller. A theory of gaseous anesthetics. *Proc. Natl. Acad. Sci. USA*, 47:1515–1524, 1961.

[168] A. Mitsutake, Y. Sugita, and Y. Okamoto. Generalized-ensemble algorithms for molecular simulations of biopolymers. *Biopolymers*, 60:96–123, 2001.

[169] S. Miyamoto and P. A. Kollman. SETTLE: An analytical version of the SHAKE and RATTLE algorithm for rigid water models. *J. Comp. Chem.*, 13:952–962, 1992.

[170] L. Monticelli, S. K. Kandasamy, X. Periole, R. G. Larson, D. P. Tieleman, and S. J. Marrink. The MARTINI coarse-grained force field: Extensions to proteins. *J. Chem. Theory Comp.*, 4:819–834, 2008.

[171] E. J. Moody, B. D. Harris, and P. Skolnick. Stereospecific actions of the inhalation anesthetic isoflurane at the GABA$_A$ receptor complex. *Brain Research*, 615:101–106, 1993.

[172] S. I. Mukhin and S. Baoukina. Analytical derivation of thermodynamic characteristics of lipid bilayer from a flexible string model. *Phys. Rev. E*, 71:061918, 2005.

[173] P. A. Mulheran, D. Pellenc, R. A. Bennett, R. J. Green, and M. Sperrin. Mechanisms and dynamics of protein clustering on a solid surface. *Phys. Rev. Lett.*, 100:068102, 2008.

[174] M. Müller, K. Katsov, and M. Schick. Biological and synthetic membranes: What can be learned from a coarse-grained description? *Phys. Rep.*, 434:113–176, 2006.

[175] L. J. Mullins. Some physical mechanisms in narcosis. *Chem. Rev.*, 54:289–323, 1954.

[176] A. G. Murzin, S. E. Brenner, T. Hubbard, and C. Chothia. SCOP: A structural classification of proteins database for the investigation of sequences and structures. *J. Molec. Biol.*, 247:536–540, 1995.

[177] J. F. Nagle and S. Tristram-Nagle. Structure of lipid bilayers. *Biochim. Biophys. Acta*, 1469:159–195, 2000.

[178] J. F. Nagle and D. A. Wilkinson. Lecithin bilayers. Density measurement and molecular interactions. *Biophys. J.*, 23:159–175, 1978.

[179] M. Neumann. Dipole moment fluctuation formulas in computer simulations of polar systems. *Molec. Phys.*, 50:841–858, 1983.

[180] A. A. Nevzorov, T. P. Trouard, and M. F. Brown. Lipid bilayer dynamics from simultaneous analysis of orientation and frequency dependence of deuterium spin-lattice and quadrupolar order relaxation. *Phys. Rev. E*, 58:2259–2281, 1998.

[181] S. O. Nielsen, C. F. Lopez, G. Srinivas, and M. L. Klein. Coarse grain models and the computer simulation of soft materials. *J. Phys.: Condens. Matter*, 16:R481–R512, 2004.

[182] S. O. Nielsen, G. Srinivas, and M. L. Klein. Incorporating a hydrophobic solid into a coarse grain liquid framework: Graphite in an aqueous amphiphilic environment. *J. Chem. Phys.*, 123:124907, 2005.

[183] S. O. Nielsen, G. Srinivas, C. F. Lopez, and M. L. Klein. Modeling surfactant adsorption on hydrophobic surfaces. *Phys. Rev. Lett.*, 94:228301, 2005.

[184] P. S. Niemela, S. Ollila, M. T. Hyvönen, M. Karttunen, and I. Vattulainen. Assessing the nature of lipid raft membranes. *PLoS Comput. Biol.*, 3:304–312, 2007.

[185] V. Noinville, C. Vidal-Madjar, and B. Sebille. Modeling of protein adsorption on polymer surfaces. Computation of adsorption potential. *J. Phys. Chem.*, 99:1516–1522, 1995.

[186] H. Nygren, S. Alaeddin, I. Lundström, and K.-E. Magnusson. Effect of surface wettability on protein adsorption and lateral diffusion. Analysis of data and a statistical model. *Biophys. Chem.*, 49:263–272, 1994.

[187] M. R. Oberholzer and A. M. Lenhoff. Protein adsorption isotherms through colloidal energetics. *Langmuir*, 15:3905–3914, 1999.

[188] M. R. Oberholzer, N. J. Wagner, and A. M. Lenhoff. Grand canonical Brownian dynamics simulation of colloidal adsorption. *J. Chem. Phys.*, 107:´9157–9167, 1997.

[189] G. A. Olah, H. W. Huang, W. Liu, and Y. Wu. Location of ion-binding sites in the gramicidin channel by X-ray diffraction. *J. Molec. Biol.*, 218:847–858, 1991.

[190] O. H. S. Ollila, T. Rog, M. Karttunen, and I. Vattulainen. Role of sterol type on lateral pressure profiles of lipid membranes affecting membrane functionality: Comparison between cholesterol, desmosterol, 7-dehydrocholesterol and ketosterol. *J. Struct. Biol.*, 159:311–323, 2007.

[191] S. Ollila, M. T. Hyvönen, and I. Vattulainen. Polyunsaturation in lipid membranes: Dynamic properties and lateral pressure profiles. *J. Phys. Chem. B*, 111:3139–3150, 2007.

[192] L. Onsager. Electric moments of molecules in liquids. *J. Am. Chem. Soc.*, 58:1486–1493, 1936.

[193] C. Oostenbrink, A. Villa, A. E. Mark, and W. F. van Gunsteren. A biomolecular force field based on the free enthalpy of hydration and solvation: The GROMOS force-field parameter sets 53A5 and 53A6. *J. Comp. Chem.*, 25:1656–1676, 2004.

[194] E. Overton. *Studien über die Narkose*. Fischer, Jena, 1901.

[195] M. Patra. Lateral pressure profiles in cholesterol-DPPC bilayers. *Europ. Biophys. J.*, 35:79–88, 2005.

[196] M. Patra, E. Salonen, E. Terama, I. Vattulainen, R. Faller, B. W. Lee, J. Holopainen, and M. Karttunen. Under the influence of alcohol: The effect of ethanol and methanol on lipid bilayers. *Biophys. J.*, 90:1121–1135, 2006.

[197] L. Pauling. A molecular theory of general anesthesia. *Science*, 134:15–21, 1961.

[198] D. A. Pearlman, D. A. Case, J. W. Caldwell, W. S. Ross, T. E. Cheatham, S. DeBolt, D. Ferguson, G. Seibel, and P. Kollman. AMBER, a package of computer programs for applying molecular mechanics, normal mode analysis, molecular dynamics and free energy calculations to simulate the structural and energetic properties of molecules. *Comput. Phys. Comm.*, 91:1–41, 1995.

[199] K. Pearson. On lines and planes of closest fit to systems of points in space. *Philosophical Magazine*, 2:559–.572, 1901.

[200] X. Periole, T. Huber, S. J. Marrink, and T. P. Sakmar. G protein-coupled receptors self-assemble in dynamics simulations of model bilayers. *J. Am. Chem. Soc.*, 129:10126–10132, 2007.

[201] J. W. Perram, H. G. Petersen, and S. W. De Leeuw. An algorithm for the simulation of condensed matter which grows as the $3/2$ power of the number of particles. *Molec. Phys.*, 65:875–893, 1988.

[202] J. C. Phillips, R. Braun, W. Wang, J. Gumbart, E. Tajkhorshid, E. Villa, C. Chipot, R. D. Skeel, L. Kale, and K. Schulten. Scalable molecular dynamics with NAMD. *J. Comp. Chem.*, 26:1781–1802, 2005.

[203] L. Piela, J. Kostrowicki, and H. A. Scheraga. On the multiple-minima problem in the conformational analysis of molecules: Deformation of the potential energy hypersurface by the diffusion equation method. *J. Phys. Chem.*, 93:3339–3346, 1989.

[204] J. M. Pope and D. W. Dubro. The interaction of n-alkanes and n-alcohols with lipid bilayer membranes: A ^{2}H-NMR study. *Biochim. Biophys. Acta*, 858:243–253, 1986.

[205] J. M. Pope, L. W. Walker, and D. Dubro. On the ordering of n-alkane and n-alcohol solutes in phospholipid bilayer model membrane systems. *Chem. Phys. Lipids*, 35:259–277, 1984.

[206] M. J. Pringle, K. B. Brown, and K. W. Miller. Can the lipid theories of anesthesia account for the cutoff in anesthetic potency in homologous series of alcohols? *Molecular Pharmacology*, 19:49–55, 1981.

[207] C. Putzke, P. J. Hanley, G. Schlichthörl, R. Preisig-Müller, S. Rinne, M. Anetseder, R. Eckenhoff, C. Berkowitz, T. Vassiliou, H. Wulf, and L. Eberhart. Differential effects of volatile and intravenous anesthetics on the activity of human TASK-1. *American Journal of Physiology - Cell Physiology*, 293:C1319–C1326, 2007.

[208] J. J. Quinlan, S. Firestone, and L. L. Firestone. Isoflurane's enhancement of chloride flux through rat brain gamma-aminobutyric acid type A receptors is stereoselective. *Anesthesiology*, 83:611–615, 1995.

[209] J. J. Quinlan, D. Huntley, and L. L. Firestone. Isoflurane's enhancement of GABA-gated chloride flux is not stereoselective. *Anesthesiology*, 77:A701, 1992.

[210] A. Quinn, H. Mantz, K. Jacobs, M. Bellion, and L. Santen. Protein adsorption kinetics in different surface potentials. *Europhys. Lett.*, 81:56003, 2008.

[211] A. Rahman. Correlations in the motion of atoms in liquid argon. *Phys. Rev.*, 136:A405–A411, 1964.

[212] A. Rahman and F. H. Stillinger. Molecular dynamics study of liquid water. *J. Chem. Phys.*, 55:3336–3359, 1971.

[213] T. Raj and W. H. Flygare. Diffusion studies of bovine serum albumin by quasielastic light scattering. *Biochemistry*, 13:3336–3340, 1974.

[214] S. Ravichandran, J. D. Madura, and J. Talbot. A Brownian dynamics study of the initial stages of hen egg-white lysozyme adsorption at a solid interface. *J. Phys. Chem. B*, 105:3610–3613, 2001.

[215] S. Ravichandran and J. Talbot. Mobility of adsorbed proteins: A Brownian dynamics study. *Biophys. J.*, 78:110–120, 2000.

[216] W. Rawicz, K. C. Olbrich, T. McIntosh, D. Needham, and E. Evans. Effect of chain length and unsaturation on elasticity of lipid bilayers. *Biophys. J.*, 79:328–339, 2000.

[217] C. Reyes Mateo, P. Tauc, and J.-C. Brochon. Pressure effects on the physical properties of lipid bilayers detected by *trans*-parinaric acid fluorescence decay. *Biophys. J.*, 65:2248–2260, 1993.

[218] D. R. Rose, J. Phipps, J. Michniewicz, G. I. Birnbaum, F. R. Ahmed, A. Muir, W. F. Anderson, and S. Narang. Crystal structure of T4-lysozyme generated from synthetic coding DNA expressed in Escherichia coli. *Protein Eng.*, 2:277–282, 1988.

[219] C. M. Roth and A. M. Lenhoff. Electrostatic and van der Waals contributions to protein adsorption: Computation of equilibrium constants. *Langmuir*, 9:962–972, 1993.

[220] C. M. Roth, B. L. Neal, and A. M. Lenhoff. Van der Waals interactions involving proteins. *Biophys. J.*, 70:977–987, 1996.

[221] C. M. Roth, J. E. Sader, and A. M. Lenhoff. Electrostatic contribution to the energy and entropy of protein adsorption. *J. of Colloid and Interface Science*, 203:218–221, 1998.

[222] S. H. Roth. Physical mechanisms of anesthesia. *Ann. Rev. Pharmacol. Toxicol.*, 19:159–178, 1979.

[223] B. Roux and M. Karplus. Molecular dynamics simulations of the gramicidin channel. *Ann. Rev. Biophys. Biomol. Struct.*, 23:731–761, 1994.

[224] E. S. Rowe. Lipid chain length and temperature dependence of ethanol-phosphatidylcholine interactions. *Biochemistry*, 22:3299–3305, 1983.

[225] E. S. Rowe, F. Zhang, T. W. Leung, J. S. Parr, and P. T. Guy. Thermodynamics of membrane partitioning for a series of n-alcohols determined by titration calorimetry: Role of hydrophobic effects. *Biochemistry*, 37:2430–2440, 1998.

[226] J.-P. Ryckaert and A. Bellemans. Molecular dynamics of liquid n-butane near its boiling-point. *Chem. Phys. Lett.*, 30:123–125, 1975.

[227] J.-P. Ryckaert, G. Ciccotti, and H. J. C. Berendsen. Numerical integration of the cartesian equations of motion of a system with constraints: Molecular dynamics of n-alkanes. *J. Comp. Phys.*, 23:327–341, 1977.

[228] S. A. Safran. *Statistical Thermodynamics of Surfaces, Interfaces, and Membranes*. Frontiers in Physics. Westview, Boulder, Colorado, 2003.

[229] T. Schlick. *Molecular Modeling and Simulation*. Springer, New York, 2002.

[230] P. Schofield and J. R. Henderson. Statistical mechanics of inhomogeneous fluids. *Proc. R. Soc. Lond. A.*, 379:231–246, 1982.

[231] A. W. Schuettelkopf and D. M. F. van Aalten. PRODRG - a tool for high-throughput crystallography of protein-ligand complexes. *Act. Cryst. D*, 60:1355–1363, 2004.

[232] A. Seelig and J. Seelig. Membrane structure. In *Encyclopedia of Physical Science and Technology*, volume 9. Academic Press, 2002.

[233] J. Seelig, P. M. MacDonald, and P. G. Scherer. Phospholipid head groups as sensors of electric charge in membranes. *Biochemistry*, 26:7535–7541, 1987.

[234] P. Seeman, S. Roth, and H. Schneider. The membrane concentrations of alcohol anesthetics. *Biochim. Biophys. Acta*, 225:171–184, 1971.

[235] A. Y. Shih, A. Arkhipov, P. L. Freddolino, and K. Schulten. Coarse grained protein-lipid model with application to lipoprotein particles. *J. Phys. Chem. B*, 110:3674–3684, 2006.

[236] J. C. Shillcock and R. Lipowsky. Equilibrium structure and lateral stress distribution of amphiphilic bilayers from dissipative particle dynamics simulations. *J. Chem. Phys.*, 117:5048–5061, 2002.

[237] M. Sikor, A. Wixforth, and M. F. Schneider. Phase transitions of supported phosphatidylcholine membranes. *Submitted*.

[238] S. J. Singer and G. L. Nicolson. The fluid mosaic model of the structure of cell membranes. *Science*, 175:720–731, 1972.

[239] S. W. I. Siu and R. A. Böckmann. Electric field effects on membranes: Gramicidin A as a test ground. *J. Struct. Biol.*, 157:545–556, 2007.

[240] S. W. I. Siu and R. A. Böckmann. Low free energy barrier for ion permeation through double-helical gramicidin. *Submitted*, 2008.

[241] S. W. I. Siu, R. Vácha, P. Jungwirth, and R. A. Böckmann. Biomolecular simulations of membranes: Physical properties from different force fields. *J. Chem. Phys.*, 128:125103, 2008.

[242] J. L. Slater and C.-H. Huang. Interdigitated bilayer membranes. *Prog. Lipid Res*, 27:325–359, 1988.

[243] O. S. Smart, J. M. Goodfellow, and B. A. Wallace. The pore dimensions of gramicidin A. *Biophys. J.*, 65:2455–2460, 1993.

[244] J. Sonne, F. Y. Hansen, and G. H. Peters. Methodological problems in pressure profile calculations for lipid bilayers. *J. Chem. Phys.*, 122:124903, 2005.

[245] M. J. Stevens. Coarse-grained simulations of lipid bilayers. *J. Chem. Phys.*, 121:11942–11948, 2004.

[246] S. Sugio, A. Kashima, S. Mochizuki, M. Noda, and K. Kobayashi. Crystal structure of human serum albumin at 2.5 Angstrom resolution. *Protein Eng.*, 12:439–446, 1999.

[247] Y. Sugita and Y. Okamoto. Replica-exchange molecular dynamics method for protein folding. *Chem. Phys. Lett.*, 314:141–151, 1999.

[248] Y. Sugita and Y. Okamoto. Replica-exchange multicanonical algorithm and multicanonical replica-exchange method for simulating systems with rough energy landscape. *Chem. Phys. Lett.*, 329:261–270, 2000.

[249] I. Szleifer, A. Ben-Shaul, and W. M. Gelbart. Chain packing statistics and thermodynamics of amphiphile monolayers. *J. Phys. Chem.*, 94:5081–5089, 1990.

[250] I. Szleifer, D. Kramer, A. Ben-Shaul, W. M. Gelbart, and S. A. Safran. Molecular theory of curvature elasticity in surfactant films. *J. Chem. Phys.*, 92:6800–6817, 1990.

[251] J. Talbot, G. Tarjus, P. R. van Tassel, and P. Viot. From car parking to protein adsorption: An overview of sequential adsorption processes. *Colloids and Surfaces*, 165:287–324, 2000.

[252] K. Tamura, Y. Kaminoh, H. Kamaya, and I. Ueda. High pressure antagonism of alcohol effects on the main phase-transition temperature of phospholipid membranes: Biphasic response. *Biochim. Biophys. Acta*, 1066:219–224, 1991.

[253] P. Tang, R. G. Eckenhoff, and Y. Xu. General anesthetic binding to gramicidin A: The structural requirements. *Biophys. J.*, 78:1804–1809, 2000.

[254] P. Tang, J. Hu, S. Liachenko, and Y. Xu. Distinctly different interactions of anesthetic and nonimmobilizer with transmembrane channel peptides. *Biophys. J.*, 77:739–746, 1999.

[255] P. Tang, P. K. Mandal, and M. Zegarra. Effects of volatile anesthetic on channel structure of gramicidin A. *Biophys. J.*, 83:1413–1420, 2002.

[256] P. Tang, V. Simplaceanu, and Y. Xu. Structural consequences of anesthetic and nonimmobilizer interaction with gramicidin A channels. *Biophys. J.*, 76:2346–2350, 1999.

[257] P. Tang and Y. Xu. Large-scale molecular dynamics simulations of general anesthetic effects on the ion channel in the fully hydrated membrane: The implication of molecular mechanisms of general anesthesia. *Proc. Natl. Acad. Sci. USA*, 99:16035–16040, 2002.

[258] R. H. Templer, S. J. Castle, A. R. Curran, G. Rumbles, and D. R. Klug. Sensing isothermal changes in the lateral pressure in model membranes using di-pyrenyl phosphatidylcholine. *Faraday Discuss.*, 111:41–53, 1999.

[259] E. Terama, O. H. S. Ollila, E. Salonen, A. C. Rowat, C. Trandum, P. Westh, M. Patra, M. Karttunen, and I. Vattulainen. Influence of ethanol on lipid membranes: From lateral pressure profiles to dynamics and partitioning. *J. Phys. Chem. B*, 112:4131–4139, 2008.

[260] J. L. Thewalt, A. P. Tulloch, and R. J. Cushley. A deuterium NMR study of labelled n-alkanol anesthetics in a model membrane. *Chem. Phys. Lipids*, 39:93–107, 1986.

[261] D. P. Tieleman, 2008. Private Communication, The joint 16th International Biophysics Congress (IUPAB) and Biophysical Society 52nd Annual Meeting, February 2-6 2008, Long Beach, California, USA.

[262] D. P. Tieleman, J. L. MacCallum, W. L. Ash, C. Kandt, Z. Xu, and L. Monticelli. Membrane protein simulations with a united-atom lipid and all-atom protein model: Lipid-protein interactions, side chain transfer free energies and model proteins. *J. Phys.: Condens. Matter*, 18:S1221–S1234, 2006.

[263] D. P. Tieleman, S. J. Marrink, and H. J. C. Berendsen. A computer perspective of membranes: Molecular dynamics studies of lipid bilayer systems. *Biochim. Biophys. Acta*, 1331:235–270, 1997.

[264] K. J. Tierney, D. E. Block, and M. L. Longo. Elasticity and phase behavior of DPPC membrane modulated by cholesterol, ergosterol, and ethanol. *Biophys. J.*, 89:2481–2493, 2005.

[265] R. D. Tilton, C. R. Robertson, and A. P. Gast. Lateral diffusion of bovine serum albumin adsorbed at the solid-liquid interface. *J. of Colloid and Interface Science*, 137:192–203, 1990.

[266] I. G. Tironi, R. Sperb, P. E. Smith, and W. F. van Gunsteren. A generalized reaction field method for molecular dynamics simulations. *J. Chem. Phys.*, 102:5451–5459, 1995.

[267] V. Tozzini. Coarse-grained models for proteins. *Curr. Opin. Struct. Biol.*, 15:144–150, 2005.

[268] C. Trandum, P. Westh, K. Jorgensen, and O. G. Mouritsen. Association of ethanol with lipid membranes containing cholesterol, sphingomyelin and ganglioside: A titration calorimetry study. *Biochim. Biophys. Acta*, 1420:179–188, 1999.

[269] C. Trandum, P. Westh, K. Jorgensen, and O. G. Mouritsen. A thermodynamic study of the effects of cholesterol on the interaction between liposomes and ethanol. *Biophys. J.*, 78:2486–2492, 2000.

[270] W. Treptow, S. J. Marrink, and M. Tarek. Gating motions in voltage-gated potassium channels revealed by coarse-grained molecular dynamics simulations. *J. Phys. Chem. B*, 112:3277–3282, 2008.

[271] J. R. Trudell. A unitary theory of anesthesia based on lateral phase separations in nerve membranes. *Anesthesiology*, 46:5–10, 1977.

[272] J. R. Trudell, W. L. Hubbell, E. N. Cohen, and J. J. Kendig. Pressure reversal of anesthesia: The extent of small-molecule exclusion from spin-labeled phospholipid model membranes. *Anesthesiology*, 38:207–211, 1973.

[273] K. Tu, M. Tarek, M. L. Klein, and D. Scharf. Effects of anesthetics on the structure of a phospholipid bilayer: Molecular dynamics investigation of halothane in the hydrated liquid crystal phase of dipalmitoylphosphatidylcholine. *Biophys. J.*, 75:2123–2134, 1998.

[274] B. W. Urban. Die Meyer-Overton Regel: Was ist geblieben? In T. Pasch, E. R. Schmid, and A. Zollinger, editors, *Anästhesie in Zürich: 100 Jahre Entwicklung 1901-2001*, pages 15–23, 2001.

[275] B. W. Urban, M. Bleckwenn, and M. Barann. Interactions of anesthetics with their targets: Non-specific, specific or both? *Pharmacology & Therapeutics*, 111:729–770, 2006.

[276] E. van den Brink-van der Laan, V. Chupin, J. A. Killian, and B. de Kruijff. Small alcohols destabilize the KcsA tetramer via their effect on the membrane lateral pressure. *Biochemistry*, 43:5937–5942, 2004.

[277] P. van der Ploeg and H. J. C. Berendsen. Molecular dynamics simulation of a bilayer membrane. *J. Chem. Phys.*, 76:3271–3276, 1982.

[278] D. van der Spoel, E. Lindahl, B. Hess, G. Groenhof, A. E. Mark, and H. J. C. Berendsen. GROMACS: Fast, flexible, and free. *J. Comp. Chem.*, 26:1701–1718, 2005.

[279] D. van der Spoel, P. J. van Maaren, P. Larsson, and N. Timneanu. Thermodynamics of hydrogen bonding in hydrophilic and hydrophobic media. *J. Phys. Chem. B*, 110:4393–4398, 2006.

[280] W. F. van Gunsteren, D. Bakowies, R. Baron, I. Chandrasekhar, M. Christen, X. Daura, P. Gee, D. P. Geerke, A. Glättli, P. H. Hünenberger, M. A. Kastenholz, C. Oostenbrink, M. Schenk, D. Trzesniak, N. F. A. van der Vegt, and H. B. Yu. Biomolecular modeling: Goals, problems, perspectives. *Angew. Chem. Int. Ed. Engl.*, 45:4064–4092, 2006.

[281] W. F. van Gunsteren and H. J. C. Berendsen. *Groningen Molecular Simulation (GROMOS) Library Manual*. BIOMOS biomolecular software, Laboratory of Physical Chemistry, University of Groningen, The Netherlands, 1987.

[282] W. F. van Gunsteren and H. J. C. Berendsen. Computer simulation of molecular dynamics: Methodology, applications, and perspectives in chemistry. *Angew. Chem. Int. Ed. Engl.*, 29:992–1023, 1990.

[283] W. F. van Gunsteren, H. J. C. Berendsen, J. Hermans, W. G. J. Hol, and J. P. M. Postma. Computer simulation of the dynamics of hydrated protein crystals and its comparison with X-ray data. *Proc. Natl. Acad. Sci. USA*, 80:4315–4319, 1983.

[284] W. F. van Gunsteren, S. R. Billeter, A. A. Eising, P. H. Hünenberger, P. Krüger, A. E. Mark, W. R. P. Scott, and I. G. Tironi. *Biomolecular Simulation: The GROMOS96 Manual and User Guide*. Vdf Hochschulverlag AG an der ETH Zürich, Zürich, Switzerland, 1996.

[285] W. F. van Gunsteren and M. Karplus. Effect of constraints, solvent and crystal environment on protein dynamics. *Nature*, 293:677–678, 1981.

[286] W. F. van Gunsteren and M. Karplus. Protein dynamics in solution and in a crystalline environment: A molecular dynamics study. *Biochemistry*, 21:2259–2274, 1982.

[287] S. Vemparala, C. Domene, and M. L. Klein. Interaction of anesthetics with open and closed conformations of a potassium channel studied via molecular dynamics and normal mode analysis. *Biophys. J.*, 94:4260–4269, 2008.

[288] S. Vemparala, L. Saiz, R. G. Eckenhoff, and M. L. Klein. Partitioning of anesthetics into a lipid bilayer and their interaction with membrane-bound peptide bundles. *Biophys. J.*, 91:2815–2825, 2006.

[289] M. Venturoli and B. Smit. Simulating the self-assembly of model membranes. *Phys. Chem. Comm.*, 10:45–49, 1999.

[290] M. Venturoli, M. M. Sperotto, M. Kranenburg, and B. Smit. Mesoscopic models of biological membranes. *Phys. Rep.*, 437:1–54, 2006.

[291] L. Verlet. Computer "experiments" on classical fluids. I. Thermodynamical properties of Lennard-Jones molecules. *Phys. Rev.*, 159:98–103, 1967.

[292] G. Vriend. WHAT IF: A molecular modeling and drug design program. *J. Mol. Graphics*, 8:52–56, 1990.

[293] J. Wang, R. M. Wolf, J. W. Caldwell, P. A. Kollman, and D. A. Case. Development and testing of a general amber force field. *J. Comp. Chem.*, 25:1157–1174, 2004.

[294] P. K. Weiner and P. A. Kollman. AMBER: Assisted model building with energy refinement. A general program for modeling molecules and their interactions. *J. Comp. Chem.*, 2:287–303, 1981.

[295] S. J. Weiner, P. A. Kollman, D. A. Case, U. C. Singh, C. Ghio, G. Alagona, S. Profeta, and P. Weiner. A new force field for molecular mechanical simulation of nucleic acids and proteins. *J. Am. Chem. Soc.*, 106:765–784, 1984.

[296] P. W. Westerman, J. M. Pope, N. Phonphok, J. W. Doane, and D. W. Dubro. The interaction of n-alkanols with lipid bilayer membranes: a ^{2}H-NMR study. *Biochim. Biophys. Acta*, 939:64–78, 1988.

[297] A. C. Williams and B. W. Barry. Penetration enhancers. *Advanced Drug Delivery Reviews*, 56:603–618, 2004.

[298] J. Wohlert and O. Edholm. Dynamics in atomistic simulations of phospholipid membranes: Nuclear magnetic resonance relaxation rates and lateral diffusion. *J. Chem. Phys.*, 125:204703, 2006.

[299] P. T. T. Wong, W. F. Murphy, and H. H. Mantsch. Pressure effects on the Raman spectra of phospholipid membranes: Pressure induced phase transitions and structural changes in 1,2-dimyristoyl 3-sn-phopshatidylcholine water dispersions. *J. Chem. Phys.*, 76:5230–5237, 1982.

[300] L. V. Woodcock. Isothermal molecular dynamics calculations for liquid salts. *Chem. Phys. Lett.*, 10:257–261, 1971.

[301] G. A. Woolley and B. A. Wallace. Model ion channels: Gramicidin and alamethicin. *J. Membr. Biol.*, 129:109–136, 1992.

[302] T. X. Xiang and B. D. Anderson. Molecular distributions in interphases: Statistical mechanical theory combined with molecular dynamics simulation of a model lipid bilayer. *Biophys. J.*, 66:561–572, 1994.

[303] Y. Xu, P. Tang, and S. Liachenko. Unifying characteristics of sites of anesthetic action revealed by combined use of anesthetics and non-anesthetics. *Toxicology Letters*, 100-101:347–352, 1998.

[304] S. Yefimov, E. van der Giessen, P. R. Onck, and S. J. Marrink. Mechanosensitive membrane channels in action. *Biophys. J.*, 94:2994–3002, 2008.

[305] M. J. Yonkunas, Y. Xu, and P. Tang. Anesthetic interaction with ketosteroid isomerase: Insights from molecular dynamics simulations. *Biophys. J.*, 89:2350–2356, 2005.

[306] J. Zhou, S. Chen, and S. Jiang. Orientation of adsorbed antibodies on charged surfaces by computer simulation based on a united-residue model. *Langmuir*, 19:3472–3478, 2003.

Acknowledgment

First of all I would like to thank Dr. Rainer Böckmann for giving me the opportunity to perform my studies in the *Theoretical and Computational Membrane Biology Group* at the Saarland University, for his excellent support and supervision of my work, and for the proofreading of this thesis. He gave me the chance to participate in many scientific conferences and he initiated the successful cooperation with the group of Dr. Matthias Schneider in Augsburg, which I both enjoyed very much. I thank him also for creating an easy working environment including the regular group meetings not only at the office, but also in the evenings, at weekends, or at a skiing excursion to Switzerland.

I thank Prof. Dr. Karin Jacobs for becoming the adviser of this thesis, for reviewing this work, and for helping me with questions regarding this thesis.

Furthermore, I would like to thank all current and former members of the TCoMB group for their help and for the pleasant working atmosphere. I thank Shirley W. I. Siu for being a good roommate at the office and also during the various conferences. I especially liked London and Long Beach, where we not only enjoyed the scientific conference, but also did some sightseeing and traveling together. We had many interesting professional discussions and I could always rely on her programming skills. Working with Simon Leis on our joint article was fun and he always helped me with any kind of practical or technical questions. I thank Caroline Becker for listening to and discussing with me the various problems occurring while finalizing this thesis, and Alexander Benedix and Caroline Becker for their help with all kind of questions and problems regarding our computers and cluster. Daniele Narzi is the one to ask concerning chemistry and everybody appreciates his cooking skills and his continuous good mood. Thanks to Christian Hanke for the good cooperation for the coarse-grained project.

With Prof. Dr. Volkhard Helm's group we shared not only the group seminar, but also many nice conference stays, birthdays, and paper acceptance celebrations. Thanks for that, too!

Finally, I would like to thank Martin Hövel for all his help and support throughout the work on this thesis and I would like to especially point out his help with the design of my posters and some of the pictures in this thesis.

Publications

B. Griepernau, S. Leis, M. F. Schneider, M. Sikor, D. Steppich, and R. A. Böckmann:
1-Alkanols and Membranes: A Story of Attraction
BBA Biomembranes 1768, 2899-2913, 2007

B. Griepernau and R. A. Böckmann:
The Influence of 1-Alkanols and External Pressure on the Lateral Pressure Profiles of Lipid Bilayers
Biophysical Journal 95, 5766-5778, 2008

B. Griepernau and R. A. Böckmann:
Influence of Anesthetics on a Membrane Ion Channel Studied by Molecular Dynamics Simulations
submitted to Soft Matter, 2009

B. Griepernau, C. Hanke, L. Santen, and R. A. Böckmann:
Coarse-Grained Simulations of Protein Adsorption on Solid Surfaces
in: From Computational Biophysics to Systems Biology (CBSB08), ed. Ulrich H. E. Hansmann, Jan H. Meinke, Sandipan Mohanty, Walter Nadler, and Olav Zimmermann, NIC Series 40, 223-226, 2008

Conference Talks and Contributions

2006

2nd Augsburg Winterschool on Complex Materials at Interfaces, Bad Wiessee, talk

International Workshop *Dynamics of Artificial and Biological Membranes*, Gomadingen, talk

WE Heraeus Seminar *Biomolecular Simulation: From Physical Principles to Biological Function*, Bad Honnef, poster presentation

Workshop *Computer Simulation and Theory of Macromolecules*, Hünfeld, poster presentation

Annual Meeting of the German Biophysical Society, Mainz, poster presentation

Workshop of the Graduate College *Structure Formation and Transport in Complex Systems*, Bosen

2007

International Bunsen Discussion Meeting *Membrane Interacting Peptides and Proteins*, Halle, talk

Workshop *Computer Simulation and Theory of Macromolecules*, Hünfeld, talk

6th EBSA European Biophysics Congress, London, poster presentation

Workshop of the Graduate College *Structure Formation and Transport in Complex Systems*, Saarbrücken, poster presentation

2008

Biophysical Society 52nd Annual Meeting & 16th IUPAB International Biophysics Congress, Long Beach, USA, poster presentation

International Workshop *Mechanical and Electrical Properties of Artificial and Cellular Membranes*, Gomadingen, poster presentation

Workshop *Computer Simulation and Theory of Macromolecules*, Hünfeld, poster presentation

Workshop *From Computational Biophysics to Systems Biology*, Jülich, poster presentation

Awards

Travel Grant of the *German Biophysical Society*, July 2007

Poster Prize at the *6th EBSA European Biophysics Congress*, London, July 2007

Best Poster Award at the Workshop of the Graduate College *Structure Formation and Transport in Complex Systems*, Saarbrücken, September 2007